Spin-flip time-dependent density functional theory and its applications to photodynamics

DISSERTATION

Presented in Partial Fulfillment of the Requirements for

the Degree Doctor of Philosophy in the Graduate

School of The Ohio State University

By

Xing Zhang, B.S.

Graduate Program In Chemistry

The Ohio State University

2016

Dissertation Committee:

John M. Herbert, Advisor

Sherwin J. Singer

Marcos M. Sotomayor

Abstract

In order to correctly simulate photodynamics, it is required to use first-principle methods since multiple electronic states have to be considered at the same time. As such, instead of computationally inexpensive classical molecular dynamics simulations, usually expensive *ab initio* molecular dynamics (AIMD) simulations become the only choice. For an excited-state AIMD simulation with the system including more than twenty heavy atoms, the only affordable quantum chemical method that is able to generate reasonable results may be the linear-response time-dependent density functional theory (LR-TDDFT). Other methods are either computationally too expensive (*e.g.* multireference methods) or unable to correctly describe the potential surfaces for both ground and excited electronic states (*e.g.* configuration interaction singles). However, conventional LR-TDDFT is not capable of describing the correct topology of conical intersections, where nonadiabatic transitions between electronic states take place. The simplest remedy is to use the "spin-flip" (SF) generalization of TDDFT, originally developed to investigate diradicals with strong static correlation in their ground states. This method treats the ground and excited states on an equal footing which thereby guarantees the correct topology at conical intersections. Recent computational studies have shown good performance of SF-TDDFT in describing electronic excitation energies, conical intersections, and excited-state

reaction pathways. It may also be attractive to directly simulate photochemical or photophysical events through nonadiabatic AIMD simulations. Usually, these simulations require the calculation of nonadiabatic derivative couplings (NDCs), which are available only for a few electronic structure theory methods. Here, we present the formal derivations and implementations of the NDCs for both LR-TDDFT and SF-TDDFT. We also applied SF-TDDFT to study the ultrafast nonradiative decay of uracil solvated in aqueous solution, and proposed the deactivation mechanism to explain the experimentally observed different excited-state lifetimes of gas-phase and solvated uracil. Finally, the spin-adapted version of SF-TDDFT has been developed, which cures the spin contamination problem of the conventional SF-TDDFT. Preliminary calculations show that this new method is potentially promising for nonadiabatic AIMD simulations.

Acknowledgments

I would like to thank my advisor, Dr. John M. Herbert, whose valuable guidance and consistent encouragement made my dissertation work possible. I also appreciate the freedom that John provided me to pursue various projects, which made my Ph.D. studies more enjoyable. I express my sincere gratitude to all the members in the Herbert group, especially Drs. Ka Un Lao, Jie Liu, Ryan Richard and Zhi-qiang You, for insightful discussions and inspiring ideas. Finally, I owe uncountable thanks to my parents, Yao Shen and Bin Zhang, and my girlfriend, Danlu Wang, without whose undying support I would have not succeeded.

Vita

1989	Born, Hangzhou, Zhejiang, China
2007	Hangzhou NO. 2 High School of Zhejiang Province
2011	B.S. Chemistry, Nanjing University, China
2011–2012	Graduate Teaching Associate, The Ohio State University
2012–2016	Graduate Research Associate, The Ohio State University

Publications

(6) J. M. Herbert, X. Zhang, A. F. Morrison, and J. Liu. **Beyond time-depenent density functional theory using only single excitations: Methods for computational studies of excited states in complex systems.** *Acc. Chem. Res.,* **49**, 931, (2016).

(5) X. Zhang and J. M. Herbert. **Spin-flip, tensor equation-of-motion configuration interaction with a density-functional correction: A spin-complete method for exploring excited-state potential energy surfaces.** *J. Chem. Phys.,* **143**, 234107 (2015).

(4) X. Zhang and J. M. Herbert. **Analytic derivative couplings in time-dependent density functional theory: Quadratic response theory versus pseudo-wavefunction approach.** *J. Chem. Phys.,* **142**, 064109 (2015).

(3) Y. Shao *et al.*. **Advances in molecular quantum chemistry contained in the Q-Chem 4 program package.** *Mol. Phys.,* **113**, 184 (2015).

(2) X. Zhang and J. M. Herbert. **Analytic derivative couplings for spin-flip configuration interaction singles and spin-flip time-dependent density functional theory.** *J. Chem. Phys.,* **141**, 064104 (2014).

(1) X. Zhang and J. M. Herbert. **Excited-state deactivation pathways in uracil versus hydrated uracil: Solvatochromatic shift in the $^1n\pi^*$ state is the key.** *J. Phys. Chem. B,* **118**, 7806 (2014).

Fields of Study

Major Field: Chemistry
Theoretical Physical Chemistry

Table of Contents

List of Figures

List of Tables

CHAPTER 1

Introduction

In this chapter, we introduce the Born-Oppenheimer adiabatic approximation and its breakdown at conical intersections. We also discuss the benefit of applying spin-flip time-dependent density functional theory (SF-TDDFT) to photodynamics, which is the main topic of the following chapters.

1.1 The Born-Oppenheimer Adiabatic Approximation

The most common procedure for solving a quantum chemical problem is usually solving the molecular non-relativistic Schrödinger equation in its time-independent form:

$$\hat{H}\Psi(\mathbf{r},\mathbf{R}) = E\Psi(\mathbf{r},\mathbf{R}), \tag{1.1}$$

where $\mathbf{r}$ and $\mathbf{R}$ denote the coordinates of the electrons and the nuclei, respectively, and $\hat{H}$, Ψ and E are the Hamiltonian, wavefunction and total energy of the system, respectively. Specifically, the Hamiltonian consists of an electronic part and a nuclear part,

$$\hat{H} = \hat{H}_e + \hat{T}_n \tag{1.2}$$

with

$$\hat{H}_e = -\sum_i \frac{1}{2}\hat{\boldsymbol{\nabla}}_i^2 - \sum_{i,A} \frac{Z_A}{r_{iA}} + \frac{1}{2}\sum_{i,j} \frac{1}{r_{ij}} + \frac{1}{2}\sum_{A,B} \frac{Z_A Z_B}{R_{AB}}, \tag{1.3}$$

and

$$\hat{T}_n = -\frac{1}{2M}\hat{\boldsymbol{\nabla}}_{\mathbf{R}}^2. \tag{1.4}$$

The above two equations are expressed in atomic units, and $r_{iA} = |\mathbf{r}_i - \mathbf{R}_A|$ denotes the distance between an electron i and a nucleus A. Similar definitions hold for r_{ij} and R_{AB}. Z_A represents the charge of a nucleus A, and M is an averaged nuclear mass, which depends on the coordinate system chosen.

Suppose we are able to obtain the eigenfunctions of the electronic Hamiltonian $\hat{H}_e$ at a fixed molecular configuration $\mathbf{R}$,

$$\hat{H}_e \Phi_i(\mathbf{r}, \mathbf{R}) = V_i(\mathbf{R})\Phi_i(\mathbf{r}, \mathbf{R}). \tag{1.5}$$

The set of electronic eigenfunctions $\{\Phi_i(\mathbf{r}, \mathbf{R})\}$ form a complete basis in the electronic space at every value of $\mathbf{R}$. Thus, we can expand the total wavefunction Ψ in this basis:

$$\Psi(\mathbf{r}, \mathbf{R}) = \sum_i \Phi_i(\mathbf{r}, \mathbf{R})\chi_i(\mathbf{R}). \tag{1.6}$$

Inserting Eq. (1.6) into Eq. (1.1), multiplying from the left by $\Phi_j(\mathbf{r}, \mathbf{R})$ and integrating over the electronic coordinates lead to

$$[\hat{T}_n + V_j(\mathbf{R})]\chi_j(\mathbf{R}) - \sum_i \Lambda_{ji}\chi_i(\mathbf{R}) = E\chi_j(\mathbf{R}), \tag{1.7}$$

where Λ_{ji} describes the couplings between electronic and nuclear motion,

$$\Lambda_{ji} = \frac{1}{2M}(2\mathbf{d}_{ji} \cdot \hat{\boldsymbol{\nabla}}_{\mathbf{R}} + G_{ji}). \tag{1.8}$$

In Eq. (1.8), we define the nonadiabatic derivative couplings

$$\mathbf{d}_{ji}(\mathbf{R}) = \langle \Phi_j(\mathbf{r},\mathbf{R}) | \hat{\boldsymbol{\nabla}}_{\mathbf{R}} \Phi_i(\mathbf{r},\mathbf{R}) \rangle_{\mathbf{r}}, \tag{1.9}$$

and the nonadiabatic scalar couplings

$$G_{ji}(\mathbf{R}) = \langle \Phi_j(\mathbf{r},\mathbf{R}) | \hat{\boldsymbol{\nabla}}^2_{\mathbf{R}} \Phi_i(\mathbf{r},\mathbf{R}) \rangle_{\mathbf{r}}. \tag{1.10}$$

Now, the nuclear equation of motion in Eq. (1.7) can be rewritten in a matrix form,

$$(\mathbf{T_n} + \mathbf{V} - \boldsymbol{\Lambda})\boldsymbol{\chi} = E\boldsymbol{\chi}, \tag{1.11}$$

where $\mathbf{T_n}$ is the nuclear kinetic energy operator (Eq. (1.4)) multiplied by a unit matrix, $\mathbf{V}$ is a diagonal matrix with diagonal elements that are the electronic energies in Eq. (1.5), the coupling matrix $\boldsymbol{\Lambda}$ has elements defined in Eq. (1.8), and $\boldsymbol{\chi}$ is a column vector defined as $\boldsymbol{\chi} \equiv [\chi_1\ \chi_2\ ...\ \chi_n]^{\mathrm{T}}$ with n denoting the number of electronic states. It is possible to further simplify Eq. (1.11) to the following appealing form,

$$\Big[-\frac{1}{2M}(\underset{\sim}{\boldsymbol{\nabla}} + \underset{\sim}{\mathbf{d}})^2 + \mathbf{V} - E \Big]\boldsymbol{\chi} = \mathbf{0}, \tag{1.12}$$

where $\underset{\sim}{\boldsymbol{\nabla}}$ is the nuclear gradient operator $\hat{\boldsymbol{\nabla}}_{\mathbf{R}}$ multiplied by a unit matrix, and $\underset{\sim}{\mathbf{d}}$ is the derivative coupling matrix with its element defined in Eq. (2.1). Both $\underset{\sim}{\boldsymbol{\nabla}}$ and $\underset{\sim}{\mathbf{d}}$ are vector matrices. To derive Eq. (1.12), we have applied a useful relation that

$$\mathbf{G} = (\underset{\sim}{\boldsymbol{\nabla}} \cdot \underset{\sim}{\mathbf{d}}) + \underset{\sim}{\mathbf{d}} \cdot \underset{\sim}{\mathbf{d}}. \tag{1.13}$$

Eq. (1.12) demonstrates that the coupled motion of the electrons and nuclei can be viewed as the nuclear motion in an electronic matrix potential $\mathbf{V}$, however, with a

dressed kinetic energy $-\frac{1}{2M}(\underset{\sim}{\boldsymbol{\nabla}} + \underset{\sim}{\mathbf{d}})^2$, which is different from the kinetic energy for bare nuclei [Eq. (1.4)].

If the couplings between the electronic and nuclear degrees of freedom can be completely ignored, $\underset{\sim}{\mathbf{d}}$ vanishes, and Eq. (1.12) reduces to

$$\Big[-\frac{1}{2M}\underset{\sim}{\boldsymbol{\nabla}}^2 + \mathbf{V} - E \Big]\boldsymbol{\chi} = \mathbf{0}. \tag{1.14}$$

Eq. (1.14) is the so-called *Born-Oppenheimer adiabatic approximation* or briefly *adiabatic approximation*. Note its difference from the *Born-Oppenheimer approximation*, which only ignores the off-diagonal elements of $\boldsymbol{\Lambda}$.[5] The adiabatic approximation implies that the nuclei move on a single target electronic potential surface and that the total energy of the system is simply the sum of the nuclear kinetic energy and the the potential energy of the target electronic state [*i.e.*, $V_i(\mathbf{R})$ in Eq. (1.5)].

1.2 Breakdown of the Adiabatic Approximation

In this section, we discuss the situations in which the adiabatic approximation breaks down. Obviously, from Eq. (1.12), we know that the adiabatic approximation becomes questionable when the magnitude of the derivative couplings is significant. By operating $\hat{\boldsymbol{\nabla}}_{\mathbf{R}}$ on both sides of Eq. (1.5) and multiplying Φ_j from the left, we are able to express the derivative couplings in their Hellmann-Feynman form,

$$\mathbf{d}_{ji} = \frac{\langle \Phi_j(\mathbf{r},\mathbf{R}) | (\hat{\boldsymbol{\nabla}}_{\mathbf{R}} \hat{H}_e) | \Phi_i(\mathbf{r},\mathbf{R}) \rangle_{\mathbf{r}}}{V_i(\mathbf{R}) - V_j(\mathbf{R})}. \tag{1.15}$$

From Eq. (1.15), we see that the derivative coupling becomes substantial when the energy gap between the two electronic states gets small. In the extreme case where

the two states are degenerate, the derivative coupling diverges and the adiabatic approximation becomes meaningless.

1.3 Conical intersections

In the region where derivative couplings are sizable, *e.g.*, in the vicinity of state crossings, the electronic and nuclear motions are greatly coupled. And the picture that nuclei move on a single potential energy surface is no longer valid. Instead, multiple electronic states may contribute to the total wavefunction of the system [Eq. (1.6)]. In a semi-classical description, the nuclear wavepacket has certain probability to "hop" between different electronic states.[6] The hopping probability is usually proportional to the magnitude of the derivative couplings.[7] In short, nuclear motion can induce electronic transitions near state crossings. These transitions do not emit photons, and are commonly called nonadiabatic transitions.

Nonadiabatic events are the major studies in theoretical photochemistry, for example, internal conversion and intersystem crossing. However, in most cases it's not possible to directly solve the quantum nuclear equation of motion shown in Eq. (1.12), because of the high computational cost. The more feasible way to simulate the nuclear motion is usually the (semi-classical) nonadibatic *ab initio* molecular dynamics (NAIMD) mentioned above.[6] In addition, it can be instructive to locate the electronic state crossings, since these are the points where nonadiabatic transitions take place, and the quality of the potential surfaces in the vicinity of these crossings also determines the performance of NAIMD simulations. In the following, we briefly introduce

the topography of a specific kind of state crossings, the conical intersection.

If we expand the electronic wavefunctions in a basis set $\{\boldsymbol{\phi}(\mathbf{r},\mathbf{R})\}$

$$\Phi_i(\mathbf{r},\mathbf{R}) = \sum_a c_a^i(\mathbf{R})\phi_a(\mathbf{r},\mathbf{R}), \tag{1.16}$$

Eq. (1.5) can be cast into a matrix form,

$$\mathbf{H}^{\mathrm{el}}(\mathbf{R})\mathbf{c}^i(\mathbf{R}) = V_i(\mathbf{R})\mathbf{c}^i(\mathbf{R}), \tag{1.17}$$

where $\mathbf{H}^{\mathrm{el}}(\mathbf{R})$ is the electronic Hamiltonian represented in the basis $\{\boldsymbol{\phi}(\mathbf{r},\mathbf{R})\}$ with its matrix elements shown below,

$$\mathrm{H}_{ab}^{\mathrm{el}}(\mathbf{R}) = \langle\phi_a(\mathbf{r},\mathbf{R})|\hat{H}_e|\phi_b(\mathbf{r},\mathbf{R})\rangle_{\mathbf{r}} \tag{1.18}$$

Suppose that M states cross with each other at the nuclear configuration $\mathbf{R}_{\mathrm{X}}$. It is then possible to construct a new basis from a geometric-independent transformation of $\{\boldsymbol{\phi}(\mathbf{r},\mathbf{R})\}$. The first M components of this basis, denoted as Q space, can be expressed as $\mathbf{c}^i(\mathbf{R}_{\mathrm{X}})^{\mathrm{T}}\boldsymbol{\phi}(\mathbf{r},\mathbf{R})$ with $i = 1,\ 2,\ ...,\ M$, which are the solutions of Eq. (1.17) at $\mathbf{R}_{\mathrm{X}}$. The remaining $N - M$ basis functions, denoted as P space, are chosen to be orthogonal to the first M basis functions, and are denoted as $\mathbf{C}^j(\mathbf{R}_{\mathrm{X}})^{\mathrm{T}}\boldsymbol{\phi}(\mathbf{r},\mathbf{R})$, which are generally not the solutions of Eq. (1.17). The electronic Hamiltonian in the new basis can be represented as

$$\begin{pmatrix} \mathbf{H}^{QQ} & \mathbf{H}^{QP} \\ \mathbf{H}^{PQ} & \mathbf{H}^{PP} \end{pmatrix}, \tag{1.19}$$

where

$$H_{ij}^{QQ} = \mathbf{c}^i(\mathbf{R}_{\mathrm{X}})^{\mathrm{T}}\mathbf{H}^{\mathrm{el}}(\mathbf{R})\mathbf{c}^j(\mathbf{R}_{\mathrm{X}}), \tag{1.20}$$

$$(H_{ai}^{PQ})^{\mathrm{T}} = H_{ia}^{QP} = \mathbf{c}^i(\mathbf{R}_{\mathrm{X}})^{\mathrm{T}}\mathbf{H}^{\mathrm{el}}(\mathbf{R})\mathbf{C}^a(\mathbf{R}_{\mathrm{X}}), \tag{1.21}$$

and

$$H_{ab}^{PP} = \mathbf{C}^a(\mathbf{R}_\mathrm{X})^\mathrm{T}\mathbf{H}^\mathrm{el}(\mathbf{R})\mathbf{C}^b(\mathbf{R}_\mathrm{X}). \tag{1.22}$$

At $\mathbf{R}_\mathrm{X}$, $\mathbf{H}^{QQ}$ becomes diagonal with all M diagonal elements equal to the degenerate state energy, and $\mathbf{H}^{PQ}$ and $\mathbf{H}^{QP}$ vanish.

If there is another crossing point $\mathbf{R}_\mathrm{Y} = \mathbf{R}_\mathrm{X} + \boldsymbol{\delta}\mathbf{R}$ that is close to $\mathbf{R}_\mathrm{X}$, the Hamiltonian in the Q space $\mathbf{H}^{QQ}$ at $\mathbf{R}_\mathrm{Y}$ may be written at first order as[8]

$$H_{ii}^{QQ}(\mathbf{R}_\mathrm{Y}) = V_i(\mathbf{R}_\mathrm{X}) + \mathbf{g}_i(\mathbf{R}_\mathrm{X}) \cdot \boldsymbol{\delta}\mathbf{R}, \tag{1.23}$$

$$H_{ij}^{QQ}(\mathbf{R}_\mathrm{Y}) = \mathbf{h}_{ij}(\mathbf{R}_\mathrm{X}) \cdot \boldsymbol{\delta}\mathbf{R}, \tag{1.24}$$

where

$$\begin{aligned} \mathbf{g}_i(\mathbf{R}_\mathrm{X}) &= \mathbf{c}^i(\mathbf{R}_\mathrm{X})^\mathrm{T} \frac{\partial \mathbf{H}^\mathrm{el}(\mathbf{R}_\mathrm{X})}{\partial \mathbf{R}} \mathbf{c}^i(\mathbf{R}_\mathrm{X}) \\ &= \frac{\partial V_i(\mathbf{R}_\mathrm{X})}{\partial \mathbf{R}}, \end{aligned} \tag{1.25}$$

and

$$\mathbf{h}_{ij}(\mathbf{R}_\mathrm{X}) = \mathbf{c}^i(\mathbf{R}_\mathrm{X})^\mathrm{T} \frac{\partial \mathbf{H}^\mathrm{el}(\mathbf{R}_\mathrm{X})}{\partial \mathbf{R}} \mathbf{c}^j(\mathbf{R}_\mathrm{X}). \tag{1.26}$$

Since the contributions from the P space alter the energy through second order,[8] the degeneracy at $\mathbf{R}_\mathrm{Y}$ is preserved through first order if the following conditions are satisfied. The first $M-1$ conditions come from the diagonal elements [Eq. (1.23)],

$$\mathbf{g}_{ij}(\mathbf{R}_\mathrm{X}) \cdot \boldsymbol{\delta}\mathbf{R} = \big[\mathbf{g}_i(\mathbf{R}_\mathrm{X}) - \mathbf{g}_j(\mathbf{R}_\mathrm{X})\big] \cdot \boldsymbol{\delta}\mathbf{R} = 0,\ 1 \leqslant i < j \leqslant M, \tag{1.27}$$

and the second $M(M-1)/2$ conditions come from the off-diagonal elements [Eq. (1.24)],

$$\mathbf{h}_{ij}(\mathbf{R}_\mathrm{X}) \cdot \boldsymbol{\delta}\mathbf{R} = 0,\ 1 \leqslant i < j \leqslant M. \tag{1.28}$$

Eqs. (3.31) and (3.28) indicate that the degeneracy of M–state crossings will be lifted, at first order of displacement $\boldsymbol{\delta}\mathbf{R}$, in $(M+2)(M-1)/2$ directions. For the most common two-state crossings, the two directions ($\mathbf{g}_{12}$ and $\mathbf{h}_{12}$) that lift the energy degeneracy form the so-called $\mathbf{g}$–$\mathbf{h}$ plane, and the potential surfaces of the two intersecting states have the shape of double cones at the crossing point, provided that $\mathbf{g}_{12}$ and $\mathbf{h}_{12}$ do not vanish identically. This kind of crossings are commonly called the conical intersections.

1.4 Spin-Flip Time-Dependent Density Functional Theory

In conventional linear-response time-dependent density functional theory (LR-TDDFT), the non-hermitian eigenvalue equation[9]

$$\begin{pmatrix} \mathbf{A} & \mathbf{B} \\ \mathbf{B}^* & \mathbf{A}^* \end{pmatrix} \begin{pmatrix} \mathbf{X} \\ \mathbf{Y} \end{pmatrix} = \omega \begin{pmatrix} \mathbf{1} & \mathbf{0} \\ \mathbf{0} & \mathbf{-1} \end{pmatrix} \begin{pmatrix} \mathbf{X} \\ \mathbf{Y} \end{pmatrix} \tag{1.29}$$

is solved for the excitation energies, ω. Here,

$$A_{ia,jb} = (\epsilon_a - \epsilon_i)\,\delta_{ij}\delta_{ab} + \langle ib|aj\rangle - C_{\mathrm{HF}}\langle ib|ja\rangle\langle ib|f^{xc}|aj\rangle, \tag{1.30}$$

and

$$B_{ia,jb} = \langle ij|ab\rangle - C_{\mathrm{HF}}\langle ij|ba\rangle + \langle ij|f^{xc}|ab\rangle\ . \tag{1.31}$$

The labels $i, j, \ldots$ and $a, b, \ldots$ represent occupied and virtual spin orbitals, respectively, and C_{HF} is the fraction of Hartree-Fock exchange included in the hybrid exchange-correlation functional.

Most photochemical or photophysical events involve the photo-excitation near Franck-Condon region and the relaxation back to ground state through conical intersections. As such, it's important that the electronic structure method is capable

of correctly describing the potential surfaces in the vicinity of conical intersections between the ground and excited states. LR-TDDFT is a computationally efficient method and it also provides good excitation energies for most chemical systems. However, it fails to predict the correct topography of the potential surfaces at the conical intersections between the reference state (which is usually the ground state) and the excited states.[10] This is due to the fact that the reference state is treated by density functional theory (DFT), thus the electronic correlations contained in the reference state and the excited states are unbalanced. Moreover, near state crossings between a DFT state and a LR-TDDFT state, the singlet instability problem of DFT may take place, which leads to imaginary excitation energies when solving Eq. (1.29).

The simplest extension of LR-TDDFT that corrects these problems is spin-flip (SF) TDDFT.[11,12] In SF-TDDFT, the reference DFT state has spin eigenvalue one unit higher than that of the target states. For example, if the target states are singlet states, then the reference DFT state is chosen as a high-spin triplet state and the target states are generated by single $\alpha \rightarrow \beta$ excitations. As a result, all the target states (including the ground state) are treated on the same footing, and the conical intersections amongst them can be correctly described. The details will be presented in the following chapters.

The formulation of SF-TDDFT largely resembles that of LR-TDDFT. The only difference comes from the $\alpha \rightarrow \beta$ excitations, which require the orbitals i, j, ..., in Eqs. (1.30) and (1.31) to be α spin orbitals and the orbitals a, b, ..., to be β spin

orbitals. As such, Eqs. (1.30) and (1.31) reduce to

$$A_{ia,jb} = (\epsilon_a - \epsilon_i)\,\delta_{ij}\delta_{ab} - C_{\mathrm{HF}}\langle ib|ja\rangle \tag{1.32}$$

and

$$B_{ia,jb} = 0\ . \tag{1.33}$$

This is the so-called collinear formulation of SF-TDDFT.[11] There is another form of SF-TDDFT called non-collinear SF-TDDFT, which can be derived from the two-component LR-TDDFT.[12] However, we will mainly focus on the collinear version in the following chapters.

CHAPTER 2

Analytic Derivative Couplings of LR-TDDFT: Quadratic Response Theory versus Pseudo-Wavefunction Approach

In this chapter, we introduce the formal derivation for the analytic derivative coupling of LR-TDDFT through quadratic response theory. We also compare it with the pseudo-wavefunction approach, in which the components that cause divergent problem are neglected. Finally, the current formulation is also valid for SF-TDDFT, and the details are presented in Chapter 3.

2.1 Introduction

The Born-Oppenheimer approximation breaks down when the energy gap between electronic states becomes small, where the electronic and nuclear degrees of freedom are coupled together and nuclear motions can induce electronic transitions. Nonadiabatic dynamics methods can be applied to go beyond the Born-Oppenheimer approximation and describe these non-radiative transitions.[6] The first-order nonadiabatic coupling matrix elements (derivative couplings) play a key role in these methods, since the transition probability between two electronic states is determined from the

derivative couplings. The derivative couplings are also important for methods to locate minimum-energy crossing points along conical seams,[13,14] which are useful to investigate photochemical processes in cases where *ab initio* nonadiabatic dynamics simulations are not affordable.

Analytic formulations of the derivative couplings can be obtained straightforwardly for wavefunction-based methods via direct differentiation of the electronic wavefunctions with respect to the nuclear coordinates. Examples include derivative couplings for multireference configuration interaction[15–18] (MRCI) and equation-of-motion coupled-cluster[19,20] theory. However, these are computationally expensive methods that can only be applied to small molecular systems. Recently, analytic derivative couplings have also been implemented for the configuration-interaction singles (CIS) method,[14,21] which is computationally inexpensive, but fails to provide even a qualitatively-correct description in many cases, owing to lack of dynamical correlation. Time-dependent density functional theory (TDDFT) is another inexpensive *ab initio* method for excited states, which often provides reasonable excited-state properties at a cost comparable to CIS.

The development of analytic derivative couplings for TDDFT is therefore important insofar as nonadiabatic *ab initio* molecular dynamics methods based on TDDFT may be efficient and accurate enough for large molecules. The most popular implementation of TDDFT is the version based on linear response (LR) of the electron density or density matrix for the noninteracting Kohn-Sham (KS) reference system.[9,22] As such, the electronic wavefunction is not defined in LR-TDDFT, which prevents the

use of direct differentiation of the wavefunction to calculate the derivative couplings.

Development of the formalism for TDDFT derivative couplings has been quite active recently.[14,23–29] Among these developments, only Send and Furche[24] and Li and Liu[26] achieved consistent formulations of TDDFT derivative couplings by using response theory exclusively. Their formulations capture all of the "Pulay terms" arising from atom-centered basis functions. Send and Furche[24] have implemented their formalism to obtain the TDDFT derivative couplings between the ground and excited electronic states, but the TDDFT derivative couplings between two excited states have only been derived conceptually,[26] with no published numerical examples so far based on response theory. It is well known that TDDFT fails to provide the correct dimensionality of the branching space for conical intersections that involve the reference state (which is usually the ground state),[10] which is caused by the imbalanced treatment of ground- versus excited-state electron correlation. No such topological issue exists for conical intersections between excited states.[10] As such, there is merit in implementing formally-exact analytic derivative couplings between TDDFT excited states that are derived solely from quadratic response theory.

In this work, we implement the derivative couplings between TDDFT excited states based on quadratic response theory. Numerical examples will compare these couplings to those derived based on a pseudo-wavefunction approach[28,29] (PWA), in which one treats the KS determinant as a wave function and computes analytic derivative couplings by direct differentiation.[14,28,29] Finally, we show that for spin-flip TDDFT,[11] the PWA formalism for the derivative couplings is formally equivalent to

quadratic response theory, which validates our recent implementation of the spin-flip TDDFT derivative couplings.[14]

2.2 Theory

The following notation is used throughout this work. Occupied and virtual KS orbitals are labeled $\phi_i, \phi_j, \phi_k, \phi_l, \ldots$ and $\phi_a, \phi_b, \phi_c, \phi_d, \ldots$, respectively, whereas $\phi_p, \phi_q, \phi_r, \phi_s, \ldots$ index arbitrary (occupied or virtual) KS orbitals. Greek letters $\mu, \nu, \lambda, \sigma, \ldots$ index atomic orbitals. All two-electron integrals will be written in physicists' notation.

2.2.1 Analytic derivative couplings between TDDFT excited states

In this section, we present a compact derivation of the analytic formulation of derivative couplings between two TDDFT excited states, based on the density matrix response theory. Similar derivations have been given previously by Send and Furche[24] and by Li and Liu.[26]

Quadratic response functions for exact states

The derivative coupling between two exact electronically-excited states $|I\rangle$ and $|J\rangle$ is

$$\mathbf{d}_{IJ} = \langle I|\hat{\boldsymbol{\nabla}}_{\mathbf{R}}|J\rangle = \frac{\langle I|\hat{\boldsymbol{\nabla}}_{\mathbf{R}}\hat{H}|J\rangle}{E_J - E_I} \,, \tag{2.1}$$

where $\mathbf{R}$ represents the nuclear coordinates, and $|I\rangle$ and $|J\rangle$ are the orthonormal eigenfunctions of the electronic Hamiltonian, $\hat{H}$, with eigenvalues E_I and E_J.

For any time-independent operator $\hat{A}$, the transition properties $\langle I|\hat{A}|J\rangle$ can be extracted from the residues of the quadratic response functions of $\hat{A}$.[26,30] The response

functions of $\hat{A}$ are those characterizing the time evolution of the average values

$$A(t) = \langle 0(t)|\hat{A}|0(t)\rangle \ , \tag{2.2}$$

where $|0(t)\rangle$ is the time-dependent electronic ground state when a general time-dependent field $W(t)$ is applied to the electronic system. The interaction between the field and the electronic system can be resolved into Fourier components V^{ω} according to[30]

$$V(t) = \int_{-\infty}^{+\infty} V^{\omega} e^{-i\omega t}\, d\omega \tag{2.3}$$

and the quadratic response functions of $\hat{A}$ at frequencies ω_α and ω_β are then[30]

$$\begin{aligned}
&\langle\langle A; V^{\omega_\alpha}, V^{\omega_\beta}\rangle\rangle \\
&= \hat{\mathcal{P}}(\alpha,\beta) \sum_{I,J} \Bigg[\frac{\langle 0|\hat{A}|I\rangle\langle I|\big(V^{\omega_\alpha} - \langle 0|V^{\omega_\alpha}|0\rangle\big)|J\rangle\langle J|V^{\omega_\beta}|0\rangle}{(\omega_\alpha + \omega_\beta - \omega_I)(\omega_\beta - \omega_J)} \\
&\quad + \frac{\langle 0|V^{\omega_\beta}|J\rangle\langle J|\big(V^{\omega_\alpha} - \langle 0|V^{\omega_\alpha}|0\rangle\big)|I\rangle\langle I|\hat{A}|0\rangle}{(\omega_\alpha + \omega_\beta + \omega_I)(\omega_\beta + \omega_J)} \\
&\quad - \frac{\langle 0|V^{\omega_\alpha}|I\rangle\langle I|\big(\hat{A} - \langle 0|\hat{A}|0\rangle\big)|J\rangle\langle J|V^{\omega_\beta}|0\rangle}{(\omega_\alpha + \omega_I)(\omega_\beta - \omega_J)} \Bigg] .
\end{aligned} \tag{2.4}$$

In this equation, $|0\rangle$ is the static electronic ground state, without the perturbation from the external field $W(t)$; V^{ω_α} and V^{ω_β} are the Fourier transform of $V(t)$ in Eq. (2.3) at frequencies ω_α and ω_β, respectively; $\hat{\mathcal{P}}(\alpha,\beta)$ is the permutation operator that generates all the permutations of α and β; and ω_I and ω_J are the excitation energies for the excited states $|I\rangle$ and $|J\rangle$.

For $I \neq J$, the quantity $\langle I|\hat{A}|J\rangle$ can be obtained from the residue of the quadratic response function:

$$\langle I|\hat{A}|J\rangle = \frac{-\lim\limits_{\omega_\alpha \to -\omega_I} (\omega_\alpha + \omega_I) \lim\limits_{\omega_\beta \to \omega_J} (\omega_\beta - \omega_J) \langle\langle A; V^{\omega_\alpha}, V^{\omega_\beta}\rangle\rangle}{\langle 0|V^{-\omega_I}|I\rangle\langle J|V^{\omega_J}|0\rangle}. \tag{2.5}$$

If we choose $\hat{A} = \hat{\boldsymbol{\nabla}}_{\mathbf{R}}$ as the nuclear derivative operator, then the derivative coupling $\mathbf{d}_{IJ}$ in Eq. (2.1) can be calculated using Eq. (2.5).

Quadratic response functions in TDKS systems

In order to calculate the derivative coupling $\mathbf{d}_{IJ}$ between TDDFT excited states, we need to derive the quadratic response functions of $\hat{\boldsymbol{\nabla}}_{\mathbf{R}}$ for time-dependent Kohn-Sham (TDKS) systems, whereas Eq. (2.4) gives the response function for exact states. In the TDKS system, the time-dependent ground state is approximated as a single determinant $\Phi(t)$ that provides the correct electron density at time t, and the expectation value of $\hat{\boldsymbol{\nabla}}_{\mathbf{R}}$ can be expressed as

$$\mathbf{D}_{\mathbf{R}}^{\mathrm{KS}}(t) \equiv \langle \Phi(t)|\hat{\boldsymbol{\nabla}}_{\mathbf{R}}|\Phi(t)\rangle = \sum_i \langle \psi_i(t)|\hat{\boldsymbol{\nabla}}_{\mathbf{R}}|\psi_i(t)\rangle, \tag{2.6}$$

where the $|\psi_i(t)\rangle$ are the occupied TDKS orbitals.

Given the perturbation from the external scalar potentials

$$V(t) = \lambda_\alpha V^{(\alpha)} e^{-i\omega_\alpha t} + \lambda_\beta V^{(\beta)} e^{-i\omega_\beta t}, \tag{2.7}$$

the TDKS orbitals may be expanded up to the second order in λ:[24]

$$|\psi_i(t)\rangle = e^{-i\epsilon_i t}\Big(|\phi_i\rangle + \lambda_\alpha|\psi_i^{(\alpha)}(t)\rangle + \lambda_\beta|\psi_i^{(\beta)}(t)\rangle + \lambda_\alpha\lambda_\beta|\psi_i^{(\alpha\beta)}(t)\rangle\Big), \tag{2.8}$$

where the $|\phi_i\rangle$ are the static KS orbitals, with orbital energies ϵ_i in the absence of the perturbation. Hereafter, we will set $\lambda_\alpha = \lambda_\beta = 1$ for simplicity.

The orbital $|\psi_i^{(\alpha)}(t)\rangle$ in Eq. (2.8) may be expanded in the basis of virtual static KS orbitals $|\phi_a\rangle$,[24]

$$|\psi_i^{(\alpha)}(t)\rangle = \sum_a \big(X_{ai}^{(\alpha)} e^{i\omega_\alpha t} + Y_{ai}^{(\alpha)} e^{-i\omega_\alpha t}\big)|\phi_a\rangle, \tag{2.9}$$

where $\mathbf{X}^{(\alpha)}$ and $\mathbf{Y}^{(\alpha)}$ are the virtual-occupied (VO) and occupied-virtual (OV) blocks of the linear density matrix response. These response functions satisfy the TDKS linear response equations,[22]

$$(\mathbf{\Lambda} - \omega_\alpha \mathbf{\Delta})\big|\mathbf{X}^{(\alpha)}, \mathbf{Y}^{(\alpha)}\big\rangle = -\big|\mathbf{P}^{(\alpha)}, \mathbf{Q}^{(\alpha)}\big\rangle \, . \tag{2.10}$$

Here,

$$\mathbf{\Lambda} = \begin{pmatrix} \mathbf{A} & \mathbf{B} \\ \mathbf{B} & \mathbf{A} \end{pmatrix} \tag{2.11}$$

is the orbital Hessian, whose matrix elements are

$$\begin{aligned} A_{ai,bj} = (\epsilon_a - \epsilon_i)\, \delta_{ij}\delta_{ab} + \langle \phi_a \phi_j | \phi_i \phi_b \rangle \\ - C_{\mathrm{HF}} \langle \phi_a \phi_j | \phi_b \phi_i \rangle + \langle \phi_a \phi_j | f^{\mathrm{xc}} | \phi_i \phi_b \rangle \end{aligned} \tag{2.12}$$

and

$$B_{ai,bj} = \langle \phi_a \phi_b | \phi_i \phi_j \rangle - C_{\mathrm{HF}} \langle \phi_a \phi_b | \phi_j \phi_i \rangle + \langle \phi_a \phi_b | f^{\mathrm{xc}} | \phi_i \phi_j \rangle \tag{2.13}$$

for a hybrid functional within the adiabatic approximation.[31] In Eqs. (4.2) and (4.3), C_{HF} is the fraction of the Hartree-Fock (HF) exchange, and f^{xc} is the exchange-correlation functional kernel. The matrix $\mathbf{\Delta}$ in Eq. (2.10) is defined as

$$\mathbf{\Delta} = \begin{pmatrix} \mathbf{1} & \mathbf{0} \\ \mathbf{0} & -\mathbf{1} \end{pmatrix}, \tag{2.14}$$

and $|\mathbf{P}^{(\alpha)}, \mathbf{Q}^{(\alpha)}\rangle$ represents the perturbation potential whose matrix elements are

$$P_{ai}^{(\alpha)} = \langle \phi_a | V^{\omega_\alpha} | \phi_i \rangle \tag{2.15}$$

$$Q_{ai}^{(\alpha)} = \langle \phi_i | V^{\omega_\alpha} | \phi_a \rangle \, . \tag{2.16}$$

Similarly, the quantity $|\psi_i^{(\alpha\beta)}(t)\rangle$ in Eq. (2.8) may be expanded as

$$\begin{aligned}|\psi_i^{(\alpha\beta)}(t)\rangle = &\sum_a \Big(X_{ai}^{(\alpha\beta)} e^{i(\omega_\alpha+\omega_\beta)t} + Y_{ai}^{(\alpha\beta)} e^{-i(\omega_\alpha+\omega_\beta)t}\Big)|\phi_a\rangle \\ &- \sum_{aj}\Big(X_{ai}^{(\alpha)} Y_{aj}^{(\beta)} e^{i(\omega_\alpha+\omega_\beta)t} + Y_{ai}^{(\alpha)} X_{aj}^{(\beta)} e^{-i(\omega_\alpha+\omega_\beta)t}\Big)|\phi_j\rangle \ ,\end{aligned} \tag{2.17}$$

where $\mathbf{X}^{(\alpha\beta)}$ and $\mathbf{Y}^{(\alpha\beta)}$ satisfy the TDKS quadratic response equations:[22]

$$\big(\mathbf{\Lambda} - (\omega_\alpha + \omega_\beta)\mathbf{\Delta}\big)\big|\mathbf{X}^{(\alpha\beta)}, \mathbf{Y}^{(\alpha\beta)}\big\rangle = -\big|\mathbf{R}^{(\alpha\beta)}, \mathbf{S}^{(\alpha\beta)}\big\rangle. \tag{2.18}$$

More details about Eq. (2.18) are presented in the Appendix.

The TDKS density operator can be calculated from the TDKS orbitals as

$$\hat{\gamma}(t) = \sum_i |\psi_i(t)\rangle\langle\psi_i(t)| \ . \tag{2.19}$$

Using Eqs. (2.8), (2.9) and (2.17), it is easy to calculate the linear and the quadratic response functions of the density operator. The linear response can be obtained by collecting the terms which are multiplied by $e^{i\omega_\alpha t}$,

$$\hat{\gamma}^{(\alpha)} = \sum_{ai}\Big(X_{ai}^{(\alpha)}|\phi_a\rangle\langle\phi_i| + Y_{ai}^{(\alpha)}|\phi_i\rangle\langle\phi_a|\Big) \ . \tag{2.20}$$

Likewise, collecting the terms that are multiplied by $e^{i(\omega_\alpha+\omega_\beta)t}$ gives us the quadratic response function,

$$\begin{aligned}\hat{\gamma}^{(\alpha\beta)} = &\sum_{ai}\Big(X_{ai}^{(\alpha\beta)}|\phi_a\rangle\langle\phi_i| + Y_{ai}^{(\alpha\beta)}|\phi_i\rangle\langle\phi_a|\Big) \\ &- \sum_{ija}\Big(X_{ai}^{(\alpha)}Y_{aj}^{(\beta)} + X_{ai}^{(\beta)}Y_{aj}^{(\alpha)}\Big)|\phi_j\rangle\langle\phi_i| \\ &+ \sum_{abi}\Big(X_{ai}^{(\alpha)}Y_{bi}^{(\beta)} + X_{ai}^{(\beta)}Y_{bi}^{(\alpha)}\Big)|\phi_a\rangle\langle\phi_b| \ .\end{aligned} \tag{2.21}$$

Equations (2.20) and (2.21) have the correct idempotent forms of the linear and the quadratic response functions of the density operator,[22] which validates the expansions in Eqs. (2.8), (2.9) and (2.17).

The quantity $\mathbf{D}_{\mathbf{R}}^{\mathrm{KS}}(t)$ in Eq. (2.6) can now be calculated by direct differentiation, using the formulas presented in Eqs. (2.8), (2.9) and (2.17). In order to get the quadratic response function of $\mathbf{D}_{\mathbf{R}}^{\mathrm{KS}}(t)$, we collect all the terms multiplied by $e^{i(\omega_\alpha+\omega_\beta)t}$ as before, which gives us

$$\begin{aligned}
\mathbf{D}_{\mathbf{R}}^{(\alpha\beta),\mathrm{KS}} &= \sum_{ai} \big(X_{ai}^{(\alpha\beta)} - Y_{ai}^{(\alpha\beta)}\big) \langle\phi_i|\hat{\boldsymbol{\nabla}}_{\mathbf{R}}|\phi_a\rangle \\
&- \sum_{ija} \big(X_{ai}^{(\alpha)} Y_{aj}^{(\beta)} + X_{ai}^{(\beta)} Y_{aj}^{(\alpha)}\big) \langle\phi_i|\hat{\boldsymbol{\nabla}}_{\mathbf{R}}|\phi_j\rangle \\
&+ \sum_{abi} \big(X_{bi}^{(\alpha)} Y_{ai}^{(\beta)} + X_{bi}^{(\beta)} Y_{ai}^{(\alpha)}\big) \langle\phi_a|\hat{\boldsymbol{\nabla}}_{\mathbf{R}}|\phi_b\rangle \\
&- \sum_{ai} \big(X_{ai}^{(\alpha)} \hat{\boldsymbol{\nabla}}_{\mathbf{R}} Y_{ai}^{(\beta)} + Y_{ai}^{(\beta)} \hat{\boldsymbol{\nabla}}_{\mathbf{R}} X_{ai}^{(\alpha)}\big) \\
&+ \sum_{ai} \big(Y_{ai}^{(\alpha)} \hat{\boldsymbol{\nabla}}_{\mathbf{R}} X_{ai}^{(\beta)} + Y_{ai}^{(\beta)} \hat{\boldsymbol{\nabla}}_{\mathbf{R}} X_{ai}^{(\alpha)}\big) \,. \qquad (2.22)
\end{aligned}$$

Derivative couplings between TDDFT excited states

Having derived the quadratic response function of $\mathbf{D}_{\mathbf{R}}^{\mathrm{KS}}(t)$, we just need to extract the derivative couplings from the residues of $\mathbf{D}_{\mathbf{R}}^{(\alpha\beta),\mathrm{KS}}$ in Eq. (2.22) following the same procedure shown in Eq. (2.5).

It is well known[9] that by using Eq. (2.10) and the spectral expansion, the quantity $|\mathbf{X}^{(\alpha)}, \mathbf{Y}^{(\alpha)}\rangle$ can be expressed as

$$|\mathbf{X}^{(\alpha)}, \mathbf{Y}^{(\alpha)}\rangle = \sum_I \left(\frac{|\mathbf{X}_I, \mathbf{Y}_I\rangle\langle\mathbf{X}_I, \mathbf{Y}_I|}{\omega_\alpha - \omega_I} - \frac{|\mathbf{Y}_I, \mathbf{X}_I\rangle\langle\mathbf{Y}_I, \mathbf{X}_I|}{\omega_\alpha + \omega_I} \right) |\mathbf{P}^{(\alpha)}, \mathbf{Q}^{(\alpha)}\rangle, \qquad (2.23)$$

where $|\mathbf{X}_I, \mathbf{Y}_I\rangle$ and $|\mathbf{Y}_I, \mathbf{X}_I\rangle$ satisfy the following pseudo-eigenvalue equations:

$$\begin{aligned}(\mathbf{\Lambda} - \omega_I \mathbf{\Delta})|\mathbf{X}_I, \mathbf{Y}_I\rangle &= \mathbf{0} \\ (\mathbf{\Lambda} + \omega_I \mathbf{\Delta})|\mathbf{Y}_I, \mathbf{X}_I\rangle &= \mathbf{0} \ ,\end{aligned} \tag{2.24}$$

subject to the orthonormality conditions

$$\begin{aligned}\langle \mathbf{X}_I, \mathbf{Y}_I|\mathbf{\Delta}|\mathbf{X}_J, \mathbf{Y}_J\rangle &= \delta_{IJ} \\ \langle \mathbf{Y}_I, \mathbf{X}_I|\mathbf{\Delta}|\mathbf{Y}_J, \mathbf{X}_J\rangle &= -\delta_{IJ} \ .\end{aligned} \tag{2.25}$$

From Eqs. (2.15), (2.16) and (2.23), the residues of $|\mathbf{X}^{(\alpha)}, \mathbf{Y}^{(\alpha)}\rangle$ and $|\mathbf{X}^{(\beta)}, \mathbf{Y}^{(\beta)}\rangle$ at frequencies $-\omega_I$ and ω_J can be written as[9,26]

$$\begin{aligned}&\lim_{\omega_\alpha \to -\omega_I} (\omega_\alpha + \omega_I)|\mathbf{X}^{(\alpha)}, \mathbf{Y}^{(\alpha)}\rangle \\ &\quad = -|\mathbf{Y}_I, \mathbf{X}_I\rangle\langle \mathbf{Y}_I, \mathbf{X}_I|\mathbf{P}^{-\omega_I}, \mathbf{Q}^{-\omega_I}\rangle \\ &\quad = -|\mathbf{Y}_I, \mathbf{X}_I\rangle\langle 0|V^{-\omega_I}|I\rangle\end{aligned} \tag{2.26}$$

and

$$\begin{aligned}&\lim_{\omega_\beta \to \omega_J} (\omega_\beta - \omega_J)|\mathbf{X}^{(\beta)}, \mathbf{Y}^{(\beta)}\rangle \\ &\quad = |\mathbf{X}_J, \mathbf{Y}_J\rangle\langle \mathbf{X}_J, \mathbf{Y}_J|\mathbf{P}^{\omega_J}, \mathbf{Q}^{\omega_J}\rangle \\ &\quad = |\mathbf{X}_J, \mathbf{Y}_J\rangle\langle J|V^{\omega_J}|0\rangle \ .\end{aligned} \tag{2.27}$$

Finally, we can extract the derivative coupling between two TDDFT excited states from the residues of $\mathbf{D}_{\mathbf{R}}^{(\alpha\beta),\mathrm{KS}}$ in Eq. (2.22) by using Eqs. (2.26), (2.27) and $|\mathbf{X}_{IJ}, \mathbf{Y}_{IJ}\rangle$

as derived in the Appendix. The result is

$$\begin{aligned}
\mathbf{d}_{IJ}^{\mathrm{KS}} = & \sum_{ai} \big(X_{ai}^{IJ} - Y_{ai}^{IJ}\big) \langle \phi_i | \hat{\boldsymbol{\nabla}}_{\mathbf{R}} | \phi_a \rangle \\
& - \sum_{ija} \big(X_{ai}^{J} X_{aj}^{I} + Y_{ai}^{I} Y_{aj}^{J}\big) \langle \phi_i | \hat{\boldsymbol{\nabla}}_{\mathbf{R}} | \phi_j \rangle \\
& + \sum_{abi} \big(X_{bi}^{J} X_{ai}^{I} + Y_{bi}^{I} Y_{ai}^{J}\big) \langle \phi_a | \hat{\boldsymbol{\nabla}}_{\mathbf{R}} | \phi_b \rangle \\
& + \sum_{ai} \frac{\lim\limits_{\omega_\beta \to \omega_J} (\omega_\beta - \omega_J)(X_{ai}^{I} \hat{\boldsymbol{\nabla}}_{\mathbf{R}} X_{ai}^{(\beta)} - Y_{ai}^{I} \hat{\boldsymbol{\nabla}}_{\mathbf{R}} Y_{ai}^{(\beta)})}{\langle J | V^{\omega_J} | 0 \rangle}.
\end{aligned} \tag{2.28}$$

The last term in Eq. (2.28) can be calculated following the procedure given by Li and Liu;[26] details are shown in the Appendix. By substituting Eq. (A.14) into Eq. (2.28), the final expression for the derivative coupling between two TDDFT excited states reads

$$\begin{aligned}
\mathbf{d}_{IJ}^{\mathrm{KS}} = & \sum_{ai} \big(X_{ai}^{IJ} - Y_{ai}^{IJ}\big) \langle \phi_i | \hat{\boldsymbol{\nabla}}_{\mathbf{R}} | \phi_a \rangle \\
& - \sum_{ija} \big(X_{ai}^{J} X_{aj}^{I} + Y_{ai}^{I} Y_{aj}^{J}\big) \langle \phi_i | \hat{\boldsymbol{\nabla}}_{\mathbf{R}} | \phi_j \rangle \\
& + \sum_{abi} \big(X_{bi}^{J} X_{ai}^{I} + Y_{bi}^{I} Y_{ai}^{J}\big) \langle \phi_a | \hat{\boldsymbol{\nabla}}_{\mathbf{R}} | \phi_b \rangle \\
& + \sum_{ijab} \Big[X_{ai}^{I} (\hat{\boldsymbol{\nabla}}_{\mathbf{R}} A_{ai,bj}) X_{bj}^{J} + Y_{ai}^{I} \hat{\boldsymbol{\nabla}}_{\mathbf{R}} A_{ai,bj}) Y_{bj}^{J} \\
& \quad + X_{ai}^{I} (\hat{\boldsymbol{\nabla}}_{\mathbf{R}} B_{ai,bj}) Y_{bj}^{J} \\
& \quad + Y_{ai}^{I} (\hat{\boldsymbol{\nabla}}_{\mathbf{R}} B_{ai,bj}) X_{bj}^{J} \Big] (\omega_J - \omega_I)^{-1} \ .
\end{aligned} \tag{2.29}$$

In Eq. (2.29), the nuclear derivatives of the orbital rotation Hessians $\hat{\boldsymbol{\nabla}}_{\mathbf{R}}\mathbf{A}$ and $\hat{\boldsymbol{\nabla}}_{\mathbf{R}}\mathbf{B}$ can be obtained from the conventional TDDFT gradient formalism.[32] The nuclear derivatives of the KS orbitals, $\hat{\boldsymbol{\nabla}}_{\mathbf{R}} |\phi_p\rangle$, can be calculated as in previous work.[14,21,28]

2.2.2 Nonadiabatic coupling vectors between TDDFT excited states

The nonadiabatic coupling vector (NACV) along with the energy difference gradient vector can be used to determine the branching plane at conical intersections.[8] For states $|I\rangle$ and $|J\rangle$ that are exact eigenstates of $\hat{H}$, the NACV may be defined as[8]

$$\begin{aligned}\mathbf{h}_{IJ} &\equiv \langle I|(\hat{\boldsymbol{\nabla}}_{\mathbf{R}}\hat{H})|J\rangle = \mathbf{d}_{IJ}(E_J - E_I) \\ &= \left\langle I \left| \left(\hat{\boldsymbol{\nabla}}_{\mathbf{R}} \sum_{i=1}^{N} \hat{V}_{\mathrm{en}}(i) \right) \right| J \right\rangle \ ,\end{aligned} \tag{2.30}$$

where $\hat{V}_{\mathrm{en}}(i)$ is the electron-nucleus Coulomb potential for the ith electron.

Since $\mathbf{d}_{IJ}^{\mathrm{KS}}$ in Eq.(2.29) was derived from response theory and is therefore formally exact, we can simply define the NACV between TDDFT excited states as

$$\mathbf{h}_{IJ}^{\mathrm{KS}} = (\omega_J - \omega_I)\mathbf{d}_{IJ}^{\mathrm{KS}} \ . \tag{2.31}$$

In addition, we can also derive $\mathbf{h}_{IJ}^{\mathrm{KS}}$ from response theory, where we replace the operator $\hat{\boldsymbol{\nabla}}_{\mathbf{R}}$ in Eq. (2.6) by $\hat{\boldsymbol{\nabla}}_{\mathbf{R}}\hat{V}_{\mathrm{en}}$. Following the same procedure used to derive $\mathbf{d}_{IJ}^{\mathrm{KS}}$, we easily obtain

$$\begin{aligned}\mathbf{h}_{IJ}^{\mathrm{KS}} = &\sum_{ai} \big(X_{ai}^{IJ} + Y_{ai}^{IJ}\big) \langle \phi_i | (\hat{\boldsymbol{\nabla}}_{\mathbf{R}}\hat{V}_{\mathrm{en}}) | \phi_a \rangle \\ &- \sum_{ija} \big(X_{ai}^{J} X_{aj}^{I} + Y_{ai}^{I} Y_{aj}^{J}\big) \langle \phi_i | (\hat{\boldsymbol{\nabla}}_{\mathbf{R}}\hat{V}_{\mathrm{en}}) | \phi_j \rangle \\ &+ \sum_{abi} \big(X_{bi}^{J} X_{ai}^{I} + Y_{bi}^{I} Y_{ai}^{J}\big) \langle \phi_a | (\hat{\boldsymbol{\nabla}}_{\mathbf{R}}\hat{V}_{\mathrm{en}}) | \phi_b \rangle \ .\end{aligned} \tag{2.32}$$

Equations (2.31) and (2.32) should be equivalent in the limit that exact density functional and frequency-dependent functional kernel are used. Of course, the functionals used in practice are approximate, and the frequency-independent adiabatic approximation[31] is almost always invoked. As such, the NACVs obtained from

Eqs. (2.31) and Eq. (2.32) will generally differ. Note that Eq. (2.32) does not involve nuclear derivatives of $\mathbf{A}$ or $\mathbf{B}$, which is very different from the NACV defined within the configuration interaction singles (CIS) theory.[14]

2.2.3 Discussion

Equation (2.29) for the derivative coupling $\mathbf{d}_{IJ}^{\mathrm{KS}}$ between two TDDFT excited states is equivalent to the expression derived by Li and Liu[26] [Eq. (125) of Ref. 26]. Those authors started from the equation-of-motion formalism, and obtained the derivative couplings for arbitrary excitation subspaces. Here for TDDFT, the excitation subspace is limited to single excitations, considering terms up to second-order response.

The first three lines on the right side of Eq. (2.29) are the VO, OV, OO, and VV blocks of the transition density matrix between two excited states (where O means "occupied" and V means "virtual"), multiplied by the "half derivative" of the corresponding KS orbital overlap matrices, $\langle\phi_p|\hat{\boldsymbol{\nabla}}_{\mathbf{R}}|\phi_q\rangle$. These terms are similar as the "configuration state function (CSF) contribution" in the formulation of MRCI derivative couplings.[15–18] The terms involving the nuclear derivatives of the orbital rotation Hessian in Eq. (2.29) resembles the "CI contribution", in the language of MRCI derivative couplings.

In CIS theory, the VO and OV blocks of the transition density matrix between two CIS states is zero because only single excitations are considered. By directly following the CIS procedure[28,29] to calculate TDDFT derivative couplings (pseudo-wavefunction approach), the terms including $|\mathbf{X}_{IJ}, \mathbf{Y}_{IJ}\rangle$ are neglected. This affords

derivative couplings

$$\begin{aligned}\mathbf{d}_{IJ}^{\mathrm{PWA}} = &-\sum_{ija}\big(X_{ai}^{J}X_{aj}^{I}+Y_{ai}^{I}Y_{aj}^{J}\big)\langle\phi_i|\hat{\boldsymbol{\nabla}}_{\mathbf{R}}|\phi_j\rangle \\ &+\sum_{abi}\big(X_{bi}^{J}X_{ai}^{I}+Y_{bi}^{I}Y_{ai}^{J}\big)\langle\phi_a|\hat{\boldsymbol{\nabla}}_{\mathbf{R}}|\phi_b\rangle \\ &+\sum_{ijab}\Big[X_{ai}^{I}(\hat{\boldsymbol{\nabla}}_{\mathbf{R}}A_{ai,bj})X_{bj}^{J}+Y_{ai}^{I}(\hat{\boldsymbol{\nabla}}_{\mathbf{R}}A_{ai,bj})Y_{bj}^{J} \\ &\quad +X_{ai}^{I}(\hat{\boldsymbol{\nabla}}_{\mathbf{R}}B_{ai,bj})Y_{bj}^{J} \\ &\quad +Y_{ai}^{I}(\hat{\boldsymbol{\nabla}}_{\mathbf{R}}B_{ai,bj})X_{bj}^{J}\Big](\omega_J-\omega_I)^{-1}\ .\end{aligned} \tag{2.33}$$

Interestingly, for spin-flip TDDFT (SF-TDDFT) with either collinear[11] or non-collinear[12] kernels, the right side of Eq. (A.9) vanishes. [For spin-flipping excitations, it is straightforward to show that $\partial F_{pq}/\partial P_{rs} = 0$ and $\partial^2 F_{pq}/\partial P_{rs}\partial P_{r's'} = 0$ in Eqs. (A.6) and (A.7).[11,12]] Thus, the VO and OV blocks of the transition density matrix between two SF-TDDFT states is zero. In other words, for SF-TDDFT, the derivative coupling calculated by the PWA[14] is exactly the same as the one calculated by the quadratic response approach (QRA) shown in Eq. (2.29).

The cost of computing $\mathbf{d}_{IJ}^{\mathrm{KS}}$ in Eq. (2.29) is greater than the cost of computing $\mathbf{d}_{IJ}^{\mathrm{PWA}}$, since an additional set of linear equations [namely, Eq. (A.9)] needs to be solved. The cost of solving Eq. (A.9) is about the same as a single TDDFT excited-state gradient calculation. As such, it is important to quantify any differences between $\mathbf{d}_{IJ}^{\mathrm{KS}}$ and $\mathbf{d}_{IJ}^{\mathrm{PWA}}$, in order to determine situations in which the PWA is capable of providing accurate derivative couplings. This is the topic of the next section.

2.3 Numerical examples

TDDFT derivative couplings $\mathbf{d}_{IJ}^{\mathrm{KS}}$ from quadratic response theory [Eq. (2.29)] have been implemented in a locally-modified version of the Q-Chem program,[33] whereas derivative couplings with the PWA have been implemented previously.[14,28,29,34] Here, we numerically compare the QRA and PWA results in order to determine the importance of the contribution from the VO and OV blocks of the transition density matrix between TDDFT excited states.

We will also compare TDDFT derivative couplings to full configuration interaction (FCI) results, and to CIS results. The effects of the Tamm-Dancoff approximation[35] (TDA) on the TDDFT results are also considered. For derivative couplings $\mathbf{d}_{IJ}^{\mathrm{KS}}$, we take the TDA to mean that the vectors $\mathbf{Y}^I$, $\mathbf{Y}^J$ and $\mathbf{Y}^{IJ}$ in Eqs. (2.29) and (A.9) are set to zero.

The CASSCF module[36,37] of the MolPro program[38] was used to perform the FCI calculations. The derivative couplings between the FCI excited states were calculated using finite central differences with a step size of 0.01 a.u. All the other calculations were performed using Q-Chem.[33]

2.3.1 Difference between $\mathbf{d}_{IJ}^{\mathrm{KS}}$ and $\mathbf{d}_{IJ}^{\mathrm{PWA}}$

When the energy gap between states I and J becomes small, the "CI contribution" [last three lines in Eq. (2.29)] should dominate $\mathbf{d}_{IJ}^{\mathrm{KS}}$, since these terms contain the inverse energy gap $(\omega_J - \omega_I)^{-1}$. As such, we may expect that the difference between $\mathbf{d}_{IJ}^{\mathrm{KS}}$ and $\mathbf{d}_{IJ}^{\mathrm{PWA}}$ is small in the curve-crossing regions.

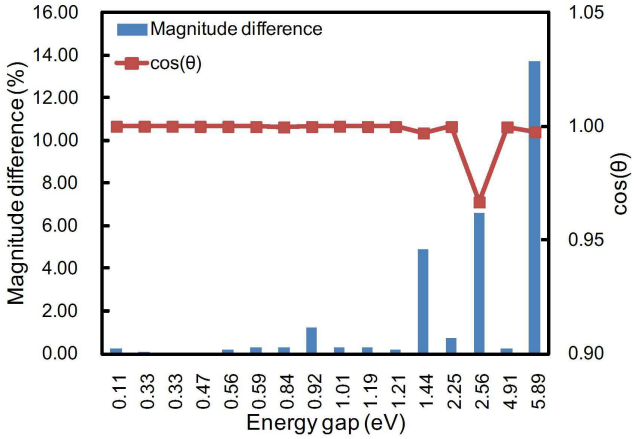

Figure 2.1: Differences between $\mathbf{d}_{IJ}^{\mathrm{KS}}$ and $\mathbf{d}_{IJ}^{\mathrm{PWA}}$ at various energy gaps. The derivative couplings were calculated by TDDFT/TDA at the PBE0/6-31G** level. Full (non-TDA) TDDFT results are similar and have been omitted. The magnitude difference is defined in Eq. (2.34) and $\cos\theta$ in Eq. (2.35). Note that the horizontal scale is not linear, but rather consists of the 16 different gaps that were computed for the 8 molecules in the test set.

To examine the energy-gap dependence of $\mathbf{d}_{IJ}^{\mathrm{KS}} - \mathbf{d}_{IJ}^{\mathrm{PWA}}$, we calculated these quantities for a test set that consists of formaldehyde, ethene, benzene, adenine, thymine, uracil, cytosine and azulene. Each molecule was distorted slightly from its global minimum geometry so that all the molecules have C_1 symmetry and we can safely calculate the derivative couplings between any pairs of excited states with the same spin multiplicity. The S_1/S_2 and S_1/S_3 derivative couplings were calculated for each molecule, at the PBE0/6-31G** level.[39] Results are shown in Fig. 2.1, where we characterize the difference between $\mathbf{d}_{IJ}^{\mathrm{KS}}$ and $\mathbf{d}_{IJ}^{\mathrm{PWA}}$ in terms of the difference in their norms,

$$\text{Magnitude difference} = \frac{||\mathbf{d}_{IJ}^{\mathrm{KS}}|| - ||\mathbf{d}_{IJ}^{\mathrm{PWA}}||}{||\mathbf{d}_{IJ}^{\mathrm{PWA}}||} \times 100\% \,, \tag{2.34}$$

and also in terms of the angle θ between the two derivative coupling vectors:

$$\cos\theta = \frac{\mathbf{d}_{IJ}^{\mathrm{KS}} \cdot \mathbf{d}_{IJ}^{\mathrm{PWA}}}{||\mathbf{d}_{IJ}^{\mathrm{KS}}|| \times ||\mathbf{d}_{IJ}^{\mathrm{PWA}}||} \,. \tag{2.35}$$

From Fig. 2.1 we see that there is almost no difference between $\mathbf{d}_{IJ}^{\mathrm{KS}}$ and $\mathbf{d}_{IJ}^{\mathrm{PWA}}$ for systems with energy gaps < 1 eV. Only for larger gaps does the magnitude difference [Eq. (2.34)] approach 5–12%, and even in these cases the vectors $\mathbf{d}_{IJ}^{\mathrm{KS}}$ and $\mathbf{d}_{IJ}^{\mathrm{PWA}}$ are nearly parallel. This suggests that for optimizations of minimum-energy crossing points along conical seams, where only the direction of the derivative coupling is important, $\mathbf{d}_{IJ}^{\mathrm{PWA}}$ can be safely used with lower computational cost. As such, we conclude that for molecules with low symmetry, $\mathbf{d}_{IJ}^{\mathrm{KS}}$ and $\mathbf{d}_{IJ}^{\mathrm{PWA}}$ can usually be used interchangeably between the states with energy gaps as large as 6 eV. (For highly symmetric molecules, such as Li_2 as considered below, $\mathbf{d}_{IJ}^{\mathrm{KS}}$ and $\mathbf{d}_{IJ}^{\mathrm{PWA}}$ may exhibit

larger differences even for small-gap systems, and the choice between the two must be considered more carefully.)

2.3.2 Geometric phase effect around conical intersections

According to the geometric phase effect, the nuclear wavefunction accumulates an additional (geometric) phase as it is transported around a path that encloses a conical intersection. This compensates for the phase change of the adiabatic electronic wavefunction.[8] The accumulated phase ϕ is related to the derivative couplings according to

$$\phi \equiv \oint_{\mathbb{C}} \mathbf{d}_{IJ} \cdot d\mathbf{R} = \pi \ , \tag{2.36}$$

where loop $\mathbb{C}$ encloses a conical intersection. (Here, we define ϕ as the indicated integral around $\mathbb{C}$. For exact derivative couplings, $\phi = \pi$,[8] though a different value of the integral might be obtained using approximate derivative couplings.)

It has been shown previously that $\mathbf{d}_{IJ}^{\mathrm{PWA}}$ satisfies Eq. (2.36) for both full TDDFT calculations[29] and TDDFT/TDA calculations.[28] This is hardly surprising, since the PWA is by nature a wavefunction-based method. It is not clear whether $\mathbf{d}_{IJ}^{\mathrm{KS}}$ derived from response theory should satisfy Eq. (2.36), although given that the difference between $\mathbf{d}_{IJ}^{\mathrm{KS}}$ and $\mathbf{d}_{IJ}^{\mathrm{PWA}}$ is small near crossing points, we might anticipate this relationship is satisfied for $\mathbf{d}_{IJ}^{\mathrm{KS}}$ as well.

In this work, we calculated the geometric phase ϕ for H_2O and for uracil. For H_2O, we computed ϕ at the B3LYP/6-31G** level[40,41] for the S_3/S_4 conical intersection, and for uracil we calculated ϕ at the PBE0/6-31G** level[39] for the S_1/S_2 intersection. The loop $\mathbb{C}$ was chosen as a circle in the branching plane with a radius of 0.001 Å and

Table 2.1: Line integrals of the TDDFT derivative couplings along closed circular loops that enclose a conical intersection. These loops are centered either at the minimum-energy crossing point ($\mathbf{R}_{\text{mex}}$) or at a point displaced 0.1 Å in the $\mathbf{g}_{IJ}$ direction. Geometric phases ϕ are given in units of π, and values in parenthesis are computed using the Tamm-Dancoff approximation.

	Centered at $\mathbf{R}_{\text{mex}}$		Displaced in $\mathbf{g}_{IJ}$ direction	
Molecule	ϕ^{QRA}/π	ϕ^{PWA}/π	ϕ^{QRA}/π	ϕ^{PWA}/π
H_2O	0.9997 (1.0001)	1.0003 (1.0000)	0.0043 (0.0119)	0.0110 (0.0120)
Uracil	0.9978 (0.9999)	0.9978 (0.9999)	0.0013 (0.0014)	0.0014 (0.0014)

a center near the minimum-energy crossing point, as detailed below. The branching plane was determined as the span of the vectors $\mathbf{g}_{IJ}$ and $\mathbf{h}_{IJ}$, where

$$\mathbf{g}_{IJ} = \hat{\boldsymbol{\nabla}}_{\mathbf{R}}(\omega_J - \omega_I) \tag{2.37}$$

is the energy difference gradient vector. The vector $\mathbf{h}_{IJ}$ is the NACV, which is given by $\mathbf{h}_{IJ}^{\text{KS}}$ Eq. (2.31) with the quadratic response approach. Within the pseudo-wavefunction approach,

$$\mathbf{h}_{IJ}^{\text{PWA,TDDFT}} = \mathbf{d}_{IJ}^{\text{PWA}}(\omega_J - \omega_I) \ , \tag{2.38}$$

or upon invoking the TDA,

$$\mathbf{h}_{IJ}^{\text{PWA,TDA}} = \sum_{ijab} X_{ai}^{I}\big(\hat{\boldsymbol{\nabla}}_{\mathbf{R}} A_{ai,bj}\big) X_{bj}^{J} \ . \tag{2.39}$$

Table 2.1 lists the geometric phases computed along two different circular loops, one that is centered at the minimum-energy crossing point ($\mathbf{R}_{\text{mex}}$) and another whose center is displaced from $\mathbf{R}_{\text{mex}}$ by 0.1 Å along a unit vector in the direction $\mathbf{g}_{IJ}$. For the loop centered at $\mathbf{R}_{\text{mex}}$, both $\mathbf{d}_{IJ}^{\text{KS}}$ and $\mathbf{d}_{IJ}^{\text{PWA}}$ afford the correct phase, $\phi = \pi$. For

the loop whose center is displaced from $\mathbf{R}_{\text{mex}}$, however, both methods afford a phase $\phi \approx 0$, indicating that this displaced loop does *not* enclose a conical intersection. (This is expected, since we displaced the center of this path along one of the branching-plane degrees of freedom.) Overall, the geometric-phase behavior of both $\mathbf{d}_{IJ}^{\text{KS}}$ and $\mathbf{d}_{IJ}^{\text{PWA}}$ is correct.

2.3.3 Comparison with FCI derivative couplings

In this section, we have calculated the derivative couplings for H_2, He_2, Li_2 and H_3 using FCI, CIS, time-dependent Hartree-Fock (TDHF) theory and TDDFT. Both the QRA and PWA derivative couplings were tested in the TDHF and the TDDFT calculations. Similar results were obtained using B3LYP and PBE0, so only the latter are shown. As the z axis was taken to be the molecular axis, only the z components of the derivative couplings are non-zero.

H_2

Derivative couplings for the 2 $^1\Sigma_g^+$ and 3 $^1\Sigma_g^+$ states of H_2, computed in the aug-cc-pVDZ basis set, are shown in Figs. 2.2 and 2.3. For bond lengths larger than 2.25 bohr, both states have strong double excitation character that cannot be captured by CIS, TDHF or TDDFT, so only our plots terminate at 2.25 bohr.

The CIS and TDHF-PWA methods are formally similar, in that both are wavefunction-based approaches that include only Hartree-Fock exchange, with excitation spaces that are truncated at single excitations. Derivative couplings computed using the these two methods are similar to one another, and agree quite well with FCI results

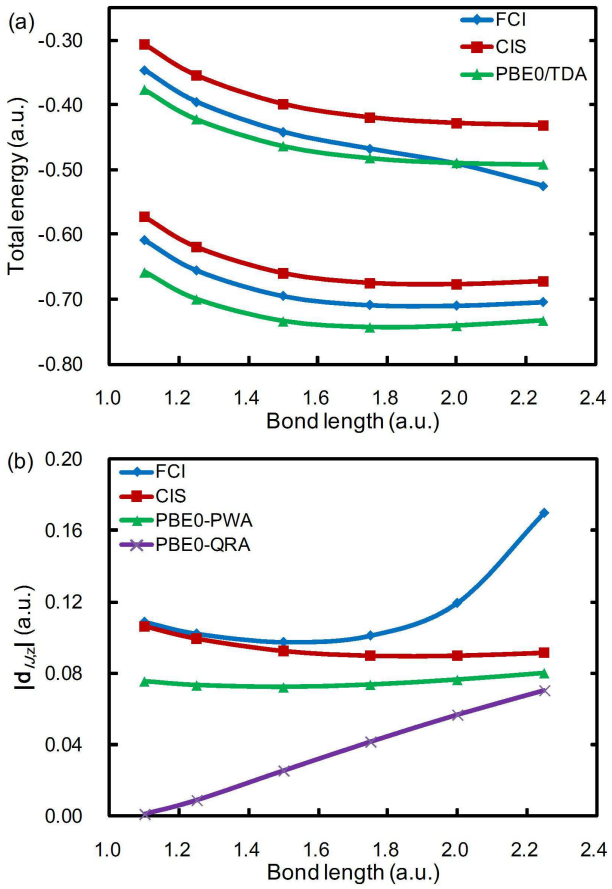

Figure 2.2: (a) Energies of the $2\ ^1\Sigma_g^+$ and $3\ ^1\Sigma_g^+$ states of H_2 computed at the FCI, CIS, and TDDFT/TDA levels, using the aug-cc-pVDZ basis set and the PBE0 functional for TDDFT. (b) Absolute value of the z-component of the derivative coupling between these two states, computed using the same methods.

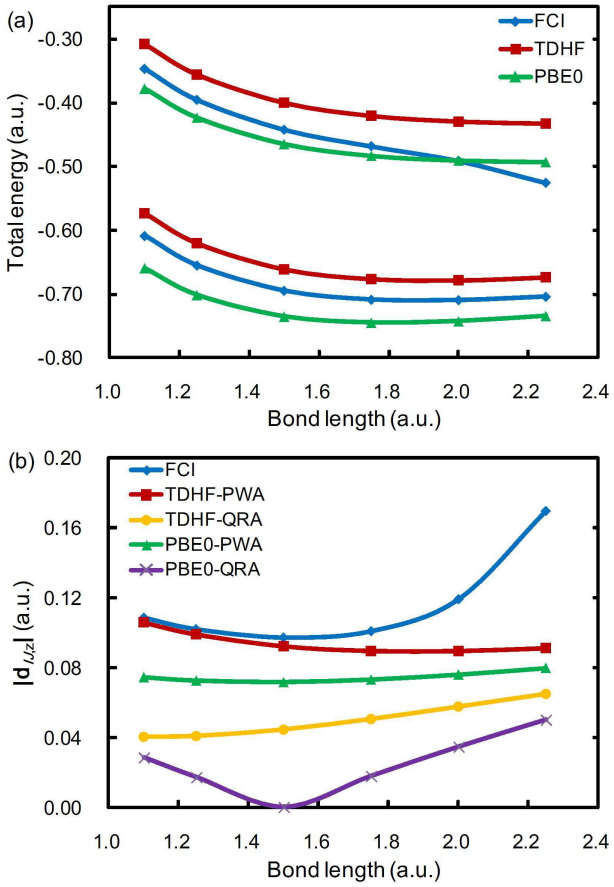

Figure 2.3: (a) Energies of the 2 $^1\Sigma_g^+$ and 3 $^1\Sigma_g^+$ states of H_2 computed at the FCI, TDHF, and TDDFT levels, using the aug-cc-pVDZ basis set and the PBE0 functional for TDDFT. (b) Absolute value of the z-component of the derivative coupling between these two states, computed using the same methods.

for bond lengths ranging from 1.0–1.6 a.u. [see Figures 2.2(b) and 2.3(b)]. For larger bond lengths, however, these methods fail to reproduce the increase in d_{IJ} as a function of bond length that is observed in the FCI results. This failure can be understood by examining the potential energy surfaces (PESs) of the $3^1\Sigma_g^+$ state, whose curvature is incorrectly predicted by CIS and TDHF calculations for bond lengths larger than 1.6 a.u. The PBE0-PWA derivative couplings, both with or without the TDA, agree qualitatively with the CIS and TDHF-PWA results (and are thus incorrect for longer bond lengths), owing to the similar wavefunction *ansatz* that is used, and the good agreement among the PESs calculated by CIS, TDHF and TDDFT

On the other hand, TDHF-QRA and PBE0-QRA derivative couplings are in poor agreement with FCI results even for shorter bond lengths. A possible explanation is accumulation of errors when calculating the VO and OV blocks of the transition density matrix between the two TDDFT excited states. From Eqs. (A.6), (A.7), and (A.9), we know that $|\mathbf{X}_{IJ}, \mathbf{Y}_{IJ}\rangle$ is based on $|\mathbf{X}_I, \mathbf{Y}_I\rangle$ and $|\mathbf{X}_J, \mathbf{Y}_J\rangle$. Although TDDFT may provide good excitation energies, it is possible that the transition properties $|\mathbf{X}_I, \mathbf{Y}_I\rangle$ and $|\mathbf{X}_J, \mathbf{Y}_J\rangle$ are less accurate. Large errors might then accumulate in $|\mathbf{X}_{IJ}, \mathbf{Y}_{IJ}\rangle$, which is obtained by solving a set of linear equations [Eq. (A.9)]. This is confirmed by comparing the transition density matrices calculated by TDDFT and FCI.

He_2

For He_2, we examine derivative couplings between the 3 $^1\Sigma_g^+$ and 5 $^1\Sigma_g^+$ states, both of which have strong single-excitation character. The 3 $^1\Sigma_g^+$ state is characterized

by a single excitation from the $1\sigma_u$ molecular orbital (MO) to the $2\sigma_u$ MO, and the $5\ ^1\Sigma_g^+$ state involves $1\sigma_u \rightarrow 3\sigma_u$ excitation. Potential energy curves and derivative couplings are plotted in Figs. 2.4 and 2.5.

The CIS and TDHF methods reproduce all the features of the FCI PES, even though the total energies are a little shifted from the FCI values. This leads to good agreement among CIS, TDHF-PWA, and FCI derivative couplings. Surprisingly, the TDHF-QRA derivative couplings exhibit large errors and qualitatively incorrect behavior at bond lengths shorter than 4.0 bohr, for reasons that are unclear but which may be another example of the error accumulation about which we have already speculated.

TDDFT potential curves fail to capture the state crossing between $3^1\Sigma_g^+$ and a higher excited state at bond lengths of 3.5–4.0 bohr, and moreover the double-well feature of the $5^1\Sigma_g^+$ state is also not correctly described in these calculations. Consequently, the TDDFT derivative couplings are qualitatively wrong at bond lengths larger than 4.0 bohr, although PBE0-PWA results are much better at shorter bond lengths, which can be understood in terms of its similarity to the wavefunction-based CIS method.

Finally, we note that the TDDFT and TDDFT/TDA derivative couplings are almost identical in this system. This is true not only for the pseudo-wavefunction approach (where the derivative couplings are in reasonable agreement with FCI results) but also for the quadratic response approach (where they are not).

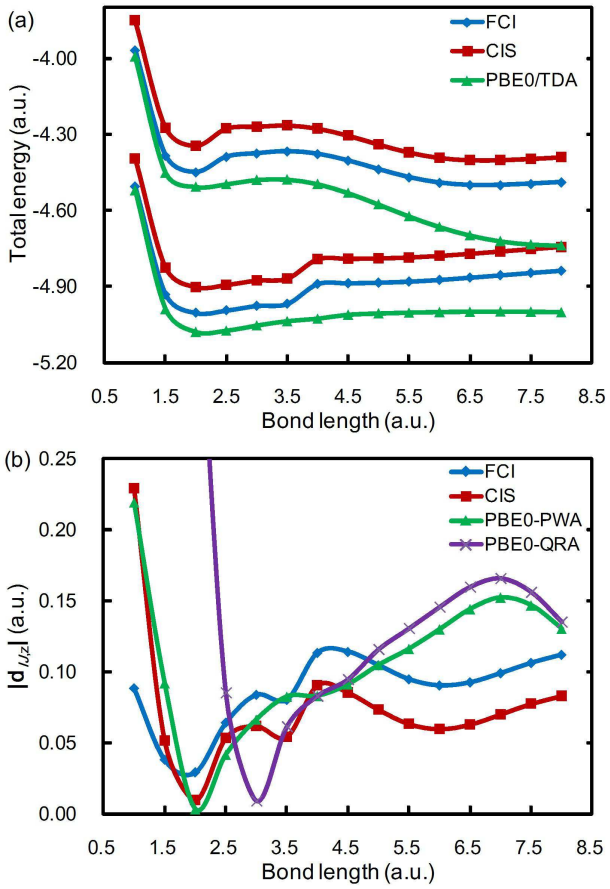

Figure 2.4: (a) Energies of the 3 $^1\Sigma_g^+$ and 5 $^1\Sigma_g^+$ states of He_2 computed at the FCI, CIS, and TDDFT/TDA levels, using the aug-cc-pVDZ basis set and the PBE0 functional for TDDFT. (b) Absolute value of the z-component of the derivative coupling between these two states, computed using the same methods.

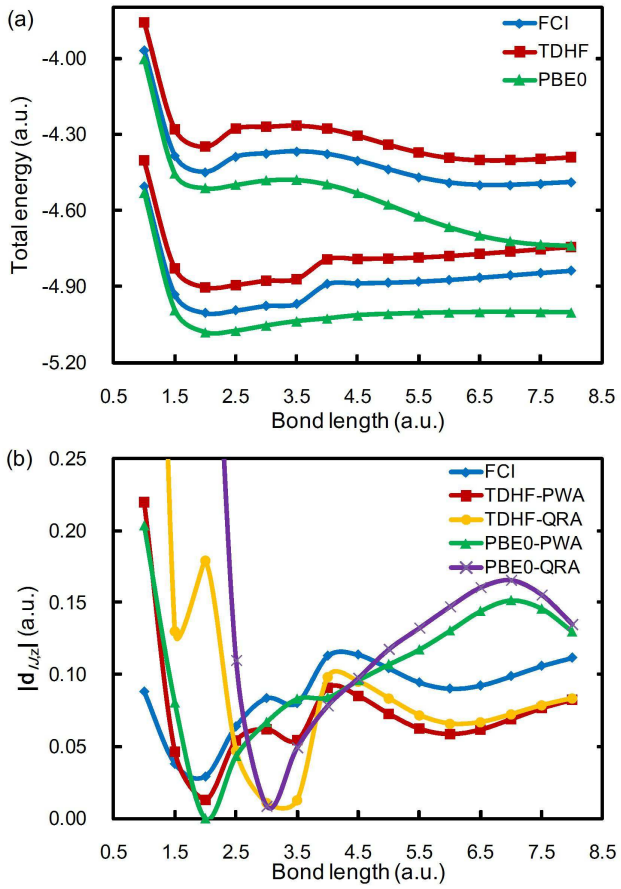

Figure 2.5: (a) Energies of the 3 $^1\Sigma_g^+$ and 5 $^1\Sigma_g^+$ states of He_2 computed at the FCI, TDHF, and TDDFT levels, using the aug-cc-pVDZ basis set and the PBE0 functional for TDDFT. (b) Absolute value of the z-component of the derivative coupling between these two states, computed using the same methods.

Li_2

The 6-31G basis set was used to calculate the derivative couplings between the two lowest $^1\Sigma_u^+$ states of Li_2. These states have single-excitation character, involving $1\sigma_g \rightarrow 1\sigma_u$ and $1\sigma_g \rightarrow 2\sigma_u$ excitation, respectively. The calculated potential curves and derivative couplings are shown in Figs. 2.6 and 2.7. All methods afford similar potential curves for both states, and the derivative couplings obtained using the CIS, TDHF-PWA and PBE0-PWA methods are about the same, but are very different from the FCI derivative couplings.

In contrast, the TDHF-QRA and PBE0-QRA derivative couplings agree very well with the FCI results. We compared the $|\mathbf{X}_{IJ}, \mathbf{Y}_{IJ}\rangle$ matrix from the QRA with the VO and OV blocks of the transition density matrix from FCI, and they are indeed very similar. This may support the previous discussion that the failures of the QRA for H_2 and He_2 are caused by the errors accumulated when calculating the transition density matrices between the TDDFT excited states. Note that the energy gap between the $1!^1\Sigma_u^+$ and $2!^1\Sigma_u^+$ states is less than 3 eV, yet the difference between $\mathbf{d}_{IJ}^{\mathrm{KS}}$ and $\mathbf{d}_{IJ}^{\mathrm{PWA}}$ is quite large. This may indicate the importance of the contributions from $|\mathbf{X}_{IJ}, \mathbf{Y}_{IJ}\rangle$ in some molecules with high symmetry.

H_3

For another high-symmetry example, we calculated the derivative couplings for H_3 in $D_{\infty h}$ symmetry. For HF and DFT calculations, the ground state in $D_{\infty h}$ symmetry belongs to the $^2\Sigma_u^+$ irreducible representation. We compute derivative couplings between the 1 $^2\Sigma_g^+$ and 2 $^2\Sigma_g^+$ states.

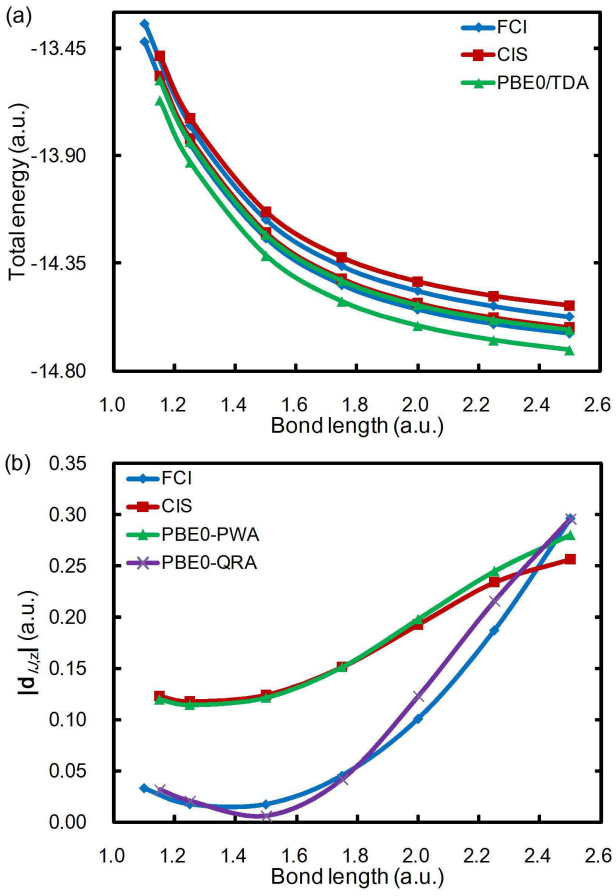

Figure 2.6: (a) Energies of the 1 $^1\Sigma_u^+$ and 2 $^1\Sigma_u^+$ states of Li_2 computed at the FCI, CIS, and TDDFT/TDA levels, using the 6-31G basis set and the PBE0 functional for TDDFT. (b) Absolute value of the z-component of the derivative coupling between these two states, computed using the same methods.

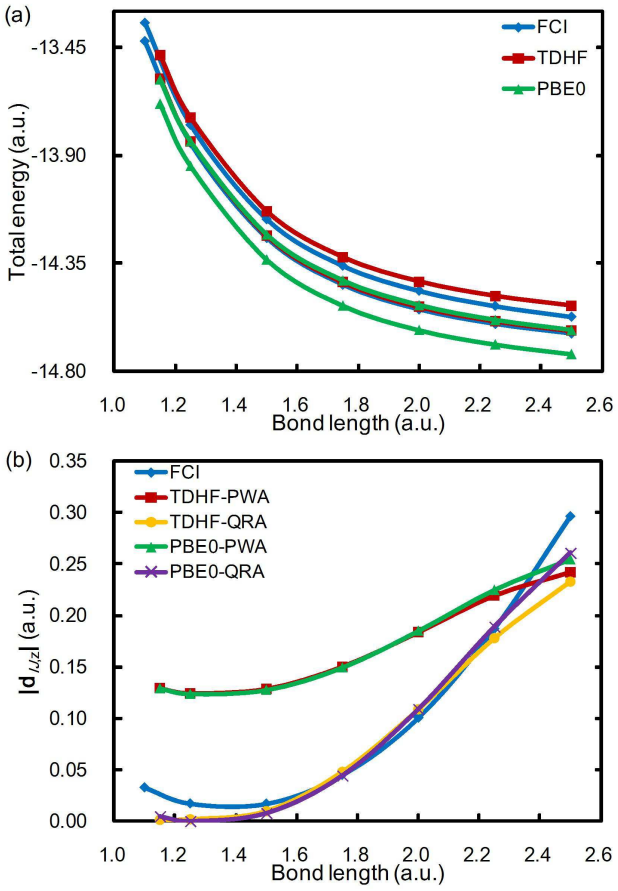

Figure 2.7: (a) Energies of the 1 $^1\Sigma_u^+$ and 2 $^1\Sigma_u^+$ states of Li_2 computed at the FCI, TDHF, and TDDFT levels, using the 6-31G basis set and the PBE0 functional for TDDFT. (b) Absolute value of the z-component of the derivative coupling between these two states, computed using the same methods.

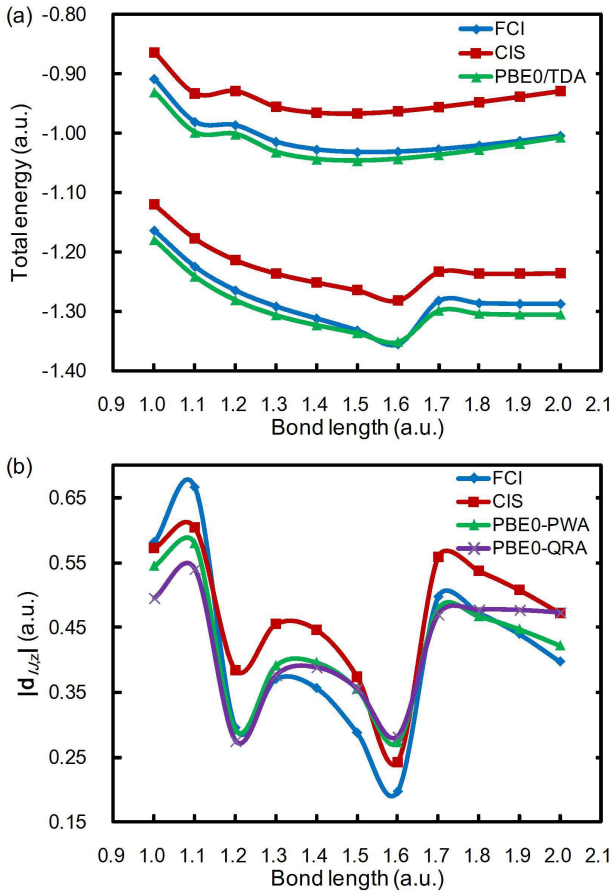

Figure 2.8: (a) Energies of the 1 $^2\Sigma_g^+$ and 2 $^2\Sigma_g^+$ states of H_3 computed at the FCI, CIS, and TDDFT/TDA levels, using the cc-pVDZ basis set and the PBE0 functional for TDDFT. (b) Absolute value of the z-component of the derivative coupling between these two states, computed using the same methods.

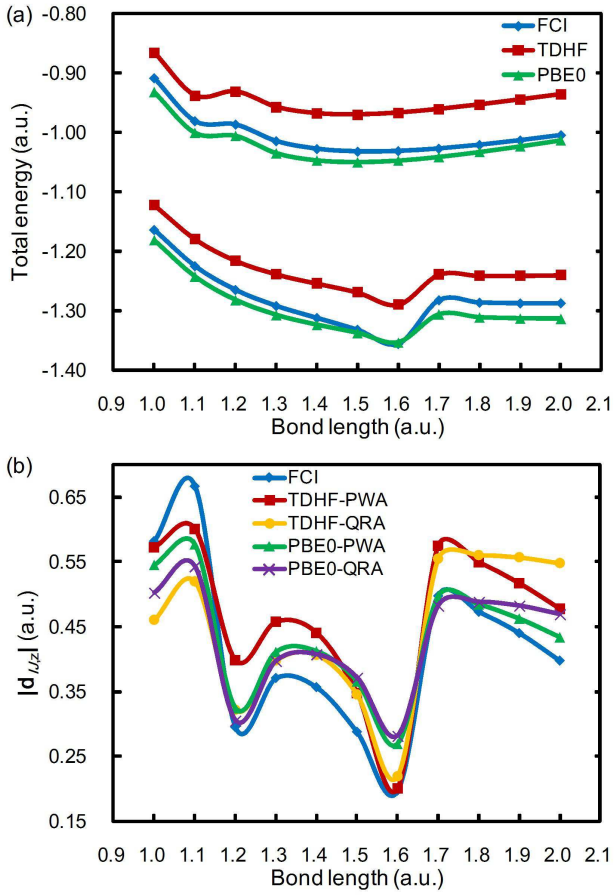

Figure 2.9: (a) Energies of the 1 $^2\Sigma_g^+$ and 2 $^2\Sigma_g^+$ states of H_3 computed at the FCI, TDHF, and TDDFT levels, using the cc-pVDZ basis set and the PBE0 functional for TDDFT. (b) Absolute value of the z-component of the derivative coupling between these two states, computed using the same methods.

In Figs. 2.8 and 2.9, we see that the potential curves obtained from CIS, TDHF, and TDDFT are very similar to the FCI potential curves, for both states. Furthermore, the derivative couplings calculated from CIS, TDHF, and TDDFT are qualitatively correct, and the differences between the QRA and PWA results are quite small. By observing the transition density matrix between FCI states, we found that the OO and VV blocks dominate, whereas the VO and OV blocks are negligible. The same is true for the TDDFT transition density matrix. This explains the similarity between the QRA and PWA derivative couplings. Note that the current H_3 system has high symmetry and the energy gap between the two chosen states is large. Thus, in what situations the VO and OV blocks of the transition density matrix between TDDFT excited states are important is still unclear and needs further study.

Brief summary

By comparing TDDFT derivative couplings computed within the QRA and PWA formalisms to FCI derivative couplings, we reach the following conclusions.

1. The PWA derivative couplings are usually qualitatively correct so long as the potential energy surface is qualitatively correct.

2. There exist systems (such as Li_2 in the present work) where the contributions from $|\mathbf{X}_{IJ}, \mathbf{Y}_{IJ}\rangle$ are important. The PWA may not be adequate for these systems.

3. Failures of the QRA in certain cases may arise due to a poor description of the transition density matrix between the TDDFT excited states. Careful selection

of the exchange-correlation functional may alleviate this problem.

2.4 Conclusion

In the present study, we have presented a compact derivation of TDDFT derivative coupling between excited states that is entirely based on the quadratic response theory; we call this the quadratic response approach or QRA. Our previous formulation[14] of the analytic derivative couplings for spin-flip TDDFT, which was based on a pseudo-wavefunction approach (PWA), is shown to be rigorously correct, as there is no distinction between the QRA and the PWA for *spin-flip* TDDFT. For spin-conserving TDDFT, there *is* a distinction, which we have explored numerically here.

For small-gap systems, we find that the QRA and PWA can usually be used interchangeably, thus the PWA may be a better choice considering its lower computational cost. However, in certain cases (Li_2 in the present work), the VO and OV blocks of the transition density matrix between excited states, which are neglected in the PWA, become important. In these cases, the QRA significantly improves the accuracy of the derivative couplings. Finally, the accuracy of the QRA derivative couplings may be improved if the transition densities calculated in TDDFT are accurate.

Overall, the QRA formalism for TDDFT derivative couplings is a potentially useful approach to calculating these quantities. However, when only qualitatively-correct derivative couplings are required, such as in the optimization of minimum-energy crossing points along conical seams, the PWA will likely be the method of

choice, owing to its lower computational cost.

CHAPTER 3

Analytic Derivative Couplings of SF-TDDFT

In this chapter, we discuss the formulation and implementation of analytic SF-TDDFT derivative couplings. In the last chapter, we have proved that both the quadratic response theory and the pseudo-wavefunction approach lead to the same formulation for SF-TDDFT derivative couplings. Thus, we will first present the derivation of the analytic derivative couplings for spin-flip configuration interaction singles, and the SF-TDDFT derivative couplings can be obtained as a simple extension of that.

3.1 Introduction

Most electronic structure methods are based on the Born-Oppenheimer approximation, in which the motions of electrons and nuclei are separated. The nuclei move on an adiabatic potential energy surface (PES), obtained by solving the electronic Schrödinger equation, and the PES is parametrically dependent on the nuclear coordinates. No electronic transitions can be induced by nuclear motion within the Born-Oppenheimer approximation. Nonadiabatic dynamics methods can be applied to go beyond the Born-Oppenheimer approximation,[6] but in order to compute transition probabilities between electronic states, most of these methods require first-order

derivative couplings

$$\mathbf{d}^{IJ} = \langle \Psi_I | \hat{\boldsymbol{\nabla}} | \Psi_J \rangle = \frac{\mathbf{h}^{IJ}}{E_J - E_I} \tag{3.1}$$

between adiabatic electronic states. The nonadiabatic coupling vector

$$\mathbf{h}^{IJ} = \langle \Psi_I | (\partial \hat{H} / \partial \mathbf{x}) | \Psi_J \rangle \tag{3.2}$$

and the difference gradient vector

$$\mathbf{g}^{IJ} = \hat{\boldsymbol{\nabla}} \big(E_I - E_J \big) \tag{3.3}$$

together define the branching space around a two-state conical intersection.[8]

In principle, $\mathbf{h}^{IJ}$ could be calculated via finite difference, but in the interest of efficiency it is desirable to compute it analytically. This facilitates both nonadiabatic *ab initio* molecular dynamics simulations[42] as well as optimization of minimum-energy crossing points (MECPs) along conical seams.[8] The latter are key features in the study of nonadiabatic phenomena in cases where dynamics simulations are not affordable. Analytic formulations of the derivative couplings h_x^{IJ}, where x represents a nuclear coordinate, have been developed and implemented only for a few *ab initio* methods, primarily multireference configuration interaction (MRCI).[15–18] In small molecules, MRCI has the advantages of a fully-balanced treatment of ground and excited states as well as including a large fraction of electron correlation, but its computational cost limits its application to molecules with < 20 atoms. Analytic derivative couplings for equation-of-motion coupled-cluster (EOM-CC) theory have been introduced more recently,[19,20] but EOM-CC methods are also limited to small molecules.

As computationally inexpensive alternatives, analytic derivative couplings for single-reference methods including configuration interaction singles (CIS) and time-dependent density functional theory (TDDFT) have been developed recently.[21,23–25] Unfortunately, these methods suffer from an imbalance in the treatment of ground- versus excited-state electron correlation, which makes them suitable only for describing electronic transitions between excited states. This is especially true near the important "funnel" regions along conical seams.[10] For any conical intersection involving the reference state (which is usually the ground state) in CIS or TDDFT, it is readily shown that the branching space is one-dimensional rather than two-dimensional.[10] The same is true, for the same reason, in the case of EOM-CC methods.[43]

The simplest extensions of CIS and TDDFT that correct these problems are spin-flip (SF) methods: SF-CIS[44] and SF-TDDFT, the latter in its "collinear" formulation.[11] Both of these two methods use a high-spin reference state and compute excitations that include a SF transition, so that for example a singlet ground state can be obtained from a self-consistent field (SCF) calculation of an $S_z = 1$ state. Recent computational studies have shown good performance of collinear SF-TDDFT in describing the electronic structure in both Franck-Condon regions and in crossing seam regions.[45–49]

In the present work, we show the existing formalism for CIS analytic derivative couplings[21] can be extended to SF-CIS and (collinear) SF-TDDFT. The resulting equations amount to relatively minor modifications of the CIS or TDDFT analytic

gradient formalism, hence computer implementation is straightforward, and the additional cost is modest. Although the extension from CIS to TDDFT is *ad hoc*, numerical examples presented herein demonstrate the accuracy and efficiency of this approach.

3.2 Theory

The following notation is used throughout this work. Occupied and virtual molecular spin orbitals are labeled $i, j, k, l, \ldots$ and $a, b, c, d, \ldots$, respectively, whereas $p, q, r, s, \ldots$ index arbitrary (occupied or virtual) molecular spin orbitals. Greek letters $\mu, \nu, \lambda, \sigma, \ldots$ index atomic orbitals. The symbol x represents a nuclear coordinate and derivatives with respect to x will be indicated as, *e.g.*, $\hat{H}^{[x]} = \partial\hat{H}/\partial x$ and $|\Psi_I^{[x]}\rangle = |\partial\Psi_I/\partial x\rangle$. (We use "$[x]$" to indicate the full derivative with respect to coordinate x, which includes differentiation of the molecular orbitals, rather than a "skeleton derivative",[50] which does not.) Two-electron integrals are written in physicists' notation.

3.2.1 Analytic derivative couplings for SF-CIS

Formalism

In this section, we revisit the analytic formulation of derivative couplings for CIS[21] and extend it to SF-CIS. (A Lagrangian formulation of the CIS derivative couplings has appeared recently,[26] but we follow the direct differentiation approach of Ref. 21.) The CIS wave function for excited state I is described as a linear combination of

singly-excited Slater determinants:

$$|\Psi_I\rangle = \sum_{ai} t_{ai}^I |\Phi_i^a\rangle \ . \tag{3.4}$$

For SF-CIS, the Slater determinant $|\Phi_i^a\rangle$ is formed by single $\alpha \rightarrow \beta$ SF excitations from a high-spin Hartree-Fock reference state (*e.g.* $S_z = 1$ or $S_z = 3/2$) to a low spin target state (*e.g.* $S_z = 0$ or $S_z = 1/2$).[44] Since spin-conserving CIS calculations use an *ansatz* identical to Eq. (3.4) but with spin-conserving Slater determinants, we will use the notation $|\Phi_i^a\rangle$ to mean either a spin-conserving or a spin-flipping determinant, depending on whether we wish to consider CIS or SF-CIS. The formalism derived below is valid for both.

The Hellmann-Feynman expression for the derivative coupling is

$$\left\langle \Psi_I \middle| \Psi_J^{[x]} \right\rangle = \frac{\langle \Psi_I | \hat{H}^{[x]} | \Psi_J \rangle}{E_J - E_I} \ . \tag{3.5}$$

However, this equation holds only when $|\Psi_I\rangle$ and $|\Psi_J\rangle$ are eigenfunctions of $\hat{H}$. As suggested in Ref. 21, we can use a projection operator

$$\hat{\mathcal{P}} = \sum_{ia} \left|\Phi_i^a\right\rangle\left\langle\Phi_i^a\right| \tag{3.6}$$

to project the electronic Hamiltonian $\hat{\mathcal{H}}$ onto the single-excitation subspace. Upon subtracting out the Hartree-Fock reference state energy, E_0, the projected Hamiltonian is defined as

$$\hat{\mathcal{H}} = \hat{\mathcal{P}}(\hat{H} - E_0)\hat{\mathcal{P}} \ . \tag{3.7}$$

The CIS wave function in Eq. (3.4) is an eigenfunction of the model Hamiltonian $\hat{\mathcal{H}}$, with an eigenvalue equal to the CIS excitation energy, ω_I. Thus the derivative

coupling between CIS excited states $|\Psi_I\rangle$ and $|\Psi_J\rangle$ is

$$\big\langle \Psi_I \big| \Psi_J^{[x]} \big\rangle = \frac{\langle \Psi_I | \hat{\mathcal{H}}^{[x]} | \Psi_J \rangle}{\omega_J - \omega_I} \; . \tag{3.8}$$

To derive working equations from Eq. (3.8), we need the derivative of $\hat{\mathcal{H}}$. Using the definition of $\hat{\mathcal{P}}$ we obtain

$$\begin{aligned} \hat{\mathcal{H}}^{[x]} &= \sum_{ijab} \Big[\big| \Phi_i^a \big\rangle \big\langle \Phi_i^a \big| (\hat{H} - E_0) \big| \Phi_j^b \big\rangle \big\langle \Phi_j^b \big| \Big]^{[x]} \\ &= \sum_{ijab} \Big(A_{ai,bj} \big| \Phi_i^{a[x]} \big\rangle \big\langle \Phi_j^b \big| + A_{ai,bj}^{[x]} \big| \Phi_i^a \big\rangle \big\langle \Phi_j^b \big| + A_{ai,bj} \big| \Phi_i^a \big\rangle \big\langle \Phi_j^{b[x]} \big| \Big) \end{aligned} \tag{3.9}$$

where

$$A_{ai,bj} = \big\langle \Phi_i^a \big| (\hat{H} - E_0) \big| \Phi_j^b \big\rangle \tag{3.10}$$

is the matrix element in conventional CIS theory.[51] Substituting Eq. (3.9) into Eq. (3.8), and using Eq. (3.4) along with the orthonormality of Slater determinants, we obtain

$$\begin{aligned} (\omega_J - \omega_I) \big\langle \Psi_I \big| \Psi_J^{[x]} \big\rangle &= \sum_{ijab} \big\langle \Psi_I \big| \Phi_i^{a[x]} \big\rangle A_{ai,bj} \big\langle \Phi_j^b \big| \Psi_J \big\rangle + \sum_{ijab} \big\langle \Psi_I \big| \Phi_i^a \big\rangle A_{ai,bj}^{[x]} \big\langle \Phi_j^b \big| \Psi_J \big\rangle \\ &\quad + \sum_{ijab} \big\langle \Psi_I \big| \Phi_i^a \big\rangle A_{ai,bj} \big\langle \Phi_j^{b[x]} \big| \Psi_J \big\rangle \\ &= \sum_{ijab} \big\langle \Psi_I \big| \Phi_i^{a[x]} \big\rangle A_{ai,bj} t_{bj}^J + \sum_{ijab} t_{ai}^I A_{ai,bj}^{[x]} t_{bj}^J \\ &\quad + \sum_{ijab} t_{ai}^I A_{ai,bj} \big\langle \Phi_j^{b[x]} \big| \Psi_J \big\rangle \; . \end{aligned} \tag{3.11}$$

Using the nuclear derivative of the molecular spin-orbitals' creation and annihilation operators,[21] we next obtain

$$\big\langle \Psi_I \big| \Phi_i^{a[x]} \big\rangle = \sum_c^{\text{particles}} t_{ci}^I \big\langle c \big| a^{[x]} \big\rangle + \sum_k^{\text{holes}} t_{ak}^I \big\langle k \big| i^{[x]} \big\rangle \tag{3.12}$$

and

$$\big\langle \Phi_j^{b[x]} \big| \Psi_J \big\rangle = \sum_c^{\text{particles}} t_{cj}^J \big\langle c \big| b^{[x]} \big\rangle + \sum_k^{\text{holes}} t_{bk}^J \big\langle k \big| j^{[x]} \big\rangle \; . \tag{3.13}$$

Next, recall that the CIS equations for states I and J are

$$\begin{aligned} \sum_{ia} t_{ai}^{I} A_{ai,bj} &= \omega_I t_{bj}^{I} \\ \sum_{jb} A_{ai,bj} t_{bj}^{J} &= \omega_J t_{ai}^{J} \ . \end{aligned} \tag{3.14}$$

Combining Eq. (3.14) with the results above, we obtain a general expression for the derivative coupling that is valid for both spin-conserved and spin-flip CIS:

$$\begin{aligned} (\omega_J - \omega_I)\big\langle \Psi_I \big| \Psi_J^{[x]} \big\rangle = &\sum_{ac} \sum_{i} \left(t_{ci}^{I} t_{ai}^{J} \omega_J + t_{ci}^{J} t_{ai}^{I} \omega_I \right) \big\langle c \big| a^{[x]} \big\rangle \\ &+ \sum_{ik} \sum_{a} \left(t_{ak}^{I} t_{ai}^{J} \omega_J + t_{ak}^{J} t_{ai}^{I} \omega_I \right) \big\langle k \big| i^{[x]} \big\rangle \\ &+ \sum_{ijab} t_{ai}^{I} A_{ai,bj}^{[x]} t_{bj}^{J} \ . \end{aligned} \tag{3.15}$$

Overlap integrals between virtual orbitals and their displaced counterparts are given by

$$\big\langle c \big| a^{[x]} \big\rangle = \sum_{\mu\nu} C_{\mu c} \big\langle \mu \big| \nu^{[x]} \big\rangle C_{\nu a} + \sum_{\mu\nu} C_{\mu c} \langle \mu | \nu \rangle C_{\nu a}^{[x]} \tag{3.16}$$

The derivatives $C_{\nu a}^{[x]}$ of the molecular orbital (MO) coefficients can be expanded in the unperturbed MO basis,[52]

$$C_{\nu a}^{[x]} = \sum_{p}^{\text{all}} C_{\nu p} U_{pa}^{[x]} \ . \tag{3.17}$$

The virtual–virtual coefficients $U_{ba}^{[x]}$ are redundant, and can be expressed as[50]

$$U_{ba}^{[x]} = -\tfrac{1}{2} S_{ba}^{[\overline{x}]} \tag{3.18}$$

where

$$S_{ba}^{[\overline{x}]} = \sum_{\mu\nu} C_{\mu b} S_{\mu\nu}^{[x]} C_{\nu a} \tag{3.19}$$

is a so-called skeleton derivative[50] of an MO overlap integral, meaning that it is evaluated for fixed MO coefficients. In contrast, the quantity $S^{[x]}_{\mu\nu} = \partial\langle\mu|\nu\rangle/\partial x$ is simply an overlap derivative in the atomic orbital (AO) basis. Equation (3.19) follows from the fact that $\mathbf{U}^{[x]} + (\mathbf{U}^{[x]})^\dagger = -\mathbf{S}$.[50]

Putting all of this together, we have

$$C^{[x]}_{\nu a} = \sum_i^{\text{occ}} C_{\nu i} U^{[x]}_{ia} - \tfrac{1}{2} \sum_b^{\text{virt}} C_{\nu b} S^{[\overline{x}]}_{ba} \ . \tag{3.20}$$

However, the term involving $U^{[x]}_{ia}$ vanishes when this equation is inserted into Eq. (3.16), because $\langle c|i\rangle = 0$, and thus $\langle c|a^{[x]}\rangle$ can be evaluated without the need to solve coupled-perturbed equations. Instead, we obtain

$$\big\langle c\big|a^{[x]}\big\rangle = \sum_{\mu\nu} C_{\mu c}\big\langle\mu\big|\nu^{[x]}\big\rangle C_{\nu a} - \tfrac{1}{2} \sum_{\mu\nu} \sum_d^{\text{virt}} C_{\mu c}\langle\mu|\nu\rangle C_{\nu d} S^{[\overline{x}]}_{da} \ . \tag{3.21}$$

A similar expression can be derived for the terms $\langle k|i^{[x]}\rangle$ that appear in Eq. (3.15):

$$\big\langle k\big|i^{[x]}\big\rangle = \sum_{\mu\nu} C_{\mu k}\big\langle\mu\big|\nu^{[x]}\big\rangle C_{\nu i} - \tfrac{1}{2} \sum_{\mu\nu} \sum_j^{\text{occ}} C_{\mu k}\langle\mu|\nu\rangle C_{\nu j} S^{[\overline{x}]}_{ji} \ . \tag{3.22}$$

Discussion

Equation (3.15) is a compact expression for the CIS derivative couplings. The non-Hellman–Feynman (or "response") terms in this expression are easily evaluated using Eqs. (3.21) and (3.22), while the Hellman-Feynman term is analogous to the conventional CIS energy gradient expression,[53]

$$\omega^{[x]}_I = \sum_{ijab} t^I_{ai} A^{[x]}_{ai,bj} t^I_{bj} \ , \tag{3.23}$$

but with different excitation eigenvectors on the right and left in Eq. (3.15). As such, we can calculate CIS analytic derivative couplings using the same algorithm for as for CIS analytic energy gradients,[53,54] and very little extra coding is required. Actually, our Eq. (3.15) for the derivative couplings is equivalent to Eq. (A23) in Ref. 21, although our derivation is somewhat more compact. Our algorithm is also analogous to that used to compute analytic derivative couplings for MRCI wave functions,[15–18] where the Hellman-Feynman term is sometimes called the "CI contribution" and the non-Hellman–Feynman terms are the "configuration state function (CSF) contribution".[18]

The explicit form of $A^{[x]}_{ai,bj}$ is derived in the Appendix. Note also that the wave function *ansatz* in Eq. (3.4) is invariant to unitary transformations of the occupied orbitals and, separately, to unitary transformations of the virtual orbitals, hence Eq. (3.15) for the derivative couplings is also invariant to such transformations.

A long-known problem with derivative couplings, but one that is sometimes overlooked, is their lack of translational invariance.[15,55–58] In a nonadiabatic dynamics simulation, this allows constant-velocity motion of the entire system to stimulate transitions between adiabatic electronic states, behavior that is ultimately an artifact of using real-valued Born-Oppenheimer electronic states for the coupled electron–nuclear dynamics.[21,55] Motivated by earlier literature on atom–atom scattering calculations,[55] Fatehi *et al.*[21,58] recently introduced electron translation factors (ETFs) for analytic derivative couplings computed using atom-centered basis sets. These authors suggest that the magnitude of the ETFs may be significant for high-symmetry

molecules.[58]

ETFs are intended to restore translational invariance in the the nonadiabatic nuclear dynamics. This can be realized by introducing complex phase factors into the AO basis functions,[21] which allow the electrons to propagate alongside the nuclei and which render the nonadiabatic equations of motion rigorously translationally invariant. To achieve this, the CIS derivative coupling that appears in the equations of motion is replaced by an ETF-corrected derivative coupling of the form[21]

$$\left\langle \Psi_I \middle| \Psi_J^{[x]} \right\rangle_{\text{ETF}} = \left\langle \Psi_I \middle| \Psi_J^{[x]} \right\rangle + \sum_{\mu\nu} \widetilde{S}_{\mu\nu}^{[x]} \left(\sum_{iab} C_{\nu a} t_{ai}^I t_{bi}^J C_{\mu b} + \sum_{ija} C_{\nu i} t_{ai}^I t_{aj}^J C_{\mu j} \right) \tag{3.24}$$

where

$$\widetilde{S}_{\mu\nu}^{[x]} = \tfrac{1}{2} \left(\left\langle \mu \middle| \nu^{[x]} \right\rangle - \left\langle \nu \middle| \mu^{[x]} \right\rangle \right) \ . \tag{3.25}$$

What is not mentioned in Ref. 21 is the fact that the first two terms in Eq. (3.15) can be rewritten as

$$\begin{aligned} &\sum_{ac} \sum_{i} \left(t_{ci}^I t_{ai}^J \omega_J + t_{ci}^J t_{ai}^I \omega_I \right) \langle c | a^{[x]} \rangle + \sum_{ik} \sum_{a} \left(t_{ak}^I t_{ai}^J \omega_J + t_{ak}^J t_{ai}^I \omega_I \right) \langle k | i^{[x]} \rangle \\ &= (\omega_I - \omega_J) \sum_{\mu\nu} \widetilde{S}_{\mu\nu}^{[x]} \left(\sum_{iab} C_{\nu a} t_{ai}^I t_{bi}^J C_{\mu b} + \sum_{ija} C_{\nu i} t_{ai}^I t_{aj}^J C_{\mu j} \right) . \end{aligned} \tag{3.26}$$

Thus, the ETF-corrected derivative coupling in Eq. (3.24) is actually identical to the final term in Eq. (3.15):

$$\left\langle \Psi_I \middle| \Psi_J^{[x]} \right\rangle_{\text{ETF}} = \frac{1}{\omega_J - \omega_I} \sum_{ijab} t_{ai}^I A_{ai,bj}^{[x]} t_{bj}^J \ . \tag{3.27}$$

In other words, the ETF correction precisely cancels the non-Hellman–Feynman terms in the expression for the derivative coupling!

Within CIS theory, the elements h_x^{IJ} of the nonadiabatic coupling vector [Eq. (3.2)] are

$$h_x^{IJ} = \sum_{ijab} t_{ai}^I A_{ai,bj}^{[x]} t_{bj}^J = (\omega_J - \omega_I) \big\langle \Psi_I \big| \Psi_J^{[x]} \big\rangle_{\text{ETF}} \,. \tag{3.28}$$

Thus, we find that the ETF-corrected derivative couplings in CIS theory may actually be more useful than the full derivative couplings formulated in Eq. (3.15). This observation may have implications in the context of derivative couplings for non-variational, correlated wave function methods such as EOM-CC.[20]

3.2.2 Analytic derivative couplings for SF-TDDFT

SF-TDDFT (with a collinear spin density) was originally introduced by Shao *et al.*[11] Unlike the conventional linear-response TDDFT, and also unlike SF-TDDFT with a non-collinear spin density,[12] collinear SF-TDDFT resembles a modified SF-CIS *ansatz* wherein Kohn-Sham MOs and the Kohn-Sham effective Hamiltonian are used in place of their Hartree-Fock counterparts. We therefore propose an *ad hoc* modification to the CIS formalism, in which matrix elements $\langle \Phi_i^a \big| \hat{H} \big| \Phi_j^b \rangle$ are replaced by their TDDFT counterparts. The latter are given by

$$\begin{aligned} \big\langle \Phi_i^a \big| \hat{H}_{\text{KS}} \big| \Phi_j^b \big\rangle &= E_{\text{KS}} \delta_{ij} \delta_{ab} + f_{ab} \delta_{ij} - f_{ij} \delta_{ab} \\ &\quad + \langle aj | ib \rangle - C_{\text{HF}} \langle aj | bi \rangle + \langle aj | \hat{\xi}_{\text{xc}} | ib \rangle \,, \end{aligned} \tag{3.29}$$

where E_{KS} is the Kohn-Sham SCF energy, $\hat{f}$ is the Kohn-Sham Fock operator, C_{HF} is the fraction of Hartree-Fock exchange in the exchange-correlation functional, and

$$\big\langle aj \big| \hat{\xi}_{\text{xc}} \big| ib \big\rangle = \int d\mathbf{r} d\mathbf{r}' \; \phi_a(\mathbf{r}) \phi_i(\mathbf{r}) \frac{\delta^2 f_{\text{xc}}}{\delta \rho(\mathbf{r}) \delta \rho(\mathbf{r}')} \phi_b(\mathbf{r}') \phi_j(\mathbf{r}') \tag{3.30}$$

is a matrix element of the exchange-correlation kernel. Effectively, we are "grafting on" an exchange-correlation term to SF-CIS, which at some level amounts to taking seriously the Kohn-Sham determinant as a wave function and will need to be validated with benchmark studies. Ou *et al.*[28] recently introduced derivative couplings for spin-conserving TDDFT within the spin-conserving, Tamm-Dancoff approximation (TDA),[35] based on the same *ad hoc* modification applied to a version of Eq. (3.15). There is some evidence that the TDA may be better suited for exploration of potential energy surfaces, as compared to full TDDFT, owing to triplet instabilities in the latter method.[59]

From Eq. (3.29), it is clear that Eqs. (3.15), (3.27) and (3.28) are valid for collinear SF-TDDFT except that the matrix elements $A^{[x]}_{ai,bj}$ must be modified according to the SF-TDDFT analytic energy gradient.[11] Details are shown in the Appendix. Notably, full TDDFT derivative couplings based on quadratic response theory have recently been derived (though not implemented),[26] and this formalism involves an extra term relative to our Eq. (3.15). The significance of this term remains to be explored.

3.3 Numerical examples

Both Eq. (3.15) for $\left\langle \Psi_I \middle| \Psi^{[x]}_J \right\rangle$, as well as Eq. (3.27) for the ETF-corrected derivative coupling, have been implemented in a locally modified version of the Q-Chem program,[33] for both spin-conserved CIS, spin-flip CIS, and collinear SF-TDDFT. For the spin-conserving cases, both spin-restricted and unrestricted reference states have been implemented, through a restricted open-shell reference is not yet implemented.

Finite-difference results are in excellent agreement with the analytic implementations of all three methods (see Appendix B), which is compelling evidence of the validity of our implementation. In addition, the derivative couplings computed using Eqs. (3.15) and (3.27) are exactly the same as the corresponding couplings computed using the formalism introduced in Ref. 21 for spin-conserved CIS, which was implemented in Q-Chem by the authors of Ref. 21. This agreement is not surprising, since the two approaches are formally equivalent for spin-conserved CIS, but provides additional evidence in support of the correctness of our implementation. Illustrative numerical examples of the new SF-CIS and SF-TDDFT derivative couplings are presented below.

3.3.1 H_3 potential surfaces near a conical intersection

Levine *et al.*[10] have shown that spin-conserved CIS and TDDFT cannot provide correct topology of the PES in the vicinity of a conical intersection that involves the reference state (usually the ground state), and numerical examples have been presented.[10,60] This is mainly due to the single-excitation nature of spin-conserved CIS and TDDFT as well as the unbalanced treatment of ground and excited states. For CIS calculations, the combination of this imbalance along with Brillouin's theorem means that the CIS method fails to provide a correct description of degenerate ground states.

SF-CIS and SF-TDDFT, on the other hand, can provide correct PESs near conical intersections, because these methods contain some determinants that look like double excitations relative to the ground state. Thus, the ground state is treated on a

more balanced footing with respect to the excited states. In other words, conical intersections with double-excitation character (*e.g.* twisted-pyramidalized ethylene[45]) can be described by SF-CIS and SF-TDDFT, and there is furthermore no fundamental problem in describing a degenerate ground state.

Our first test system is H_3 in D_{3h} symmetry, which requires the D_0 and D_1 states to be degenerate, and we will compare SF-CIS and collinear SF-TDDFT results to restricted open-shell CIS (ROCIS) and spin-conserving TDA-TDDFT. In this particular case, spin-conserving, unrestricted CIS fails to describe this system due to significant spin contamination, necessitating the use of a restricted open-shell reference state. Furthermore, spin-conserving TDDFT fails in the presence of the near-degeneracy, owing to imaginary roots (triplet instabilities) in the orbital Hessian. For this reason, the spin-conserving TDDFT calculations were performed within the TDA. The latter calculations employ the B3LYP functional while SF-TDDFT calculations employ the BH&HLYP functional (50% Hartree-Fock exchange plus 50% Becke exchange[61] with Lee-Yang-Parr correlation[41]), and we abbreviate this method as SF-BH&HLYP.

We scanned over the bond length of all D_{3h} geometries for H_3, using the 6-31G* basis set for all energy scans, finding minimum-energy conical intersections at $R =$ 1.35 Å (SF-CIS), $R = 1.19$ Å (SF-BH&HLYP), $R = 1.09$ Å (ROCIS), and $R = 1.09$ Å (TD-B3LYP). In Fig. 3.1, two internal coordinates (one angle and one bond length, as shown in the figure) are varied to depict the PES in the vicinity of the D_{3h} conical intersection.

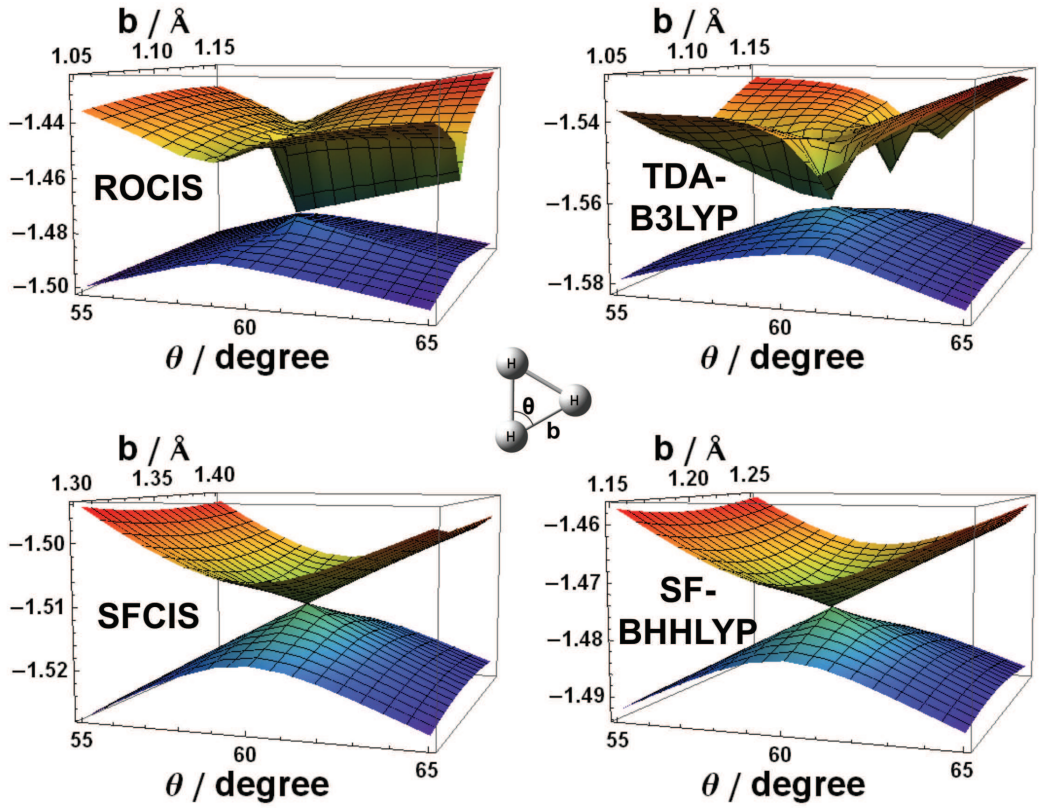

Figure 3.1: Potential energy surfaces around the conical intersections of D_{3h} H_3 calculated by restricted open-shell CIS, unrestricted TD-B3LYP within the Tamm-Dancoff approximation, SF-CIS, and SF-BH&HLYP. All calculations employ the 6-31G* basis set, and energies are shown in atomic units.

The degeneracy between the D_0 and D_1 states does not appear for most equilateral triangular geometries in ROCIS calculations because the D_0 and D_1 states are calculated within different schemes (*i.e.* Hartree-Fock SCF versus configuration interaction). Moreover, the D_1 surface shows an unphysical sharp cusp near the intersection. This has been observed spin-conserving TDDFT calculations as well,[10] and is confirmed by the TD-B3LYP results in Fig. 3.1, wherein D_1 exhibits multiple, unphysical cusps. SF-CIS and SF-BH&HLYP calculations, on the other hand, clearly provide the correct double-cone shape, and the surface varies smoothly away from the intersection.

Although this particular symmetry-required degeneracy between doublet states is correctly reproduced by SF-CIS and SF-TDDFT, not all possible single and double excitations are contained in the SF set of excitations, and as such there certainly exist systems where a degenerate ground state is not correctly reproduced by these methods. For example, SF-CIS and SF-BH&HLYP fail to produce the symmetry-required degeneracy in linear H–O–H ($D_{\infty h}$ symmetry). Degenerate ground states in closed-shell systems may generally be a problem for such methods, as significant spin contamination may lead to a lifting of what should properly be a symmetry-imposed degeneracy.

3.3.2 Minimum-energy crossing points for ethylene

In contrast to the symmetry-imposed degeneracy in H_3, we next consider some accidental degeneracies in ethylene. We have used SF-CIS and SF-TDDFT to locate four critical points (see Fig. 3.2) on the S_0/S_1 crossing seam, for which we can compare

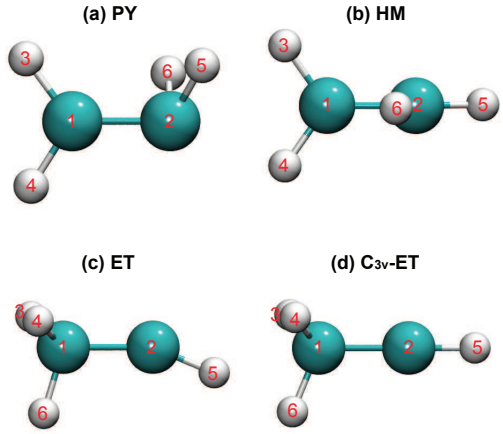

Figure 3.2: Geometries for the MECPs of ethylene: (a) twisted-pyramidalized (**PY**), (b) hydrogen-migration (**HM**), (c) ethylidene (**ET**) and (d) C_{3v} ethylidene (**C3v–ET**).

our results to a previous MRCI study.[4] Three of these critical points are MECPs, whereas structure **HM** in Fig. 3.2 is actually a saddle point on the crossing seam.[4] Critical points were optimized using the projected-gradient algorithm of Bearpark *et al.*,[13] which involves optimizing along the gradient

$$\mathbf{g} = 2(E_J - E_I)\mathbf{x} + \mathbf{P}\mathbf{g}_{\text{mean}} \ . \tag{3.31}$$

The quantity

$$\mathbf{g}_{\text{mean}} = \tfrac{1}{2}\hat{\boldsymbol{\nabla}}\big(E_I + E_J\big) \tag{3.32}$$

is the average energy gradient for states I and J,

$$\mathbf{x} = \frac{\hat{\boldsymbol{\nabla}}(E_J - E_I)}{\big|\big|\hat{\boldsymbol{\nabla}}(E_J - E_I)\big|\big|} \tag{3.33}$$

Table 3.1: Geometric parameters for the four ethylene critical points depicted in Fig. 3.2, optimized by SF-CIS/6-31G(d,p), SF-BH&HLYP/6-31G(d,p) and MR-CISD/aug′-cc-pTVZ levels. (MRCI values are taken from Ref. 4.)

Parameter	**PY**			**HM**			**ET**			**C3v–ET**		
	spin-flip		MRCI	spin-flip		MRCI	spin-flip		MRCI	spin-flip		MRCI
	CIS	BH&HLYP		CIS	BH&HLYP		CIS	BH&HLYP		CIS	BH&HLYP	
C_1–C_2	1.415	1.384	1.399	1.363	1.338	1.360	1.452	1.434	1.448	1.456	1.437	1.452
C_2–H_5	1.082	1.098	1.096	1.054	1.056	1.063	1.056	1.060	1.068	1.050	1.056	1.064
C_2–H_6	1.209	1.140	1.163	1.231	1.162	1.180						
C_1–H_3	1.089	1.098	1.098	1.092	1.108	1.105	1.090	1.094	1.096	1.090	1.095	1.097
$\angle C_1C_2H_5$	123.6	113.4	118.6	168.9	162.1	164.1	156.3	157.3	155.1			
$\angle C_1C_2H_6$	66.9	89.7	82.8	62.7	75.5	72.8						
$\angle H_5C_2H_6$	98.3	92.2	94.4	128.4	122.5	121.9						
$\angle H_3C_1C_2H_5$	23.1	39.3	35.2	−88.1	−93.7	−76.3						
$\angle H_4C_1C_2H_6$	108.0	120.0	114.7	−89.7	−85.5	−88.1						

is the normalized gradient difference vector, and

$$\mathbf{P} = \mathbf{1} - \mathbf{x}\mathbf{x}^\dagger - \mathbf{y}\mathbf{y}^\dagger \tag{3.34}$$

projects out the vector $\mathbf{x}$ and also the vector

$$\mathbf{y} = \frac{(\mathbf{1} - \mathbf{x}\mathbf{x}^\dagger)\mathbf{h}^{IJ}}{\left|\left|(\mathbf{1} - \mathbf{x}\mathbf{x}^\dagger)\mathbf{h}^{IJ}\right|\right|} \tag{3.35}$$

from the mean gradient.

Some selected internal coordinates were compared with the MRCI results in Table 3.3.2. The SF-BH&HLYP and MRCI geometries are in good agreement, and the SF-CIS geometries agree qualitatively with the MRCI results, except that for the **PY** and **HM** structures optimized by SF-CIS, the extent of hydrogen migration is slightly overestimated as compared with the SF-BH&HLYP and MRCI results.

The relative energies of the four critical points are shown in Table 3.2. SF-BH&HLYP energies agree well with the MRCI results in all four cases. However,

Table 3.2: Relative energies (in eV) for the four critical points of ethylene that are depicted in Fig. 3.2, as calculated at the SF-CIS/6-31G(d,p), SF-BH&HLYP/ 6-31G(d,p), and MR-CISD/aug′-cc-pVTZ levels. (MRCI values are taken from Ref. 4.)

	SF-CIS		SF-BH&HLYP		MRCI	
MECP	S_0	S_1	S_0	S_1	S_0	S_1
$\mathbf{S}_{0min}$	0.00	9.07	0.00	8.35	0.00	8.02
PY	5.88	5.88	4.85	4.85	4.83	4.83
HM	6.51	6.51	5.49	5.49	5.38	5.38
ET	4.71	4.71	4.62	4.62	4.49	4.49
C_{3v}–ET	4.86	4.86	4.70	4.70	4.59	4.60

Table 3.3: Efficiencies of two different algorithms for locating ethylene MECPs, at the SF-BH&HLYP/6-31G** level. The same convergence criteria and starting structures were used for both algorithms.

MECP	Using $\mathbf{g}$ only[a]		Using $\mathbf{g}$ and $\mathbf{h}$[b]	
	iterations	time/s	iterations	time/s
PY	49	1126	21	566
ET	20	429	8	201

[a]Branching-plane updating method of Ref. 62.

[b]Projected-gradient method of Ref. 13.

SF-CIS energies differ by more than 1 eV (as compared to the MRCI energies) for $\mathbf{S}_{0min}$, **PY** and **HM**. This likely reflects the lack of dynamical correlation in SF-CIS.

Finally, we compare the efficiency of the aforementioned projected-gradient optimization algorithm,[13] which uses both $\mathbf{g}^{IJ}$ and $\mathbf{h}^{IJ}$, to that of a branching-plane updating algorithm[62] that requires only $\mathbf{g}^{IJ}$. (We find the latter algorithm to be much more efficient as compared to penalty-constrained approaches[63] that also do

not require derivative couplings.) Performance data for ethylene MECPs are shown in Table 3.3, from which we see that the branching-plane updating algorithm requires more than twice as many iterations to converge as compared to the projected-gradient algorithm. Calculation of $\mathbf{h}^{IJ}$ adds only a very small cost per iteration, hence the projected-gradient algorithm based on analytic derivative couplings affords significantly faster timings.

3.4 Summary

We have formulated and implemented analytic first derivative couplings for SF-CIS, which are simple extensions of previous work on derivative couplings for spin-conserved CIS but have the advantage that the SF methods describe ground and excited states in a more balanced way. *Ad hoc* introduction of an exchange-correlation term in the Hamiltonian then affords derivative couplings for (collinear) SF-TDDFT. Numerical examples demonstrate that these SF methods provide correct topologies in the vicinity of conical intersections and reasonable energetics across the PES, as we saw in a previous study as well.[49] As such, these methods seem like good choices for nonadiabatic *ab initio* molecular dynamics simulations, especially in the case of SF-TDDFT, which incorporates dynamical electron correlation. (Static correlation is handled via the SF formalism.)

Although spin contamination becomes problematic for some systems,[49] these SF methods can in principle be extended to their spin-complete counterparts.[3,64,65] The SF-extended CIS method,[64] for example, is the spin-complete version of SF-CIS, and

analytic derivative couplings can be derived without difficulty using the formalism described here. Collinear SF-TDDFT can be similarly extended, and a restricted open-shell formulation is also possible but has not yet been implemented. Finally, it is straightforward to extend our formalism to evaluate derivative couplings for *non-collinear* SF-TDDFT with the TDA,[12] as the analytic gradient of this method has recently been reported.[66] Extensions along these lines are currently in progress in our group, as are comparisons to TDDFT derivative couplings based on quadratic response theory.[26]

CHAPTER 4

Excited-State Deactivation Pathways in Uracil versus Hydrated Uracil

In this chapter, the application of SF-TDDFT to the study of excited-state uracil deactivation mechanism is presented. We compare the relaxation process of gas-phase uracil with that of aqueously solvated uracil. The solvatochromatic shift in the $^1n\pi^*$ state was found to be the key factor that determines the relaxation pathways.

4.1 Introduction

Upon excitation by UV light, DNA may form harmful photoproducts than can cause lethal carcinogenesis. However, the probability of photodamage is significantly reduced because of the self-repairing system in organisms. All five nucleobases, which are fundamental functioning parts of DNA, can relax back to their respective ground states within a few picoseconds following photo-excitation,[67,68] which may be an important photoprotection mechanism.

There has been significant effort in the past decade to study the excited-state deactivation mechanisms of the nucleobases, both experimentally and computationally. In particular, excited-state lifetimes of the nucleobases in both the gas phase[69] and

in aqueous solution[1] are available from time-resolved spectroscopy. Although there is some disagreement regarding the precise time constants,[1,67–71] the existence of fast and slow decay components in nucleobases is now widely accepted.

Despite the availability of such data, the details of the excited-state dynamics in assemblies of nucleobases remains to be revealed by theoretical studies. For the individual nucleobases, vertical and/or adiabatic excitation energies, conical intersection structures, and relaxation pathways have been calculated at various levels of theory,[72–75] and some excited-state dynamics simulations have been performed as well.[76–79] Where multireference methods have been employed, computational constraints limit the system size to not much more than 15 atoms. Moreover, the use of small basis sets and insufficiently large active spaces makes the reliability (for qualitatively different excited states) and accuracy (due to the limited treatment of dynamical correlation) questionable in some cases. While the importance of dynamical correlation beyond the complete active space, self-consistent field (CASSCF) model was pointed out long ago,[80] and has been investigated in detail for uracil,[73] it is difficult to extend such high-level treatments to larger systems.

Time-dependent density functional theory (TDDFT) is an attractive alternative due to its low computational cost. However, this method cannot correctly describe the topology of conical intersections involving the reference state,[10] at least not within the ubiquitous adiabatic approximation to the exchange-correlation kernel. Thus, the description of the potential surface in the important "funnel" region of near-degeneracy is highly suspicious in conventional TDDFT. A potential remedy is to use

the "spin-flip" (SF) generalization of TDDFT,[11,12,66] originally developed to investigate diradicals with strong static correlation in their ground states. In the present context, SF-TDDFT based on a high-spin triplet reference state affords a route to the singlet manifold, in which S_0 is treated on an equal footing with the singlet excited states. As such, conical intersections among singlet states pose no fundamental problem.[10] Good performance of SF-TDDFT for conical intersections in ethylene-like molecules has recently been reported,[45–48] although concerns about the suitability of choosing the lowest triplet state as the reference have been raised.[59]

In the present work, we apply SF-TDDFT to study the excited-state deactivation of uracil in both the gas phase and the aqueous solution. Several decay pathways have been suggested for photo-excited uracil, namely:

1. direct internal conversion from the lowest $^1\pi\pi^*$ state to S_0;
2. early trapping in a shallow local minimum on the lowest $^1\pi\pi^*$ state;[76,77]
3. intersystem crossing from the lowest $^1n\pi^*$ state to the lowest $^3\pi\pi^*$ state;[1] and finally
4. trapping on the lowest $^1n\pi^*$ state followed by internal conversion to S_0.[1]

In particular, mechanisms 1, 3, and 4 were proposed in an ultrafast spectroscopic study of aqueous 1-cyclohexyluracil,[1] and the diagram in Fig. 4.1 illustrates the bifurcated decay mechanism put forth in that study.

In a previous computational study,[74] a conical intersection between the $^1n\pi^*$ state and S_0 has been located but is separated by a barrier of $\approx$ 1.6 eV from the $^1n\pi^*$

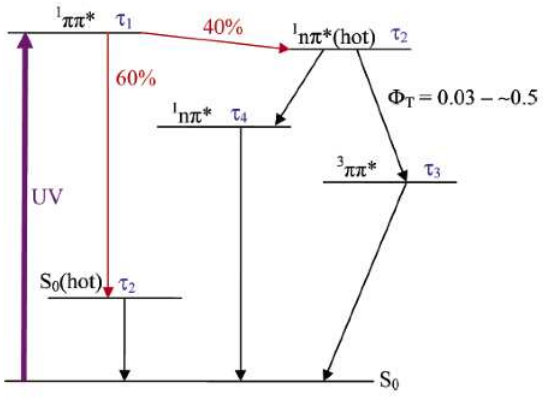

Figure 4.1: Proposed mechanism for excited-state deactivation of photo-excited 1-cyclohexyluracil, from the experimental study in Ref. 1. (Reprinted from Ref. 1; copyright 2006 American Chemical Society.)

state minimum. Meanwhile, a significant discrepancy exists in the experimentally-reported lifetime for the spectroscopically-dark $^1n\pi^*$ state in the gas phase: several nanoseconds, according to UV spectroscopy,[69,81] but only 2.4 ps according to time-resolved photoelectron spectroscopy.[71] It was later suggested that the 2.4 ps time component might be due to vibrational cooling of of a hot S_0 state populated on an ultrafast time scale, whereas the lifetime of the $^1n\pi^*$ state might be longer still.[1,74] For uracil in aqueous solution, the same lifetime is reported to be ≈ 24 ps.[1,82]

Various electronic structure methods have been deployed to study the excited-state deactivation of gas-phase uracil,[72,76,77] but only a few TDDFT calculations are available for solvated uracil.[79,83–85] The latter calculations support the role of the $^1n\pi^*$ as a "trap" along the $^1\pi\pi^* \rightarrow S_0$ relaxation pathway (see Fig. 4.1),[74] but neither conical intersections nor optimized relaxation pathways have been determined, due

to the fundamental limitations of traditional, spin-conserving TDDFT.

The present work aims for a detailed comparison between decay mechanisms for uracil in the gas phase and in aqueous solution. Due to theoretical limitations, we only consider singlet states of uracil, but note that intersystem crossing has been shown to play a minor role in the decay process, as supported by the relatively low quantum yield of the $^3\pi\pi^*$ state in solution-phase uracil ($< 10\%$ in protic solvents).[1,86] The crossing region between the $^1n\pi^*$ and S_0 states is also excluded from the current study, due to the large barrier along the reaction path that was determined previously.[74] Recently, a ring-opening conical intersection between S_0 and a $\sigma_{n\pi}\pi^*$ state, which may contribute to a new decay channel, was located computationally.[77] However, the overestimated stability of the ring-opening conformation in the CASSCF calculations of Ref. 77, along with the low fraction of the trajectories that proceed via this pathway, make it questionable whether this is really important. This pathway is not considered in the present work.

4.2 Methods

Spin-Flip TDDFT

In the present work, we use the "collinear" form of spin-flip TDDFT, first introduced by Shao *et al.*,[11] to determine excited-state relaxation pathways for uracil. (A "non-collinear" formulation of SF-TDDFT, introduced by Wang and Ziegler,[12] will be tested for some single-point calculations.) In the linear-response (LR) TDDFT approach, we need to solve the following non-Hermitian equation to get the excitation

energies, ω:

$$\begin{pmatrix} \mathbf{A} & \mathbf{B} \\ \mathbf{B}^* & \mathbf{A}^* \end{pmatrix} \begin{pmatrix} \mathbf{X} \\ \mathbf{Y} \end{pmatrix} = \omega \begin{pmatrix} \mathbf{1} & \mathbf{0} \\ \mathbf{0} & \mathbf{-1} \end{pmatrix} \begin{pmatrix} \mathbf{X} \\ \mathbf{Y} \end{pmatrix} . \tag{4.1}$$

Here,

$$\begin{aligned} A_{ia,jb} = (\epsilon_a - \epsilon_i)\, \delta_{ij}\delta_{ab} + \langle ib|aj\rangle - C_{\mathrm{HF}}\langle ib|ja\rangle \\ + \langle ib|f^{xc}|aj\rangle \end{aligned} \tag{4.2}$$

and

$$B_{ia,jb} = \langle ij|ab\rangle - C_{\mathrm{HF}}\langle ij|ba\rangle + \langle ij|f^{xc}|ab\rangle . \tag{4.3}$$

The labels $i, j, \ldots$ and $a, b, \ldots$ represent occupied and virtual spin orbitals, respectively, and C_{HF} is the fraction of Hartree-Fock exchange included in the hybrid exchange-correlation functional. Within the SF-TDDFT method, the lowest high-spin ($M_S = 1$) triplet state is chosen as the reference state, and only the $\alpha \rightarrow \beta$ spin excitation blocks in LR-TDDFT are used to obtain $M_S = 0$ for the target state. As a consequence, Eqs. (4.2) and (4.3) reduce to the following form when using a collinear exchange-correlation functional kernel:

$$A_{ia,jb} = (\epsilon_a - \epsilon_i)\, \delta_{ij}\delta_{ab} - C_{\mathrm{HF}}\langle ib|ja\rangle \tag{4.4}$$

$$B_{ia,jb} = 0 . \tag{4.5}$$

Thus, the collinear SF-TDDFT just looks like LR-TDDFT within the Tamm-Dancoff approximation, and only the Hermitian eigenvalue equation $\mathbf{AX} = \omega\mathbf{X}$ needs to be solved.

Minimum-Energy Crossing Point Optimization

In order to minimize the energy along a conical seam between electronic states I and J, we need the difference gradient vector (DGV),

$$\mathbf{g}^{IJ} = \hat{\nabla}_{\mathbf{R}}(E_I - E_J) \ , \tag{4.6}$$

and the nonadiabatic coupling vector (NACV),

$$\mathbf{h}^{IJ} = \langle \Psi_I | \hat{\nabla}_{\mathbf{R}} | \Psi_J \rangle \ . \tag{4.7}$$

Together, these two vectors define the two-dimensional branching space for the conical intersection between states I and J. Since the NACV is not available at present for the SF-TDDFT method, we adopt the branching-plane updating approach to numerically approximate the exact branching space.[62] In this method, the branching plane is updated iteratively; the (approximate) branching space at step k is spanned by the normalized DGV, which we denote as $\mathbf{x}_k$, and another unit vector $\mathbf{y}_k$ that is orthogonal to $\mathbf{x}_k$. The vector $\mathbf{y}_k$ is defined as the linear combination of $\mathbf{x}_{k-1}$ and $\mathbf{y}_{k-1}$:

$$\mathbf{y}_k = a\,\mathbf{x}_{k-1} + b\,\mathbf{y}_{k-1} \ , \tag{4.8}$$

such that $a^2 + b^2 = 1$. Since we require that $\mathbf{x}_k \cdot \mathbf{y}_k = \mathbf{0}$, one may solve for $\mathbf{y}_k$:

$$\mathbf{y}_k = \frac{(\mathbf{y}_{k-1} \cdot \mathbf{x}_k)\mathbf{x}_{k-1} - (\mathbf{x}_{k-1} \cdot \mathbf{x}_k)\mathbf{y}_{k-1}}{\left[(\mathbf{y}_{k-1} \cdot \mathbf{x}_k)^2 + (\mathbf{x}_{k-1} \cdot \mathbf{x}_k)^2\right]^{1/2}} \ . \tag{4.9}$$

The gradient projection method[13,87] is used to optimize the structures of conical intersections. In the optimizations, the gradient vector employed is

$$\mathbf{g} = 2(E_I - E_J)\mathbf{x} + \mathbf{P}\mathbf{g}_{\text{mean}}, \tag{4.10}$$

where

$$\mathbf{P} = \mathbf{1} - \mathbf{x}^\top \mathbf{x} - \mathbf{y}^\top \mathbf{y} \tag{4.11}$$

is a projection operator onto the (approximate) seam space and

$$\mathbf{g}_{\text{mean}} = \tfrac{1}{2} \hat{\nabla}_{\mathbf{R}} (E_I + E_J) \; . \tag{4.12}$$

We find this method to be much more effective as compared to the penalty-constrained minimization of $\mathbf{g}_{\text{mean}}$ that has been used in some previous studies,[10,45,46,63] and which we had originally implemented. In addition, the plane defined by vectors $\mathbf{x}_k$ and $\mathbf{y}_k$ approaches the exact branching plane very quickly after several iterations when the optimization reaches the crossing seam between the electronic states I and J.

Computational Details

In the present study, minimum-energy conical intersections and excited state relaxation pathways of uracil are calculated using SF-TDDFT in conjunction with the BH&HLYP hybrid functional (50% Hartree-Fock exchange plus 50% Becke exchange[61] with Lee-Yang-Parr correlation[41]). This somewhat unusual functional has been found to afford good results in several previous SF-TDDFT studies,[11,45] although it has been suggested that the relatively high fraction of Hartree-Fock exchange may be compensating for the non-collinear spin-flip formalism.[59] Therefore as a test, we optimized six different minimum-energy crossing point (MECP) structures, for which MR-CIS structures are available in the literature.[2] The MR-CIS and SF-BH&HLYP geometries for these MECPs are superimposed in Fig. 4.2, and are seen to be almost indistinguishable in most cases.

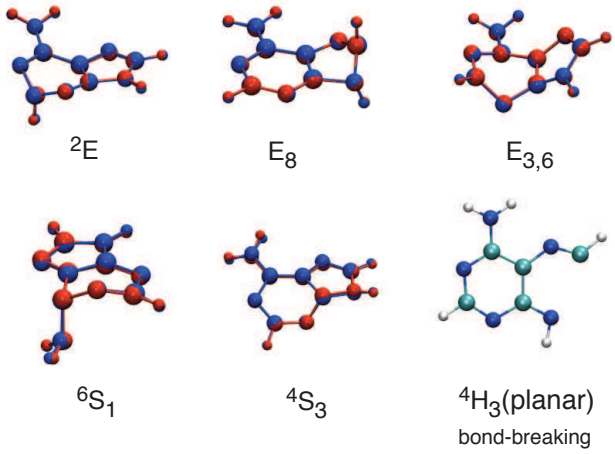

Figure 4.2: MECP structures for 9H-adenine, superimposing MR-CIS(6,5)/6-31G* results (in red, from Ref. 2) with SF-BH&HLYP/6-31G* results (in blue, this work). The nomenclature for the MECPs is taken from Ref. 2. The $^4H_3$(planar) MECP is not reported in Ref. 2 but is obtain by relaxing the (non-minimum) $^4H_3$ conical intersection reported in that work.

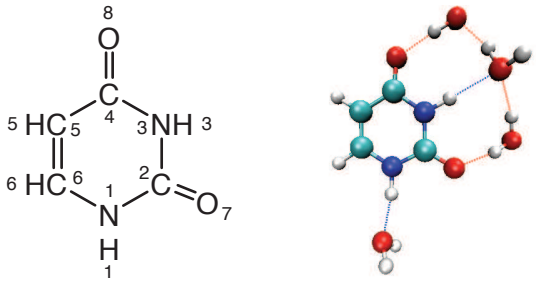

Figure 4.3: Molecular structure and numbering scheme for uracil, along with the (uracil)$(H_2O)_4$ cluster that is used to model aqueous uracil.

As a model of uracil in aqueous solution, we consider a (uracil)$(H_2O)_4$ cluster in which we add H_2O molecules at uracil's four hydrogen-bonding sites; see Fig. 4.3. (Such a model has also been used in previous studies of excited states of aqueous uracil.[85]) In addition, a smooth version of the conductor-like polarizable continuum model (C-PCM) is added,[88,89] in order to model bulk solvation.

Minimum-energy pathways for gas-phase uracil and hydrated uracil were optimized using the growing-string method[90] and the freezing-string method,[91] respectively. These methods can provide quite good approximations to exact minimum-energy pathways calculated using the intrinsic reaction coordinate method, but at lower computational cost in terms of the number of energy and gradient evaluations that are required to determine the path.[91] Mass-weighted coordinates were computed by setting the starting point structure of each string as the origin.

SF-BH&HLYP/6-31+G(d,p) was used for all gradient calculations, and energetics along the relaxation pathways were recalculated using the aug-cc-pVTZ basis set to confirm the reliability of the small basis set that is used for optimizations. (The difference in energetics between the two basis sets is less than 0.1 eV along the whole of each pathway, thus the aug-cc-pVTZ results are omitted here.) In addition, non-collinear (NC) SF-ωPBEh/6-31+G(d,p) calculations were performed along pathways optimized as indicated above, using the non-collinear formalism of Wang and Ziegler[12,66] in conjunction with the long-range corrected hybrid PBE functional, LRC-ωPBEh.[92] (The parameters $C_{\mathrm{HF}} = 0.2$ and $\omega = 0.2$ bohr^{-1} are used in LRC-ωPBEh, as suggested in Ref. 92) Finally, RI-CC2/aug-cc-pVTZ calculations (approximate coupled-cluster

theory in a resolution-of-identity implementation) were performed along the relaxation pathways obtained using SF-BH&HLYP. In general, good agreement is found amongst the energetics predicted by all of these methods.

RI-CC2 results were obtained using the TURBOMOLE package[93] and all other calculations were carried out using a development version of Q-CHEM.[33]

4.3 Results and Discussion

In this section, the results of SF-BH&HLYP calculations for photophysics of uracil are presented. Stationary-point structures and their energetics are discussed first, and the corresponding Cartesian coordinates can be found in the Supporting Information. Next, relaxation pathways optimized by string methods are reported. Finally, deactivation mechanisms for photo-excited uracil are proposed based on the relaxation pathways. Throughout this work, the equilibrium structures of S_0 and the lowest $^1n\pi^*$ state are denoted as S_0-min and $S_{n\pi^*}$-min , respectively.

4.3.1 Vertical Excitation Energies

Gas Phase Uracil

The S_0-min geometry of gas-phase uracil is planar, and the geometric parameters are presented in Table 4.1 (The labeling of atoms is shown in Fig. 4.3.) The S_0-min optimized by SF-BH&HLYP agrees well with the crystallographic structure,[94] with differences within 0.03 Å for bond lengths and 1.5° for bond angles.

Vertical excitation energies for the lowest two singlet states are presented in Table 4.2. The S_1 state with A″ symmetry has $n\pi^*$ character (excitation from the n_{O8}

Table 4.1: Stationary Point Geometries of Gas-Phase Uracil

Parameter	S_0-*min*		$S_{n\pi^*}$-*min*		*ci*-$n\pi$		*ci*-$n\pi$-p		*ci*-0π	
	DFT[a]	Expt.[b]	DFT[a]	CASSCF[c]	DFT[a]	CASSCF[c]	DFT[a]	MRCI[d]	DFT[a]	CASSCF[c]
C_2–N_3	1.372	1.373	1.388	1.378	1.369	1.371	1.421	1.335	1.372	1.358
C_2–N_1	1.377	1.379	1.356	1.369	1.399	1.415	1.419	1.410	1.417	1.421
C_6–N_1	1.367	1.380	1.409	1.405	1.350	1.337	1.313	1.330	1.346	1.325
C_5–C_6	1.341	1.338	1.365	1.408	1.479	1.500	1.517	1.511	1.432	1.447
C_4–N_3	1.395	1.383	1.385	1.393	1.420	1.432	1.469	1.462	1.421	1.433
C_4–C_5	1.456	1.440	1.364	1.364	1.372	1.382	1.390	1.415	1.468	1.487
C_4–O_8	1.205	1.227	1.385	1.361	1.255	1.252	1.195	1.205	1.199	1.194
C_2–O_7	1.206	1.218	1.209	1.200	1.205	1.197	1.216	1.216	1.200	1.199
$\angle N_1C_2O_7$	122.6	123.2	124.6	123.3	121.1	120.2	115.4	116	120.3	119.2
$\angle N_3C_4O_8$	120.4	119.9	111.3	113.2	115.9	115.3	116.4	116	119.2	117.7
$\angle N_1C_6C_5$	121.9	122.8	119.2	118.1	113.5	113.4	113.8	114	115.0	118.1
$\angle C_4C_5C_6$	119.6	119.2	117.7	117.8	116.6	114.4	119.5	122	114.3	110.4
$\angle N_1C_2N_3$	113.7	114.8	114.3	114.8	113.6	113.2	114.6		115.0	114.7
$\angle C_2N_3C_4$	127.8	127.0	122.3	122.7	121.2	119.2	119.3		126.1	126.4
$\angle N_3C_4C_5$	113.7	114.7	121.8	121.7	116.1	115.2	121.2		110.4	111.3
$\angle C_4C_5C_6H_5$	180.0	180.0	180.0	180.0	−161.1	−139.8	180.0	180	120.8	111.7
$\angle C_6C_5C_4H_6$	0.0	0.0	0.0	0.0	−12.3	−12.3	0.0	0	23.4	20.9
$\angle C_4C_5C_6N_1$	0.0	0.0	0.0	0.0	−35.2	−41.2	0.0	0	53.3	51.5
$\angle N_1C_2N_3C_4$	0.0	0.0	0.0	0.0	−28.6	−36.7	0.0	0	22.3	15.4

[a]SF-BH&HLYP/6-31+G(d,p) results (this work).
[b]Experimental values are obtained by averaging over dimensions found in crystal structures.[94]
[c]SA-3-CASSCF(10,8)/6-31G* results, from Ref. 77.
[d]MRCI1/cc-pVDZ results, from Ref. 72.

Table 4.2: Vertical Excitation Energies (in eV) for the First Two Singlet Excited States of Gas-Phase Uracil

Method	$1^1A''$ ($n\pi^*$)	$1^1A'$ ($\pi\pi^*$)
SF-BH&HLYP/6-31+G(d,p)	5.60	5.93
SF-BH&HLYP/aug-cc-pVTZ	5.54	5.84
NC-SF-ωPBEh/aug-cc-pVTZ	5.15	5.55
EOM-CCSD/6-311++G(d,p)	5.26	5.75
CR-EOM-CCSD(T)[a]	5.00	5.25
MS-CASPT2[b]	5.05	5.78
TD-PBE0[c]	4.80	5.26
RI-CC2[d]	4.80	5.35
MRCI$\sigma\pi$[e]	4.80	5.79

[a]CR-EOM-CCSD(T)/aug-cc-pVTZ, from Ref. 73.
[b]MS-3-CASPT2/SA-3-CASSCF(10,8)/6-31G*, from Ref. 77.
[c]TD-PBE0/6-311+G(2d,2p), from Ref. 85.
[d]RI-CC2/aug-cc-pVQZ, from Ref. 95.
[e]From Ref. 72.

lone pair into a π^* orbital), and the S_2 state with A$'$ symmetry is a bright $\pi\pi^*$ state. An exhaustive theoretical study of these vertical excitation energies was reported in Ref. 73, and the best theoretical estimate from that study is probably the CR-EOM-CCSD(T)/aug-cc-pVTZ result, at 5.00 eV for the S_1 state and 5.25 eV for the S_2 state. Our SF-BH&HLYP excitation energies are ≈ 0.6 eV higher, although the energy gap between S_1 and S_2 (≈ 0.3 eV) is in good agreement with the CR-EOM-CCSD(T) result. This lends some credence to the excited-state relaxation pathways described in the next section. We also note that the non-collinear formalism[12,66] for SF-TDDFT improves the vertical excitation energies by about 0.4 eV, relative to the CR-EOM-CCSD(T) benchmark. It may be interesting to examine the behavior of non-collinear SF-TDDFT when used to scan potential energy surfaces, but at present

Table 4.3: Relative Energies (in eV) at Stationary Points of Gas-Phase Uracil

	S_0-*min*			$S_{n\pi^*}$-*min*			*ci*-$n\pi$			*ci*-$n\pi$-p			*ci*-0π		
	spin-flip[a]		RI-CC2[b]	spin-flip[a]		RI-CC2[b]	spin-flip[a]		RI-CC2[b]	spin-flip[a]		RI-CC2[b]	spin-flip[a]		RI-CC2[b]
S_0	0.00	(0.00)	0.00	1.29	(1.03)	0.82	1.83	(1.66)	1.59	1.29	(1.15)	1.10	4.24	(4.05)	3.97
$^1n\pi^*$	5.60	(5.23)	4.96	4.16	(4.29)	3.85	5.17	(4.90)	4.73	5.84	(5.52)	5.38	7.14	(6.76)	6.48
$^1\pi\pi^*$	5.93	(5.64)	5.44	5.90	(5.42)	5.25	5.17	(4.82)	4.87	5.84	(5.48)	5.38	4.24	(4.01)	3.88

[a]Relative energies computed at the SF-BH&HLYP/6-31+G(d,p) level and, in parentheses, at the NC-SF-ωPBEh/6-31+G(d,p) level. Geometries are computed at the SF-BH&HLYP/6-31+G(d,p) level.
[b]Relative energies at the RI-CC2/aug-cc-pVTZ//SF-BH&HLYP/6-31+G(d,p) level.

numerically-stable analytic gradients are not available for non-LDA functionals,[66] so optimizing pathways is expensive and problematic.

SF-BH&HLYP optimization affords a planar minimum-energy geometry for the S_1 state, which agrees with the CASSCF result[77] (see Table 4.1). A previous MRCI study, however, found a slightly puckered equilibrium geometry for S_1.[72] As far as we know, the potential energy surface near $S_{n\pi^*}$-*min* is quite flat, so the results may be very sensitive to small changes in the level of electronic structure theory that is used. Compared with the ground-state minimum, the C_4–O_8 and C_5–C_6 bonds at $S_{n\pi^*}$-*min* geometry are elongated by 0.18 Å and 0.03 Å, respectively, while the C_4–C_5 bond is shortened by 0.09 Å due to excitation from the n_{O8} non-bonding orbital to an antibonding π^* orbital. The adiabatic excitation energy is 4.2 eV according to SF-BH&HLYP (see Table 4.3), in agreement with previous CASPT2 and MR-CISD results.[77] Unconstrained geometry optimization of the S_2 state by SF-BH&HLYP leads directly to the crossing region between the S_1 and S_2 states, a point to which we shall return later.

Hydrated Uracil

Solvatochromatic shifts in uracil have been studied previously at many different levels of theory.[73,85,96–99] Most studies show that the order of the lowest $^1\pi\pi^*$ and $^1n\pi^*$ states is reversed in aqueous solution, relative to that in the gas phase, with solvatochromatic shifts ranging from -0.1 to -0.3 eV for the $^1\pi\pi^*$ state and from $+0.4$–0.5 eV for the $^1n\pi^*$ state, depending on the level of theory. Our SF-BH&HLYP/C-PCM results for the microhydrated (uracil)$(H_2O)_4$ system agree well with the previous studies: the energy shifts are -0.13 eV for the $^1\pi\pi^*$ state and 0.50 eV for the $^1n\pi^*$ state (see Table 4.4).

The equilibrium geometry of the ground state is planar and similar to the gas-phase geometry. The major difference is that the two C–O bonds are ≈ 0.02 Å longer for hydrated uracil, which is caused by the hydrogen bonding interaction with the nearby water molecules, and this phenomenon manifests in the other stationary-point structures as well. We also optimized the equilibrium structure of the $^1n\pi^*$ state and found that it deviates slightly from the planar geometry, via ring puckering. The adiabatic excitation energy is reported in Table 4.4 as 4.6 eV, which is 0.4 eV higher than that for gas-phase uracil, but this solvatochromatic shift does affect the deactivation mechanisms that are discussed below. Unconstrained geometry optimization of the $^1\pi\pi^*$ state directly leads to the crossing region between the $^1\pi\pi^*$ and the S_0 states, indicating little if any barrier between the S_1 minimum and the S_1/S_0 conical intersection of hydrated uracil, at the SF-BH&HLYP level of theory.

Table 4.4: Relative Energies (in eV) at Stationary Points of Hydrated Uracil

	S_0-*min*			$S_{n\pi^*}$-*min*			*ci*-$n\pi$			*ci*-$n\pi$-p			*ci*-0π		
	spin-flip[a]		RI-CC2[b]	spin-flip[a]		RI-CC2[b]	spin-flip[a]		RI-CC2[b]	spin-flip[a]		RI-CC2[b]	spin-flip[a]		RI-CC2[b]
S_0	0.00	(0.00)	0.00	1.63	(1.22)	1.00	1.04	(0.92)	0.84	1.03	(0.87)	0.74	4.38	(4.18)	3.81
$^1\pi\pi^*$	5.80	(5.49)	5.29	6.12	(5.69)	5.37	5.38	(5.03)	4.84	5.73	(5.34)	5.06	4.38	(4.14)	4.58
$^1n\pi^*$	6.10	(5.68)	5.46	4.58	(4.72)	4.65	5.38	(5.07)	5.07	5.73	(5.40)	5.32	7.52	(7.16)	7.42

[a]Relative energies computed at the SF-BH&HLYP/6-31+G(d,p) level and, in parentheses, at the NC-SF-ωPBEh/6-31+G(d,p) level. Geometries are computed at the SF-BH&HLYP/6-31+G(d,p) level.
[b]Relative energies at the RI-CC2/aug-cc-pVTZ//SF-BH&HLYP/6-31+G(d,p) level.

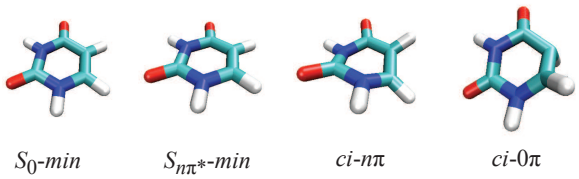

Figure 4.4: Structures optimized at the SF-BH&HLYP/6-31+G(d,p) level for gas-phase uracil. Similar critical points are obtained for hydrated uracil.

4.3.2 Conical Intersections

In the present study, we consider only the two most important MECPs that determine the main deactivation channels of uracil. The conical intersection between the $^1\pi\pi^*$ and $^1n\pi^*$ states is denoted *ci*-$n\pi$ and the one between the $^1\pi\pi^*$ and S_0 states is denoted *ci*-0π. Relative energies at these geometries are listed in Tables 4.3 and 4.4. Optimized structures in the gas phase are depicted in Fig. 4.4, and the ones for hydrated uracil are quite similar.

ci-$n\pi$

The *ci*-$n\pi$ intersection has a boat conformation with the two oxygen atoms pointing away from the ring in the same direction. For gas-phase uracil, the energy of the $^1\pi\pi^*$ state is 0.76 eV lower at *ci*-$n\pi$ than the energy at the S_0 geometry, according to the SF-BH&HLYP/6-31+G(d,p) method; this energy difference is 0.78 eV for NC-SF-ωPBEh/6-31+G(d,p) and 0.64 for RI-CC2/aug-cc-pVTZ calculations. For the hydrated uracil case, the energy lowering is 0.42 eV, 0.44 eV, and 0.34 eV, respectively, for these three methods (see Tables 4.3 and 4.4). Thus, the system always goes downhill to reach *ci*-$n\pi$ from the Franck-Condon (FC) region, for both gas-phase and hydrated uracil. Although the NC version of SF-TDDFT systematically moves the excitation energies closer to RI-CC2 results (see Tables 4.3 and 4.4), most of the discrepancy between excitation energies computed with all three methods reflects the energy difference relative to the ground state. Later, when we discuss the details of the relaxation process, we will see that all three methods afford similar energetics across the relaxation pathway.

Finally, we also optimized the structure of the planar conical intersections (labeled as *ci*-$n\pi$-p) between the $^1\pi\pi^*$ and the $^1n\pi^*$ states, for both gas-phase and hydrated uracil. The geometry of this symmetry-constrained MECP in the gas phase agrees with the one obtained at the MRCI level in Ref. 72; see Table 4.1. The change in energy in moving from the FC region of the $^1\pi\pi^*$ state to *ci*-$n\pi$-p is -0.09 eV in the gas phase [SF-BH&HLYP/6-31+G(d,p) level], as compared to -0.14 eV [NC-SF-ωPBEh/6-31+G(d,p)] and -0.06 eV (RI-CC2/aug-cc-pVTZ). For hydrated uracil,

the same energy changes are −0.07 eV, −0.12 eV and −0.10 eV, respectively. Thus, the $^1\pi\pi^*$ state energy at the *ci*-$n\pi$-p geometry is slightly lower in energy ($\approx$ 0.1 eV), or perhaps comparable to, the energy of the $^1\pi\pi^*$ state in the FC region. The potential importance of this conical intersection is discussed in the next section.

ci-0π

The *ci*-0π intersection has an ethylenic structure with pyramidalization at the C_5 atom and out-of-plane distortion at H_5 (see Fig. 4.4). The energies of *ci*-0π are 4.24 and 4.38 eV higher than the S_0-*min* energies for gas-phase uracil and hydrated uracil, respectively [SF-BH&HLYP/6-31+G(d,p) level], due to significant distortion away from a planar geometry. In the NC-SF-ωPBEh calculations, these energy differences are reduced to 4.03 eV (gas phase) and 4.16 eV (hydrated), and the RI-CC2 results are 3.92 eV (gas phase) and 4.20 eV (hydrated). We note that the energy gap between the S_0 state and the $^1\pi\pi^*$ state at *ci*-0π geometry for hydrated uracil is quite large in the RI-CC2 calculation (0.77 eV). This means that the crossing point between these two states in the RI-CC2 calculation is a little different from *ci*-0π optimized by SF-BH&HLYP. However, the relaxation pathways calculated by the two methods agree well with each other, as demonstrated in the next section.

4.3.3 Relaxation Pathways

In this section, we present optimized minimum-energy relaxation pathways connecting the critical points reported in the last section, with the aim of unraveling the excited-state deactivation mechanism(s).

Ultrafast Internal Conversion between the $^1\pi\pi^*$ and S_0 States

Immediately after photo-excitation to the first $^1\pi\pi^*$ state at the Franck-Condon geometry, the system can evolve on that excited state energy surface. Figure 4.5 shows the minimum-energy pathway connecting the S_0-min and ci-0π geometries, for both gas-phase and hydrated uracil. No barriers on the $^1\pi\pi^*$ state energy surfaces are found. Although we attempted to optimize the minimum-energy geometry for the $^1\pi\pi^*$ state, this optimization led directly to the ci-$n\pi$ crossing region in gas phase, and to the ci-0π crossing region for hydrated uracil. (Recall that the ordering of the $^1\pi\pi^*$ and $^1n\pi^*$ states in the FC region is different in the gas phase than in aqueous solution.) The system must encounter the ci-$n\pi$ funnel region in gas phase [Fig. 4.5(a)], while it can bypass the ci-$n\pi$ funnel region when evolving on the $^1\pi\pi^*$ state in aqueous solution [Fig. 4.5(b)]. This is further discussed below.

The question of whether the $^1\pi\pi^*$ state exhibits a local minimum remains a topic of debate, and the answer changes depending on the electronic structure method that is used. A shallow minimum on the $^1\pi\pi^*$ state, which would trap the uracil molecule on that state, is predicted in Refs. 76 and 77, and in those studies the slower decay component (several picoseconds) that is observed experimentally was ascribed to such trapping. The minimum-energy pathways computed here, however—along with results from attempted geometry optimizations—support the hypothesis that there does not exist any significant barrier that might trap uracil on the $^1\pi\pi^*$ state. This conclusion is reached also in several other theoretical studies.[72,74,100] Moreover, fluorescence up-conversion experiments suggest a sub-picosecond lifetime for the $^1\pi\pi^*$

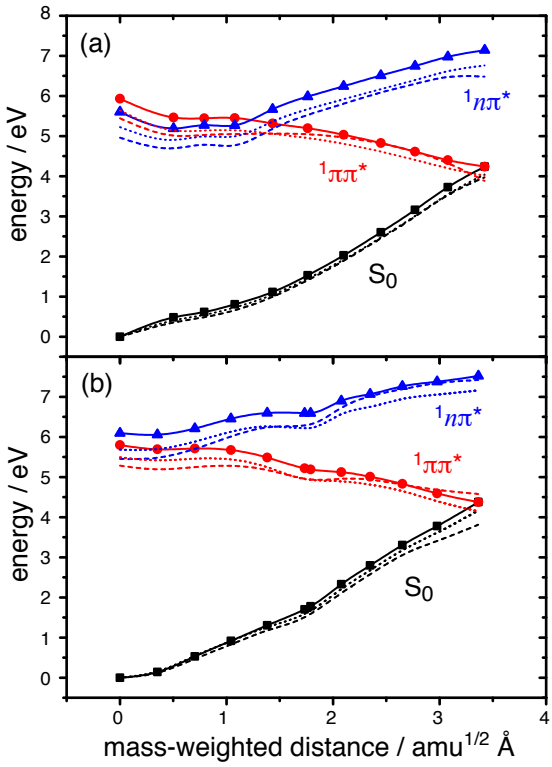

Figure 4.5: Relaxation pathways from S_0-*min* to *ci*-0π for (a) gas-phase uracil and (b) hydrated uracil, following the gradient of the $^1\pi\pi^*$ state. Solid curves connect points along the pathway that have been optimized at the SF-BH&HLYP/6-31+G(d,p) level. Energetics along that same pathway have also been computed at the NC-SF-ωPBEh/6-31+G(d,p) level (dotted curves) and the RI-CC2/aug-cc-pVTZ level (dashed curves).

state,[85] in conflict with the suggestion that trapping occurs on that state. Thus, we assign the fastest sub-picosecond decay component (called τ_1 in Ref. 1) of the optically-populated $^1\pi\pi^*$ state to direct internal conversion with the ground state.

The Role of the Long-Lived $^1n\pi^*$ Dark State

As discussed in the previous section, the energy of the $^1\pi\pi^*$ state of uracil at the *ci*-$n\pi$ geometry is smaller than that at the Franck-Condon geometry, for both gas-phase and hydrated uracil. The crossing region near *ci*-$n\pi$ is the starting point where the $^1n\pi^*$ state begins to contribute to the deactivation process. Figure 4.6 depicts minimum-energy pathways of the $^1\pi\pi^*$ state connecting S_0-*min* and *ci*-$n\pi$ configurations. The reaction pathway is barrierless for gas-phase uracil [Fig. 4.6(a)], while a small barrier of < 0.1 eV is found for hydrated uracil [Fig. 4.6(b)]. Although we attempted to find a local minimum on the latter pathway, geometry optimizations invariably led to the crossing region between the S_0 and $^1\pi\pi^*$ states. Meanwhile, due to the large excess energy gained by the system after photo-excitation, the small barrier predicted in the hydrated case should be easily overcome. For these reasons, we conclude that aqueous uracil excited to the $^1\pi\pi^*$ state will evolve directly to *ci*-0π or to *ci*-$n\pi$ without any trapping on the $^1\pi\pi^*$ state.

In the previous section, we mentioned the existence of a planar conical intersection (*ci*-$n\pi$-p), for both gas-phase and hydrated uracil. The mass-weighted distances between S_0-*min* and *ci*-$n\pi$-p structures are 1.00 amu$^{1/2}$ Å (gas phase) and 1.07 amu$^{1/2}$ Å (hydrated), which should be compared with the lengths of the pathways connecting S_0-*min* and *ci*-$n\pi$ in Fig. 4.6, which are larger than 2 amu$^{1/2}$ Å. This indicates that

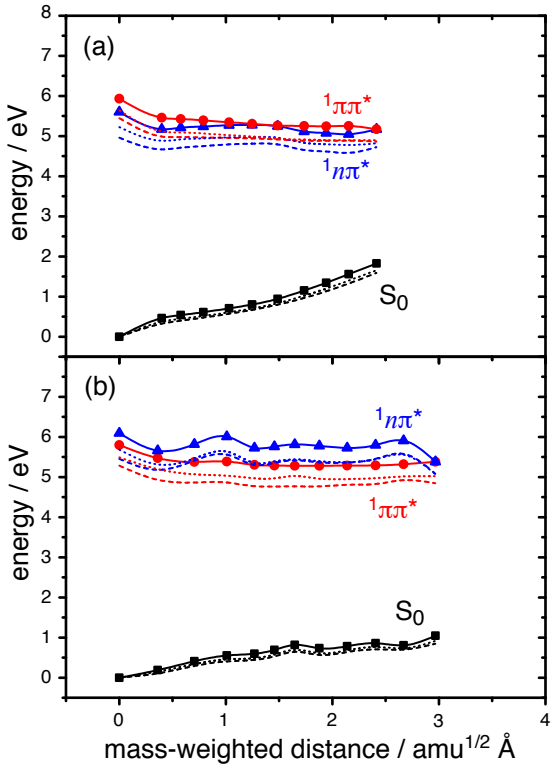

Figure 4.6: Relaxation pathways from S_0-*min* to *ci*-$n\pi$ for (a) gas-phase uracil and (b) hydrated uracil, following the gradient of the $^1\pi\pi^*$ state. Solid curves connect points along the pathway that have been optimized at the SF-BH&HLYP/6-31+G(d,p) level. Energetics along that same pathway have also been computed at the NC-SF-ωPBEh/6-31+G(d,p) level (dotted curves) and the RI-CC2/aug-cc-pVTZ level (dashed curves).

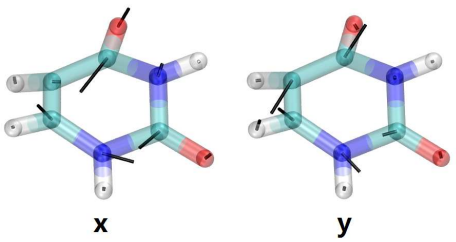

Figure 4.7: Optimized **x** and **y** vectors (black line segments) at the *ci*-$n\pi$ conformation of gas-phase uracil.

the crossing regions between the $^1\pi\pi^*$ state and the $^1n\pi^*$ state are geometrically close to the FC region in both the gas phase and in solution. Keeping in mind the excess vibrational energy after photo-excitation and the fact that the $^1\pi\pi^*$ state in both the gas-phase and hydrated case is similar between S_0-*min* and *ci*-$n\pi$-p, we propose that the system can reach the crossing seam between the $^1\pi\pi^*$ state and the $^1n\pi^*$ state very early after photo-excitation, which is associated with the sub-picosecond decay component, τ_1.

After the system encounters the intersection seam between the $^1\pi\pi^*$ and $^1n\pi^*$ states, the wave function is a mixture of $\pi\pi^*$ and $n\pi^*$ character. The reaction pathway may bifurcate in two directions, depending on which character the wave function takes after the system leaves the crossing region, as already shown in previous studies.[72,77] Examining the branching-space vectors **x** and **y** at the *ci*-$n\pi$ geometry, which are shown in Fig. 4.7. We see that **x** is mainly the C_4–O_8 bond stretch, which leads to $S_{n\pi^*}$-*min*, while **y** is the C_4–C_5 stretch combined with ring puckering, which leads to *ci*-0π.

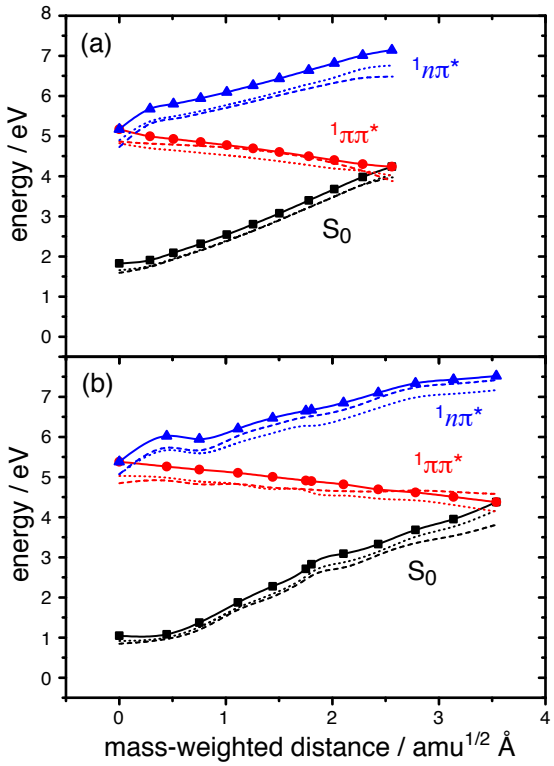

Figure 4.8: The relaxation pathways from *ci*-$n\pi$ to *ci*-0π for (a) gas-phase uracil and (b) hydrated uracil, following the gradient of the $^1\pi\pi^*$ state. Solid curves connect points along the pathway that have been optimized at the SF-BH&HLYP/6-31+G(d,p) level. Energetics along that same pathway have also been computed at the NC-SF-ωPBEh/6-31+G(d,p) level (dotted curves) and the RI-CC2/aug-cc-pVTZ level (dashed curves).

If the diabatic $\pi\pi^*$ character is maintained during the decay process, then the system will evolve directly toward *ci*-0π (see Fig. 4.8). For the situation in the gas phase, this decay component is just a part of the direct ultrafast internal conversion between the $^1\pi\pi^*$ and S_0 states. Because the state ordering of $^1\pi\pi^*$ and $^1n\pi^*$ changes along the decay pathway [Fig. 4.5(a)], the system has to cross the intersection seam between these two states. The situation for hydrated uracil is slightly different. In the Franck-Condon region, the S_1 state has $\pi\pi^*$ character while the S_2 state has $n\pi^*$ character. From Fig. 4.5(b), we note that the system need not encounter the crossing seam between the $^1\pi\pi^*$ and $^1n\pi^*$ states in order to decay toward *ci*-0π. Thus, the decay channel FC $\rightarrow$ *ci*-$n\pi$ $\rightarrow$ *ci*-0π is distinct from the one in Fig. 4.5(b), namely FC $\rightarrow$ *ci*-0π, in the case of hydrated uracil. We next explain this conclusion.

In Fig. 4.9, we report the minimum-energy pathways connecting S_0-*min*, *ci*-$n\pi$ and *ci*-0π, projected onto a two-dimensional reaction coordinate plane. Here, the horizontal axis represents the geometry change between S_0-*min* and *ci*-0π, which is defined as the direction of the vector

$$\mathbf{a} = \mathbf{R}_{ci\text{-}0\pi} - \mathbf{R}_{S_0\text{-}min} \tag{4.13}$$

The vertical axis represents the geometry change between S_0-*min* and *ci*-$n\pi$, but with the direction of the horizontal axis projected out. This corresponds to the direction of the vector

$$\mathbf{b} = (\mathbf{1} - \hat{\mathbf{a}}^\top \hat{\mathbf{a}})(\mathbf{R}_{ci\text{-}n\pi} - \mathbf{R}_{S_0\text{-}min}) \tag{4.14}$$

where $\hat{\mathbf{a}} = \mathbf{a}/||\mathbf{a}||$. In the gas phase, we see from Fig. 4.9(a) that the paths FC $\rightarrow$ *ci*-$n\pi$ and *ci*-$n\pi$ $\rightarrow$ *ci*-0π are quite close to the path FC $\rightarrow$ *ci*-0π, so there is essentially

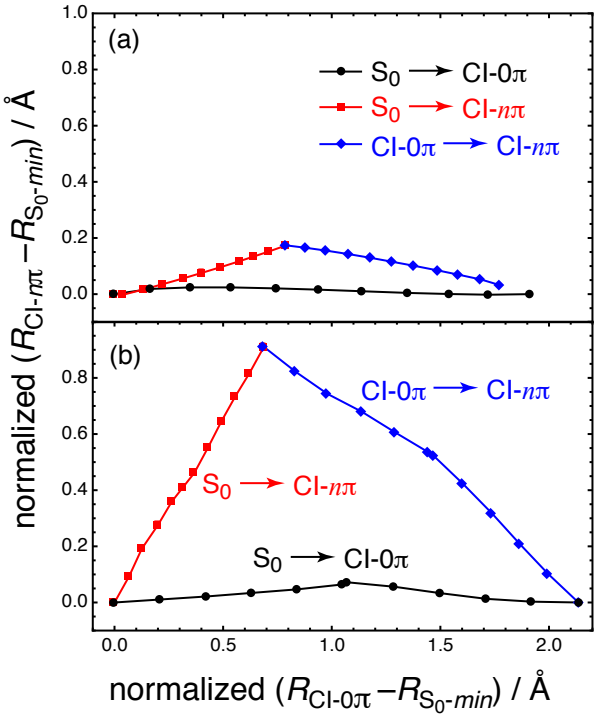

Figure 4.9: Projected relaxation pathways S_0-min $\rightarrow$ ci-0π (black curve), S_0-min $\rightarrow$ ci-$n\pi$ (red curve), and ci-$n\pi$ $\rightarrow$ ci-0π (blue curve), for (a) gas-phase uracil and (b) hydrated uracil. The directions of the horizontal and vertical axes are defined in Eqs. (4.13) and (4.14), respectively.

only one decay channel from the Franck-Condon geometry to *ci*-0π, going through the $^1\pi\pi^*/^1n\pi^*$ intersection seam. For hydrated uracil [Fig. 4.9(b)], the paths FC $\rightarrow$ *ci*-$n\pi$ and *ci*-$n\pi \rightarrow$ *ci*-0π are far away from the path FC $\rightarrow$ *ci*-0π, and combined with the pathway shown in Fig. 4.5(b), we conclude that the intersection seam between the $^1\pi\pi^*$ and $^1n\pi^*$ states does not lie in the same region of the potential surface as the decay channel FC $\rightarrow$ *ci*-0π.

In order to further explain the above conclusion, we did an extensive potential energy surface (PES) scan at the level of SF-BH&HLYP/6-31+G(d,p) near the three relaxation pathways shown in Fig. 4.9. The surfaces thus obtained are shown in Fig. 4.10. Note that the *ci*-$n\pi$ point shown in Fig. 4.10(b) is not the real MECP on the $^1\pi\pi^*/^1n\pi^*$ crossing seam that is depicted in Fig. 4.4, because we did not perform geometry relaxations for the PES, but the energy increase is only 0.17 eV. Consequently, the position of the $^1\pi\pi^*/^1n\pi^*$ crossing seam in Fig. 4.10(b) represents the position of the seam through which the system can cross *near* the *ci*-$n\pi$ MECP. Comparing the PES of gas-phase uracil to that of its hydrated analogue, it is clear that the $^1\pi\pi^*/^1n\pi^*$ crossing seam moves far away from the FC region for hydrated uracil, as a direct result of the solvatochromatic shifts for the $^1\pi\pi^*$ and $^1n\pi^*$ states. In Fig. 4.10, the red curves on the $^1\pi\pi^*$ state are the minimum relaxation pathways connecting the critical points. For gas-phase uracil, only one decay channel is found, namely, FC $\rightarrow$ $^1\pi\pi^*/^1n\pi^*$ seam $\rightarrow$ *ci*-0π. For hydrated uracil, however, we observe a broad, nearly barrierless region enclosed by the three relaxation pathways on the $^1\pi\pi^*$ state. Thus, the system is free to either evolve to the $^1\pi\pi^*/^1n\pi^*$ crossing seam

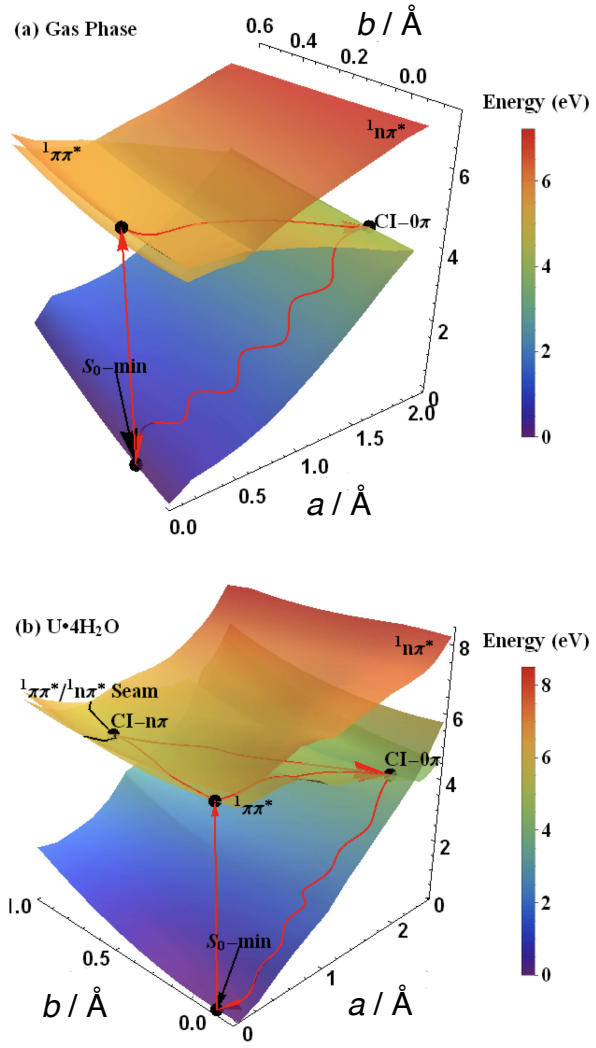

Figure 4.10: Potential energy surfaces for the lowest three singlet states for (a) gas-phase uracil and (b) hydrated uracil. The **a** and **b** axes are defined in Eqs. (4.13) and (4.14).

then return back to the $^1\pi\pi^*/S_0$ seam, or directly travel toward the $^1\pi\pi^*/S_0$ seam without reaching the $^1\pi\pi^*/^1n\pi^*$ crossing region.

As such, there are two decay channels from the FC geometry to *ci*-0π for uracil in aqueous solution, namely, FC $\rightarrow$ *ci*-0π and FC $\rightarrow$ $^1\pi\pi^*/^1n\pi^*$ seam $\rightarrow$ *ci*-0π. However, since both of these two channels are downhill on the $^1\pi\pi^*$ surface, we do not expect significantly different time constants in time-resolved experiments; both channels correspond to the fastest decay component (τ_1).

The wave function can also take $n\pi^*$ character after the system encounters the $^1\pi\pi^*/^1n\pi^*$ crossing seam. In Fig. 4.11, we see that the system can travel on the $^1n\pi^*$ surface barrierlessly toward $S_{n\pi^*}$-*min*. In the solution phase, this process is associated with the vibrational cooling of the $^1n\pi^*$ state. Because of the existence of this stable equilibrium structure ($S_{n\pi^*}$-*min*), the system can be trapped on the $^1n\pi^*$ state for a relatively longer time (τ_4 in Ref. 1), from tens of picoseconds to several nanoseconds, depending on whether the solvent is protic or aprotic.

Figure 4.12 shows the relaxation pathways connecting $S_{n\pi^*}$-*min* and *ci*-0π. In order to go back to the crossing region between the $^1\pi\pi^*$ and S_0 states, the system has to overcome a relatively large energy barrier ($\approx$ 1.0 eV in gas phase and $\approx$ 0.7 eV for hydrated uracil at the SF-BH&HLYP level), and this is the reason for the long lifetime of the dark singlet state that is observed in time-resolved experiments. (At the . NC-SF-ωPBEh level, the barrier drops from 0.61 eV for gas-phase uracil to 0.39 eV for hydrated uracil, while RI-CC2 results are 1.1 eV for gas-phase uracil and 0.4 eV for hydrated uracil.) This lowering of the barrier upon hydration may be the reason

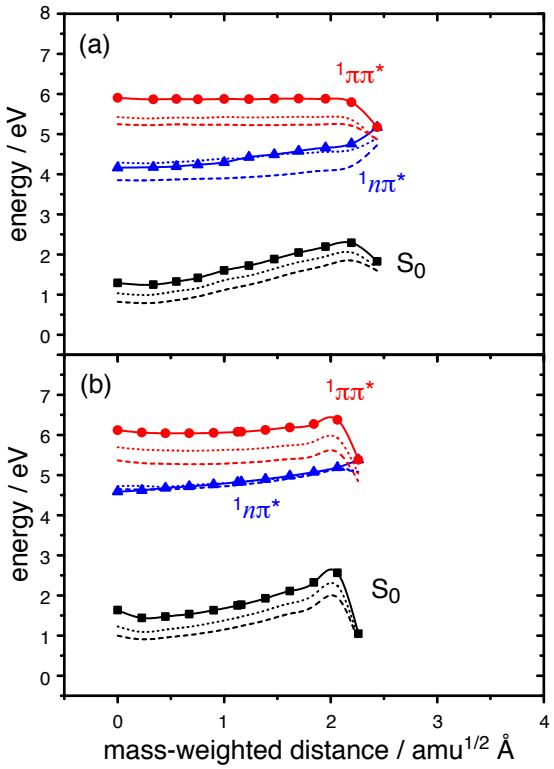

Figure 4.11: The relaxation pathways from $S_{n\pi^*}$-*min* to *ci*-$n\pi$ for (a) gas-phase uracil and (b) hydrated uracil, following the gradient of the $n\pi^*$ state. Solid curves connect points along the pathway that have been optimized at the SF-BH&HLYP/6-31+G(d,p) level. Energetics along that same pathway have also been computed at the NC-SF-ωPBEh/6-31+G(d,p) level (dotted curves) and the RI-CC2/aug-cc-pVTZ level (dashed curves).

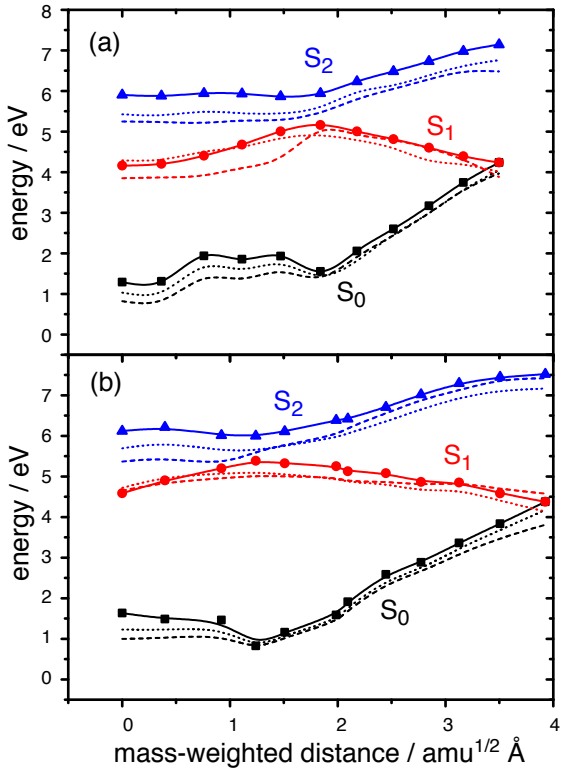

Figure 4.12: The relaxation pathways from $S_{n\pi^*}$-*min* to *ci*-0π for (a) gas-phase uracil and (b) hydrated uracil, following the gradient of the S_1 state. The wave function changes character from $n\pi^*$ to $\pi\pi^*$ at the maximum energy point on the S_1 pathway, so the reaction pathways come across the $^1\pi\pi^*/^1n\pi^*$ crossing regions and lead the system back to the $^1\pi\pi^*$ surface. [Solid curves represent the pathway optimized at the SF-BH&HLYP/6-31+G(d,p) level, whereas energetics along that same pathway are also computed at the NC-SF-ωPBEh/6-31+G(d,p) level (dotted curves) and the RI-CC2/aug-cc-pVTZ level (dashed curves).]

for the shorter lifetime (τ_4) of the singlet dark state in protic solvents as compared to aprotic solvents.[1] A similar conclusion was reached in a previous TDDFT study.[74]

The Quantum Yield of the $^1n\pi^*$ State

Transient absorption spectroscopy indicates that the quantum yield of the ultrafast internal conversion through *ci*-0π is $\sim$60% (for all solvents examined experimentally), and the remaining 40% of the quantum yield was ascribed to some combination of deactivation to the singlet $^1n\pi^*$ dark state and to the triplet $^3\pi\pi^*$ dark state.[1] If we assume that the $^3\pi\pi^*$ state is obtained by intersystem crossing from the $^1n\pi^*$ state, as proposed in Ref. 1, then the quantum yield of the $^1n\pi^*$ state can be taken as $\sim$40% after decay through the $^1\pi\pi^*/^1n\pi^*$ crossing region, in all solvents.

In the present study, if we assume the deactivation mechanism of uracil in the gas phase is similar to that in aprotic solvents, where no hydrogen bonds are formed between uracil and the solvent molecules, then it is possible to study the quantum yield of the $^1n\pi^*$ state for uracil in different solvents. In the previous discussion, we saw that the major difference of the decay channels for gas-phase uracil and hydrated uracil is that the direct deactivation from the $^1\pi\pi^*$ state to the ground state through the *ci*-0π conical intersection for hydrated uracil can bypass the $^1\pi\pi^*/$ $^1n\pi^*$ crossing region. Thus, the probability for the system to reach the *ci*-$n\pi$ crossing seam may be smaller for hydrated uracil. In other words, the quantum yield of the dark $^1n\pi^*$ state may be lower for uracil in protic solvents. However, this effect may be minor due to the excess energy at photo-excitation which may lead the system to the energetically unfavored but geometrically closer *ci*-$n\pi$ crossing seam (see the

discussion above regarding the *ci*-$n\pi$-p conical intersection). In any case, the quantum yield of the singlet dark state of uracil in protic solvents appears to be governed by the competition between the FC $\rightarrow$ *ci*-0π and the FC $\rightarrow$ *ci*-$n\pi$ decay channels. Careful dynamics calculations are required in order to understand the details.

4.4 Conclusions

Spin-flip TDDFT is capable of correctly describing the topology of a conical intersection,[10] without increasing the computational cost relative to standard TDDFT, and affords minimum-energy crossing point geometries along conical seams that are in good agreement with benchmark results from multireference wave function methods. In the present study, we have applied SF-TDDFT to examine the excited-state deactivation mechanisms of both gas-phase and hydrated uracil, by first locating the two most important MECPs, then optimizing reaction pathways connecting various stationary points with the MECPs, and finally confirming the energetics using coupled-cluster calculations. Based on the pathways thus obtained, we have assigned the time constants measured in time-resolved experiments.

Our calculations support the deactivation mechanism proposed by Hare *et al.*[1] and later suggested also by Mercier *et al.*[74] based on TDDFT calculations, and the present work provides additional evidence in the form of optimized MECP structures. The ultrafast decay component $\tau_1 = 120$ fs that is measured experimentally[1] is assigned to direct relaxation from the first $^1\pi\pi^*$ state to the ground state state via conical intersection *ci*-0π, whereas the slow component[1] ($\tau_4 = 26$ ps) is assigned to indirect

relaxation, via the pathway $^1\pi\pi^* \rightarrow {}^1n\pi^* \rightarrow S_0$. The lifetime of the dark $^1n\pi^*$ state is observed to increase from tens of picoseconds in protic solvents to several nanoseconds in aprotic solvents,[1] and this behavior is ascribed to solvatochromatic shifts that serve to decrease a key activation barrier on the $^1n\pi^*$ state. Finally, we find no evidence that trapping should occur on the $^1\pi\pi^*$ state, either in the gas phase or in aqueous solution.

More generally, our results for both uracil and adenine suggest that SF-TDDFT can describe the excited state properties of nucleobases qualitatively correctly and at relatively low cost. If we limit the discussion to relative energies of singlet excited states, then SF-TDDFT results agree very well with the CC2 results, although excitation energies with respect to S_0 are overestimated with respect to experiment and CC2 results. This overestimation is largely corrected by SF-TDDFT calculations within the non-collinear formalism, at least for uracil. This shift relative to S_0 may be due to the relatively large fraction of Hartree-Fock exchange (50%) that is found to yield best results for collinear SF-TDDFT,[11,45] which may be an an artifact of the collinear formalism.[59] Non-collinear exchange-correlation kernels may therefore be better choices for future work, although gradients are not yet available. In any case, the low cost of SF-TDDFT makes it use promising for application to larger nucleic acid assemblies.

One final cautionary note, which is especially relevant in the context of *ab initio* molecular dynamics, is that to use SF-TDDFT one must identify and eliminate the $M_S = 0$ component of the triplet from the singlet excitation manifold. In our hands,

this is sometimes quite difficult away from the Franck-Condon region, owing to significant spin contamination. Recently, Li *et al.*[101] introduced a spin-adapted formalism for the open-shell random phase approximation, using the tensor equation of motion formalism.[102] This approach offers a potential solution to the spin contamination issue. Meanwhile, calculation of analytic first-order nonadiabatic coupling vectors for TDDFT is available at the linear response level,[23,24] and the extension to SF-TDDFT is straightforward. This would obviate the need for the gradient projection algorithm used here, as MECP optimization could proceed directly along the vectors **g** and **h**. Efforts to improve SF-TDDFT along these lines are underway in our group.

CHAPTER 5

Spin-flip, Tensor Equation-of-Motion Configuration Interaction with a Density-Functional Correction

In this chapter, we introduce the spin-adapted version of SF-TDDFT that cures the spin contamination problem of conventional SF-TDDFT. Preliminary numerical results show that this new method is potentially a much more attractive approach to excited-state *ab initio* MD simulations, as compared to SF-TDDFT.

5.1 Introduction

Spin-flip time dependent density functional theory[11,12] (SF-TDDFT) is a qualitatively correct and very efficient electronic structure method for describing electronic excitation energies,[11,12,66,103–106] conical intersections,[14,107] excited-state reaction pathways,[14,45–49,59,108–111] and excited-state non-adiabatic *ab initio* molecular dynamics (MD) simulations.[112,113] Spin-flipping excitations enable SF-TDDFT to treat ground- and excited-state electron correlation on the same footing, while also incorporating some doubly-excited determinants that are important for biradicals.[11,44] The dynamical correlation that is included in SF-TDDFT makes this model more accurate than its wavefunction analogue, spin-flip configuration-interaction singles (SF-CIS).[44]

Despite these favorable features, SF-TDDFT has one notorious drawback in the form of serious spin contamination. This can easily be understood using an example in which a high-spin triplet reference state is used in order to target singlet states obtained from a single $\alpha \rightarrow \beta$ spin-flip excitation. Figure 5.1 depicts all possible electron configurations obtained in such a scenario, using a model consisting of four electrons in four orbitals. Only those excitations within the open-shell space are able to generate spin-pure solutions, whereas all other configurations are missing their "spin complements", leading to spin-contaminated solutions. In this example, at most three singlet states and one triplet state may exhibit proper spin symmetry, whereas all other solutions will be significantly spin-contaminated. This is a serious drawback in SF-TDDFT, especially for *ab initio* MD or excited-state optimizations, where states may cross as the molecular geometry is changed and some form of state-tracking is required. Since the number of spin-pure states is limited, only a few low-lying states can be studied in SF-TDDFT simulations,[112,113] and various techniques are required in order to follow the state having the desired spin symmetry.[112]

Several approaches have been proposed to generate spin eigenstates for open-shell TDDFT. Vahtras and Rinkevicius[114] introduced general excitation operators that can be used to generate excited states having well-defined spin multiplicities, whereas Li and Liu[65,101,115] extended the tensor equation-of-motion (TEOM) formalism, originally developed by Rowe and co-workers in nuclear physics,[102] to the case of molecular systems. At the SF-CIS level, Sherrill and co-workers[3] presented a

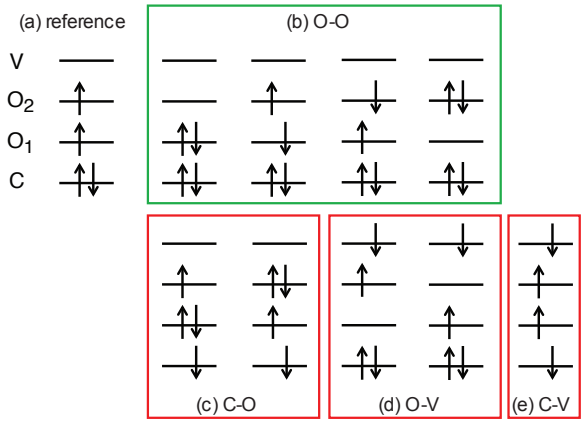

Figure 5.1: Example of spin-flip from a high-spin triplet reference state, for a model system consisting of four electrons in four orbitals. Configuration (a) is the reference state. Configurations in (b) are obtained by a single flip-down excitation within the open-shell orbitals; only these configurations are able to form spin eigenstates. Configurations in (c)–(e) are obtained by closed- to open-shell excitations, open-shell to virtual excitations, and closed-shell to virtual excitations, respectively, each with a $\alpha \rightarrow \beta$ spin-flip excitation. These configurations are missing their complementary spin configurations and lead to spin-contaminated solutions in conventional SF-TDDFT.

spin-complete implementation within a restricted active space formalism, and Tsuchimochi *et al.*[116,117] reported a spin-projected formulation of SF-CIS in which spin-adapted solutions are also obtained. None of these approaches, however, has been applied to SF-TDDFT,which is the topic of the present work. We will derive a spin-adapted, spin-flip CIS method (SA-SF-CIS) based on one of three formally equivalent TEOMs.[102] To incorporate dynamical electron correlation, we will then go on to include a DFT correction, following along the lines that Grimme *et al.*[118,119] used to merge DFT with multireference configuration interaction (MRCI) in the DFT/MRCI method. The performance of this new method is then analyzed through some example calculations.

5.2 Theory

We briefly review the TEOM formalism introduced by Rowe *et al.*,[102] then derive the working equations for SA-SF-CIS based on this formalism.

5.2.1 Notation

The following notation is used throughout this work. Doubly- and singly-occupied molecular orbitals are labeled as $\phi_i, \phi_j, \phi_k, \phi_l, \ldots$ and $\phi_t, \phi_u, \phi_v, \phi_w, \ldots$, respectively, while virtual molecular orbitals are labeled as $\phi_a, \phi_b, \phi_c, \phi_d, \ldots$. We label arbitrary (occupied or virtual) molecular orbitals as $\phi_p, \phi_q, \phi_r, \phi_s, \ldots$. All two-electron integrals will be written in physicists' notation. Furthermore, we will use C, O and V to denote closed, open, and virtual spaces, respectively, consistent with Fig. 5.1. A tensor operator having rank Γ is denoted as $\hat{O}^\dagger(\Gamma)$ and its μth component is $\hat{O}^\dagger(\Gamma, \mu)$.

5.2.2 Tensor equations of motion

The traditional scalar equations of motion[120] can be generalized to tensor equations of motion in a straightforward way using tensor basis functions insdead of scalar basis functions.[102] One seeks the tensor operators $\hat{O}^{\dagger}_{x\lambda}$ with rank λ that relate the excited tensor state $|xS_f\rangle\rangle$ to some reference tensor state $|S_0\rangle\rangle$ in the following way,

$$\left\{\hat{O}^{\dagger}_{x\lambda} \times |S_0\rangle\rangle\right\}^{S_f} = |xS_f\rangle\rangle \tag{5.1}$$

$$\hat{O}_{x\lambda}|S_0\rangle\rangle = 0 \ . \tag{5.2}$$

We use curly brackets to represent the coupled products between two tensors, and the superscript above the bracket is the rank of the product tensor. The labels S_0 and S_f indicate the spin symmetries of the initial (reference) state and the final (target) state, respectively. (Note that S_0 as used in Section 5.2 does not mean "singlet ground state", S_0. The latter notation is used in the numerical calculations in Section 5.3.) In Eq. (5.2), all possible coupled products should vanish. The tensor operator $\hat{O}^{\dagger}_{x\lambda}$ can be expanded by a series of tensor operators with different ranks,

$$\hat{O}^{\dagger}_{x\lambda} = \sum_i \hat{O}^{\dagger}_{x\lambda_i} \ , \tag{5.3}$$

and the ranks λ_i must satisfy the triangle relations required by Eq. (5.1), namely

$$|S_0 - S_f| \leq \lambda_i \leq |S_0 + S_f| \ . \tag{5.4}$$

As shown by Rowe *et al.*,[102] three formally equivalent TEOMs can be derived from

Eqs. (5.1) and (5.2). The first of these is

$$\begin{aligned}
&\sum_{ij\Gamma}(-1)^{S_0-S_f-\Gamma-\lambda_i}(2\Gamma+1)^{1/2}W(\lambda_i\lambda_j S_0 S_0;\Gamma S_f) \\
&\quad\times\left\langle S_0\middle|\middle|\left\{\hat{\overline{O}}_{y\lambda_i}\times[\hat{H},\hat{O}^\dagger_{x\lambda_j}]\right\}^\Gamma\middle|\middle|S_0\right\rangle \\
&=\omega_{xS_f}\sum_{ij\Gamma}(-1)^{S_0-S_f-\Gamma-\lambda_i}(2\Gamma+1)^{1/2}W(\lambda_i\lambda_j S_0 S_0;\Gamma S_f) \\
&\quad\times\left\langle S_0\middle|\middle|\left\{\hat{\overline{O}}_{y\lambda_i}\times\hat{O}^\dagger_{x\lambda_j}\right\}^\Gamma\middle|\middle|S_0\right\rangle . \qquad (5.5)
\end{aligned}$$

The second version is

$$\begin{aligned}
&\sum_{ij\Gamma}(-1)^{S_0-S_f-\Gamma-\lambda_i}(2\Gamma+1)^{1/2}W(\lambda_i\lambda_j S_0 S_0;\Gamma S_f) \\
&\quad\times\left\langle S_0\middle|\middle|\left\{[\hat{\overline{O}}_{y\lambda_i},[\hat{H},\hat{O}^\dagger_{x\lambda_j}]]\right\}^\Gamma\middle|\middle|S_0\right\rangle \\
&=\omega_{xS_f}\sum_{ij\Gamma}(-1)^{S_0-S_f-\Gamma-\lambda_i}(2\Gamma+1)^{1/2}W(\lambda_i\lambda_j S_0 S_0;\Gamma S_f) \\
&\quad\times\left\langle S_0\middle|\middle|\left\{[\hat{\overline{O}}_{y\lambda_i},\hat{O}^\dagger_{x\lambda_j}]\right\}^\Gamma\middle|\middle|S_0\right\rangle . \qquad (5.6)
\end{aligned}$$

Finally, the third TEOM is

$$\begin{aligned}
&\sum_{ij\Gamma}(-1)^{S_0-S_f-\Gamma-\lambda_i}(2\Gamma+1)^{1/2}W(\lambda_i\lambda_j S_0 S_0;\Gamma S_f) \\
&\quad\times\left\langle S_0\middle|\middle|\left\{[\hat{\overline{O}}_{y\lambda_i},\hat{H},\hat{O}^\dagger_{x\lambda_j}]\right\}^\Gamma\middle|\middle|S_0\right\rangle \\
&=\omega_{xS_f}\sum_{ij\Gamma}(-1)^{S_0-S_f-\Gamma-\lambda_i}(2\Gamma+1)^{1/2}W(\lambda_i\lambda_j S_0 S_0;\Gamma S_f) \\
&\quad\times\left\langle S_0\middle|\middle|\left\{[\hat{\overline{O}}_{y\lambda_i},\hat{O}^\dagger_{x\lambda_j}]\right\}^\Gamma\middle|\middle|S_0\right\rangle . \qquad (5.7)
\end{aligned}$$

The quantity W in these equations is a Racah coefficient, $\hat{\overline{O}}_{y\lambda_i}$ is the tensor operator corresponding to the Hermitian adjoint of $\hat{O}^\dagger_{y\lambda_i}$,[102] ω_{xS_f} is the excitation energy from $|S_0\rangle\rangle$ to $|xS_f\rangle\rangle$, and the sums over i and j are sums over all tensor operators with

different ranks λ_i and λ_j, as in Eq. (5.3)]. The only difference amongst the three TEOMs in Eqs. (5.5)–(5.7) comes in the reduced matrix elements, $\langle S_0||\{\cdots\}^{\Gamma}||S_0\rangle$.

In order to derive Eq. (5.6) from Eq. (5.5), the so-called "killer condition" [Eq. (5.2)] must be satisfied. Equation (5.7) is equivalent to Eq. (5.6) only if $|S_0\rangle\rangle$ is an eigenfunction of the Hamiltonian $\hat{H}$. Amongst these three TEOMs, Eq. (5.7) has the favorable features that the double commutator in the reduced matrix elements has lower rank as compared to the first formulation in Eq. (5.5), and furthermore that both sides of the Eq. (5.7) are Hermitian.[102] If the killer condition is not satisfied, however, then use of either Eq. (5.6) or Eq. (5.7) may be problematic, as discussed below.

5.2.3 Spin-adapted, spin-flip CIS

In this work, the excitation operators involved in the TEOMs are truncated at the single excitation level. In other words, we only focus on removing the spin contamination in traditional (spin-incomplete) spin-flip CIS and its time-dependent Hartree-Fock (TD-HF) extension. Higher-order excitation operators could in principle be included to introduce additional electron correlation.

Single excitation operators can be grouped into two kinds of tensors, one having rank zero (singlet coupling) and the other having rank one (triplet coupling).[121]

Meanwhile, Eqs. (5.5)–(5.7) require the following triangle relations to be fulfilled:

$$|S_0 - S_f| \leq \lambda_i \leq |S_0 + S_f| \tag{5.8a}$$

$$|S_0 - S_f| \leq \lambda_j \leq |S_0 + S_f| \tag{5.8b}$$

$$|\lambda_i - \lambda_j| \leq \Gamma \leq |\lambda_i + \lambda_j| \tag{5.8c}$$

$$|S_0 - S_0| \leq \Gamma \leq |S_0 + S_0| \ . \tag{5.8d}$$

In spin-flip methods, we usually look for the excited states whose total spin angular momentum is one unit smaller than that of the reference state, $S_f = S_0 - 1$. Thus, only triplet-coupled single excitation operators (*i.e.*, $\lambda_i = \lambda_j = 1$) satisfy the above triangle relations. These tensor operators have the following components when represented in the molecular orbital (MO) basis:

$$\hat{O}^\dagger_{pq}(1,1) = -\hat{a}^\dagger_p \, \hat{a}_{\bar{q}}, \tag{5.9a}$$

$$\hat{O}^\dagger_{pq}(1,0) = \frac{1}{\sqrt{2}}(\hat{a}^\dagger_p \, \hat{a}_q - \hat{a}^\dagger_{\bar{p}} \, \hat{a}_{\bar{q}}), \tag{5.9b}$$

$$\hat{O}^\dagger_{pq}(1,-1) = \hat{a}^\dagger_{\bar{p}} \, \hat{a}_q, \tag{5.9c}$$

where $\hat{a}^\dagger_p$ creates an α-spin electron in orbital ϕ_p and $\hat{a}_{\bar{q}}$ annihilates a β-spin electron in orbital ϕ_q.

Previous work by Li and Liu uses Eq. (5.7) as the working equation.[65,101,115] However, in the SF-CIS case, the killer condition in Eq. (5.2) is not satisfied for excitations within the open-shell space, and as a result both Eq. (5.6) and Eq. (5.7) will generate spurious solutions. The reason is that the excitation space is overcomplete, but Eqs. (5.6) and (5.7) are not capable of removing this overcompleteness. Consequently,

we choose Eq. (5.5) as our working equation, and we will show that this equation automatically removes the overcompleteness of the excitation space, by symmetry.

An alternative way to solve this problem is to introduce an operator that projects out the reference state, so that the killer condition is fulfilled by construction. This procedure has been shown to be successful in scalar equation-of-motion calculations.[122] We can also extend this approach to TEOMs, simply by writing the tensor operators in Eqs. (5.1) and (5.2) with the following general forms:

$$\hat{O}^{\dagger}_{x\lambda} = \sum_i (-1)^{S_f-\lambda_i} \left(\frac{2S_f+1}{2\lambda_i+1}\right)^{1/2} \left\{ \{ O^{\dagger}_{x\lambda_i} |S_0\rangle\rangle \}^{S_f} \langle\langle S_0| \right\}^{\lambda_i} \tag{5.10a}$$

$$\hat{O}_{x\lambda} = \sum_i (-1)^{S_f-\lambda_i} \left(\frac{2S_f+1}{2\lambda_i+1}\right)^{1/2} \left\{ |S_0\rangle\rangle \{ \langle\langle S_0| O_{x\lambda_i} \}^{S_f} \right\}^{\lambda_i} . \tag{5.10b}$$

Given these two tensor operators, the killer condition [Eq. (5.2)] is always satisfied, and the three TEOMs in Eqs. (5.5)–(5.7) become formally equivalent if $|S_0\rangle\rangle$ is an eigenfunction of the Hamiltonian. This is not, however, the approach that is pursued here.

Now we can express the TEOM in Eq. (5.5) using the spin-tensor basis shown in Eq. (5.9). This results in the following matrix representation of the TEOM,

$$\mathbf{MZ}(x) = \omega_x \mathbf{NZ}(x) \ , \tag{5.11}$$

where the matrix elements of $\mathbf{M}$ and $\mathbf{N}$ are

$$M_{pq,rs} = \sum_{\Gamma}(-1)^{S_0-S_f-\Gamma-1}(2\Gamma+1)^{1/2}W(11S_0S_0;\Gamma S_f) \times \left\langle S_0\middle|\middle|\left\{\hat{\overline{O}}_{pq}(1)\times[\hat{H},\hat{O}^{\dagger}_{rs}(1)]\right\}^{\Gamma}\middle|\middle|S_0\right\rangle \tag{5.12}$$

$$N_{pq,rs} = \sum_{\Gamma}(-1)^{S_0-S_f-\Gamma-1}(2\Gamma+1)^{1/2}W(11S_0S_0;\Gamma S_f) \times \left\langle S_0\middle|\middle|\left\{\hat{\overline{O}}_{pq}(1)\times\hat{O}^{\dagger}_{rs}(1)\right\}^{\Gamma}\middle|\middle|S_0\right\rangle . \tag{5.13}$$

The reduced matrix elements in Eqs. (5.12) and (5.13) can be evaluated using the Wigner-Eckart theorem,

$$\left\langle\Gamma\middle|\middle|\hat{O}(\lambda)\middle|\middle|\Gamma_1\right\rangle = \frac{\sqrt{2\Gamma+1}}{C(\Gamma_1\mu_1\lambda\nu;\Gamma\mu)}\left\langle\Gamma\mu\middle|\hat{O}(\lambda,\nu)\middle|\Gamma_1\mu_1\right\rangle , \tag{5.14}$$

where C is a Clebsch-Gordan coefficient, $|\Gamma\mu\rangle$ denotes an angular momentum eigenstate whose total angular momentum is Γ and whose z-component is μ, and $\langle\Gamma||\hat{O}(\lambda)||\Gamma_1\rangle$ is the reduced matrix element. Using Eq. (5.14), the reduced matrix elements in $\mathbf{M}$ can be expressed as

$$\left\langle S_0\middle|\middle|\left\{\hat{\overline{O}}_{pq}(1)\times[\hat{H},\hat{O}^{\dagger}_{rs}(1)]\right\}^{\Gamma}\middle|\middle|S_0\right\rangle = \frac{(2\Gamma+1)^{1/2}\left\langle S_0S_0\middle|\left\{\hat{\overline{O}}_{pq}(1)\times[\hat{H},\hat{O}^{\dagger}_{rs}(1)]\right\}^{\Gamma}_{0}\middle|S_0S_0\right\rangle}{C(S_0S_0\Gamma 0;S_0S_0)} . \tag{5.15}$$

In the notation $|S_0S_0\rangle$, the first S_0 is the total spin quantum number and the second S_0 represents the quantum number for the z-component of the spin vector, which makes $|S_0S_0\rangle$ a high-spin state. In Eq. (5.15), we use the normal spin-flip convention wherein the high-spin open-shell state $|S_0S_0\rangle$ is taken to be the reference state.

The numerator of the right side of Eq. (5.15), which is a coupled product between excitation operators, can be derived readily:

$$\begin{aligned}
&\big\langle S_0 S_0 \big| \big\{ \hat{\bar{O}}_{pq}(1) \times [\hat{H}, \hat{O}^\dagger_{rs}(1)] \big\}^\Gamma_0 \big| S_0 S_0 \big\rangle \\
&= \sum_\mu \big\langle S_0 S_0 \big| \hat{\bar{O}}_{pq}(1,-\mu) \times [\hat{H}, \hat{O}^\dagger_{rs}(1,\mu)] \big| S_0 S_0 \big\rangle \\
&\qquad \times C(1(-\mu)1\mu;\Gamma 0) \; .
\end{aligned} \tag{5.16}$$

The quantity $\hat{\bar{O}}_{pq}(1,-\mu)$ is defined as[102]

$$\hat{\bar{O}}_{pq}(1,-\mu) = (-1)^{1-\mu} \hat{O}_{pq}(1,\mu). \tag{5.17}$$

Finally, the matrix elements of $\mathbf{M}$ can be evaluated. The results are very similar to those derived by Li and Liu,[101] based on the TEOM in Eq. (5.7), and the details are relegated to an Appendix. The matrix elements of $\mathbf{N}$ can be derived in the same way, nevertheless it is worth demonstrating the structure of $\mathbf{N}$, since this is what guarantees that the overcompleteness of the excitation space is removed automatically. We next proceed to demonstrate this structure.

For SA-SF-CIS, we choose p and q in Eq. (5.9) to run over all MOs. Namely, $\hat{O}^\dagger(1)$ is expanded in the following way if we neglect the redundant excitations:

$$\begin{aligned}
\hat{O}^\dagger(1) = &\sum_{ai} \hat{O}^\dagger_{ai}(1) X^{\mathrm{CV}}_{ai} + \sum_{ui} \hat{O}^\dagger_{ui}(1) X^{\mathrm{CO}}_{ui} \\
&+ \sum_{au} \hat{O}^\dagger_{au}(1) X^{\mathrm{OV}}_{au} + \sum_{tu} \hat{O}^\dagger_{tu}(1) X^{\mathrm{OO}}_{tu} \\
&+ \sum_{ia} \hat{O}^\dagger_{ia}(1) Y^{\mathrm{VC}}_{ia} + \sum_{iu} \hat{O}^\dagger_{iu}(1) Y^{\mathrm{OC}}_{iu} \\
&+ \sum_{ua} \hat{O}^\dagger_{ua}(1) Y^{\mathrm{VO}}_{ua}.
\end{aligned} \tag{5.18}$$

In Eq. (5.18), we use $\mathbf{X}$ and $\mathbf{Y}$ to represent the excitation and de-excitation parts of the amplitude, respectively. Superscripts on the quantities X_{pq} and Y_{qp} indicate the excitation type, *e.g.*, X_{ai}^{CV} is the coefficient for excitation of one electron from a closed-shell, doubly-occupied MO ϕ_i and into a virtual MO ϕ_a. Using the spin-tensor basis above, the matrix $\mathbf{N}$ can be expressed explicitly as $\mathbf{N} = \mathbf{N_{XX}} \oplus \mathbf{N_{YY}}$ where

$$\mathbf{N_{XX}} = \begin{pmatrix} \delta_{ij}\delta_{ab} & 0 & 0 & 0 \\ 0 & \left(\frac{2S_0+1}{2S_0}\right)\delta_{ij}\delta_{uv} & 0 & 0 \\ 0 & 0 & \left(\frac{2S_0+1}{2S_0}\right)\delta_{uv}\delta_{ab} & 0 \\ 0 & 0 & 0 & \mathbf{N^{OO\text{-}OO}} \end{pmatrix} , \tag{5.19}$$

and $\mathbf{N_{YY}} = \mathbf{0}$. The block $\mathbf{N^{OO\text{-}OO}}$ is the only part of $\mathbf{N_{XX}}$ that is not diagonal. This block is singular, with matrix elements

$$N_{tu,vw}^{\text{OO-OO}} = -\left(\frac{2S_0+1}{2S_0(2S_0-1)}\right)\delta_{tu}\delta_{vw} + \left(\frac{2S_0+1}{2S_0-1}\right)\delta_{tv}\delta_{uw} \, . \tag{5.20}$$

The rank of $\mathbf{N^{OO\text{-}OO}}$ is less than its dimension, which removes the overcompleteness of the OO excitation space. For example, if $S_0 = 1$ and $S_f = 0$ (singlet states from a high-spin triplet reference), then $\mathbf{N^{OO\text{-}OO}}$ can be expressed as

$$\mathbf{N_{S_0=1}^{OO\text{-}OO}} = \begin{pmatrix} \frac{3}{2} & 0 & 0 & -\frac{3}{2} \\ 0 & 3 & 0 & 0 \\ 0 & 0 & 3 & 0 \\ -\frac{3}{2} & 0 & 0 & \frac{3}{2} \end{pmatrix} \tag{5.21}$$

which has a rank of 3. It is easy to show that all possible single spin-flipping excitations within the open-shell space from a high-spin triplet reference state will generate three singlet states and one triplet state. That the matrix in Eq. (5.21) has rank 3 rather than 4 guarantees that the one triplet state is excluded from the solutions. At this point, we have proved that by using Eq. (5.5) as the working equation for

SA-SF-CIS, all the solutions will have the correct spin eigenvalue and no spurious solutions will be generated.

It is also interesting to note that the de-excitation part of the TEOM vanishes, *i.e.*, $\mathbf{N_{YY}} = \mathbf{0}$. As such, there is no concept of a "Tamm-Dancoff approximation",[35] since $\mathbf{Y} \equiv \mathbf{0}$, and the SA-SF-CIS method derived here reduces to the spin-complete SF-CIS method introduced of Sherrill and co-workers.[3] The benefit of our TEOM-based derivation is that we don't have to add more electron configurations into the CI equations, as was done in Ref. 3. Actually, the matrix dimensions of $\mathbf{M}$ and $\mathbf{N}$ in SA-SF-CIS are exactly the same as those in (spin-incomplete) SF-CIS, due to the spin-tensor basis that is used here. In other words, the spin contamination in SF-CIS can be removed without additional computational cost by applying the TEOM approach.

5.2.4 DFT correction

In principle, the current SA-SF-CIS method can be extended to its corresponding DFT counterpart by introducing a Hamiltonian $\hat{H}^{\mathrm{DFT}}$ associated to density functional theory. This Hamiltonian is required to generate the exact ground-state energy from the single-determinant reference state, $E_0^{\mathrm{exact}} = \langle S_0|\hat{H}^{\mathrm{DFT}}|S_0\rangle$. Unfortunately, no such Hamiltonian is known in analytic form. Instead, we propose an empirical correction to the matrix elements in the SA-SF-CIS working equation to capture dynamical correlation using a density functional. The motivation behind this *ad hoc* correction is similar in spirit to the idea that underlies the DFT/MRCI method.[118,119] We will denote our method as SA-SF-DFT.

In DFT/MRCI, the major correction from DFT is added to the diagonal matrix elements of the MRCI Hamiltonian in the following way. Using singly-excited Slater determinants $|\Phi_{pq}\rangle$ rather than configuration state-functions as the basis, we have

$$\langle\Phi_{pq}|\hat{H}^{\mathrm{DFT}} - E_0^{\mathrm{DFT}}|\Phi_{pq}\rangle = \tag{5.22}$$
$$F_{pp}^{\mathrm{KS}} - F_{qq}^{\mathrm{KS}} + \langle pq||qp\rangle + p_J\langle pq|pq\rangle - p(N_o)\langle pq|qp\rangle \ .$$

Here, $|\Phi_{pq}\rangle$ indicates $q \rightarrow p$ excitation, E_0^{DFT} is the ground-state DFT energy, $\mathbf{F}^{\mathrm{KS}}$ is the Kohn-Sham Fock matrix, p_J is a fitting parameter, and $p(N_o)$ is an empirical function depending on the number of open shells, N_o. The quantities p_J and $p(N_o)$ are optimized for each density functional, and for the BH&HLYP functional,[123] good performance is obtained for $p_J = 1 - C_{\mathrm{HF}} = 0.5$. (Re-parameterization is required for functionals having a substantially different fraction of Hartree-Fock exchange.[119])

Since the correction from $\langle pq|pq\rangle$ is usually larger than that from $\langle pq|qp\rangle$, we will neglect the final term in Eq. (5.22) in our method. Moreover, we set $p_J = 1 - C_{\mathrm{HF}}$, and apply the correction to all matrix elements including off-diagonal terms, for simplicity. The matrix elements in SA-SF-DFT therefore have the following form:

$$\langle\Phi_{pq}|\hat{H}^{\mathrm{DFT}} - E_0^{\mathrm{DFT}}|\Phi_{rs}\rangle = \delta_{qs}F_{pr}^{\mathrm{KS}} - \delta_{pr}F_{qs}^{\mathrm{KS}}$$
$$+ \langle pq||qp\rangle + (1 - C_{\mathrm{HF}})\langle pq|pq\rangle. \tag{5.23}$$

This is precisely the same matrix element as in collinear SF-TDDFT,[11] which provides some justification for the generally good performance of that method. In principle, we could tune the value of p_J in collinear SF-TDDFT for any density functional, in an effort to obtain accurate energetics. As such, the requirement of $\approx 50\%$ Hartree-Fock

exchange for good results in collinear SF-TDDFT, which was discovered empirically in Ref. 11, may actually depend upon how we "translate" the CI method to TDDFT, and may have less to do with spin contamination, as was suggested in Ref. 101. Additional evidence in support of this argument comes from non-collinear SF-TDDFT, which usually performs well with less Hartree-Fock exchange,[59,66] despite the fact that it is also spin contaminated. This is mainly because the CI method and TDDFT are connected in a different way, namely, through non-collinear kernels, and the parameterization approach for non-collinear SF-TDDFT is distinct from that for collinear SF-TDDFT.

Besides the simple form of Eq. (5.23), there is another advantage to calculating the matrix elements in this way. The Wigner-Eckart theorem is used in deriving the TEOMs, and this theorem assumes that the components of a spin tensor are energetically degenerate because the Hamiltonian of the system is spin-independent. This degeneracy is satisfied only if we use the same Hamiltonian to calculate the ground-state energy and the matrix elements in the TEOM. Equation (5.23), based on a restricted open-shell Hartree-Fock[51] (ROHF) reference state, satisfies the spin-degeneracy condition,[101] and thus partly removes the ambiguity associated with application of the Wigner-Eckart theorem. Some ambiguity remains, insofar as the Kohn-Sham Fock matrix that is used in Eq. (5.23) is calculated from a different Hamiltonian as compared to $\hat{H}^{\mathrm{DFT}}$.

Although in principle it would be possible to use non-collinear exchange-correlation

(XC) functionals to add a DFT correction to SA-SF-CIS, we will use collinear functionals exclusively. The reason is that the ROHF reference state exactly satisfies the degeneracy condition amongst the various components of a spin multiplet, and the form of the collinear matrix elements [Eq. (5.23)] does not alter this fact. For non-collinear functionals, the form of the **K** matrices introduced in the Appendix is altered in a way that may not respect the spin-degeneracy condition.[101] (Li and Liu[101] suggest how empirical parameters could be introduced to partially restore this degeneracy, but we will not attempt this here.)

Note that the use of Eq. (5.23) in conjunction with a spin-complete formalism does engender some double-counting of electron correlation. The same can be said of DFT/MRCI, and in that method the off-diagonal matrix elements are modified in an attempt to counterbalance some of this double-counting.[119] Similar modifications may help the SA-SF-DFT method, but we have not pursued these yet. It should be noted that collinear SF-TDDFT itself is already subject to some double-counting.

5.3 Numerical examples

The SA-SF-DFT method has been implemented in a locally modified version of the Q-Chem program,[33] and in this section we evaluate its performance. All calculations were performed using Q-Chem except for some benchmark MRCI calculations, which were performed using the Orca program.[124] The examples that we consider here involve singlet excitations starting from a high-spin ROHF reference state[51] for the triplet. It should be noted that the formalism is more general than triplet-to-singlet

spin-flipping transitions, however. The spin states S_0 and S_f (Section 5.2) can be any integer or half-integer values, subject to the constraint that $S_f = S_0 - 1$.

5.3.1 Ethylene torsion

Ethylene torsion is a prototypical example for testing how electronic structure methods describe biradicals. Collinear SF-TDDFT performs well for this system,[11] whereas most spin-conserving, single-reference methods (*e.g.*, TDDFT or EOM-CCSD) fail to yield smooth potential curves at the D_{2d} geometry,[116] because the ground and excited states are described in an unbalanced manner.

Here, we study potential energy curves along the double-bond twisting coordinate of the singlet N, V, and Z states. We compare collinear SF-TDDFT, SA-SF-DFT, and SA-SF-CIS potential energy curves to those obtained at the MRCI singles and doubles level. The BH&HLYP functional[123] is used for the DFT calculations, and a CAS(2,2) singlet ground state is used as the reference state for the MRCI calculations. Potential scans along the torsion coordinate use the cc-pVTZ basis set starting from the equilibrium geometry optimized at the ωB97X-D/6-31G* level. Potential scans are plotted in Fig. 5.2.

All four of the aforementioned methods are in good agreement with each other for the N state, except that the two DFT methods slightly overestimate the barrier height and SA-SF-CIS slightly underestimates it, as compared to the MRCI result. For the V and Z states, potential curves computed using the two DFT methods exhibit quantitative agreement with MRCI results, whereas the excitation energies predicted by SA-SF-CIS are more than 1 eV too large at the D_{2d} geometry. This is undoubtedly

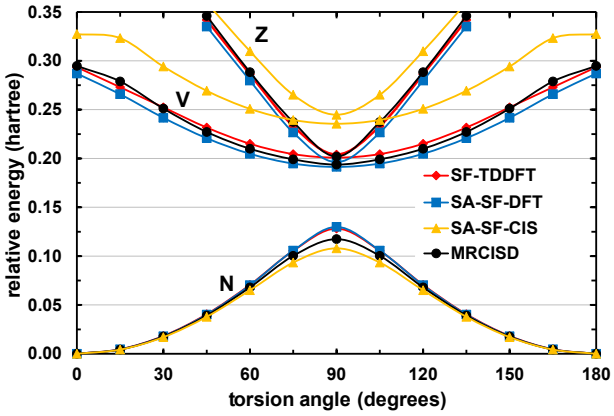

Figure 5.2: Potential energy curves along the double-bond torsion coordinate of ethylene, for the singlet states N, V, and Z. The SF-TDDFT results use the collinear formalism, and note that SA-SF-CIS (without the *ad hoc* DFT correction) is equivalent to the spin-complete SF-CIS method of Ref. 3. The zero in energy corresponds to the singlet ground state at its equilibrium geometry.

due in large part to the lack of dynamical correlation in this approach, and the same effect was seen recently in time-dependent projected Hartree Fock calculations of twisted ethylene.[116] Nevertheless, each of the methods examined here produces a smooth potential curve and at least quasi-degeneracy between the V and Z states at the D_{2d} geometry. This is because all three spin-flip approaches (and MRCI as well) treats the ground and excited states in a balanced manner, and include the most important double excitations.

Note also that there is essentially no difference between SA-SF-DFT and collinear SF-TDDFT results for the ethylene torsion problem. This is not surprising given that the latter approach exhibits nearly zero spin contamination for the electronic states in question. Recalling that we construct the matrix elements of SA-SF-DFT in the

Table 5.1: Vertical excitation energies (in eV) for the lowest two singlet excited states of the five nucleobases. For collinear SF-TDDFT, the value of $\langle \hat{S}^2 \rangle$ is given in parentheses, in units of $\hbar^2$.

Nucleobase	SA-SF-DFT		Collinear SF-TDDFT		Benchmark	
	S_1	S_2	S_1	S_2	S_1	S_2
uracil	5.35	5.56	5.50 (1.09)	5.80 (0.16)	5.00[a]	5.25[a]
adenine	5.24	5.28	4.79 (1.09)	5.31 (1.11)	5.13[b]	5.20[b]
thymine	5.21	5.66	5.60 (1.08)	5.66 (0.16)	5.14[c]	5.60[c]
cytosine	4.74	5.60	5.28 (0.29)	5.45 (1.04)	4.76[d]	5.24[d]
guanine	5.02	5.18	4.95 (1.04)	5.02 (1.05)	4.76[b]	5.09[b]
MAE[e]	0.16	0.18	0.40	0.20		

[a]CR-EOM-CCSD(T)/aug-cc-pVTZ results from Ref. 73.

[b]CAS(10,10)PT2/ANO-double-ζ results from Ref. 125.

[c]EOM-CCSD/TZVP results from Ref. 126.

[d]CR-EOM-CCSD(T)/cc-pVDZ results from Ref. 127.

[e]Mean absolute error with respect to the benchmarks.

same way as in collinear SF-TDDFT [Eq. (5.23)], these two methods become identical in cases where SF-TDDFT exhibits no spin contamination.

5.3.2 Vertical excitation energies of nucleobases

Previous collinear SF-TDDFT studies have shown that this method tends to overestimate vertical excitation energies for nucleobases,[49] and it is interesting to examine whether SA-SF-DFT can correct this problem. Equilibrium structures of the nucleobases were optimized at the B3LYP/6-311G(2df,2pd) level, and then SA-SF-DFT and collinear SF-TDDFT excitation energies were computed at the BH&HLYP/aug-cc-pVTZ level.

Table 5.1 summarizes the vertical excitation energies of the lowest two singlet excited states for all five nucleobases, along with benchmark results from correlated

wavefunction calculations. For the collinear SF-TDDFT calculations, values of $\langle \hat{S}^2 \rangle$ are listed as well. Since most of the states in the collinear SF-TDDFT calculations are heavily spin-contaminated, with $\langle \hat{S}^2 \rangle \approx 1$ (in units of $\hbar^2$), we assign those states with $\langle \hat{S}^2 \rangle < 1.5$ to be singlet states.

We observe that SA-SF-DFT affords reasonable excitation energies for the S_1 and S_2 states of all five nucleobases, with a mean absolute error (MAE) 0.17 eV. For the S_1 state, collinear SF-TDDFT affords a large MAE (0.40 eV), although the MAE for the S_2 state is comparable at 0.20 eV. It is possible that the reasonable performance of the heavily spin-contaminated SF-TDDFT calculations is accidental, since averaging over the triplet and singlet states sometimes results in good excitation energies in unrestricted TDDFT calculations for open-shell systems,[115] and many of the ostensibly singlet excitations computed using SF-TDDFT in Table 5.1 are better described as roughly equal mixtures of singlet and triplet.

Considering the similarity of the matrix elements in DFT/MRCI [Eq. (5.22)] and collinear SA-SF-DFT [Eq. (5.23)], one might anticipate comparable performance given an appropriate reference state. [For example, a high-spin triplet reference state in SA-SF-DFT corresponds to a CAS(2,2) reference state in MRCI.] On the other hand, the traditional, collinear SF-TDDFT approach with the same functional (*e.g.* BH&HLYP) usually show much worse performance, especially near the Franck-Condon region. From the examples in Sections 5.3.1 and 5.3.2, we may conclude that the poor performance of collinear SF-TDDFT is mostly caused by the spin contamination, while an XC functional with $\approx 50\%$ Hartree-Fock exchange should still be a

reasonable choice for collinear SF-TDDFT.

In a previous study of the nucleobases using range-separated hybrid functionals with non-empirical tuning, a MAE of 0.19 eV for the $S_0 \rightarrow S_1$ excitations was reported.[128] This further suggests that the performance of SA-SF-DFT is perhaps about the best that one can expect from contemporary TDDFT. Based on these few, simple tests, we can say that the correction to excitation energies that is obtained by removing the spin contamination in collinear SF-TDDFT is sizable, and SA-SF-DFT seems like a promising method.

5.3.3 State assignment in SF-TDDFT

Although there are a few examples of *ab initio* MD simulations using SF-TDDFT,[46,112,113] and other examples of using SF-TDDFT to locate minimum-energy crossing points (MECPs) along conical seams,[45,47–49,109] the spin contamination problem makes it challenging to assign the excited states correctly and consistently across the potential energy surface. Here, we demonstrate this problem with numerical examples.

Nonadiabatic *ab initio* MD

We carried out a fewest-switches surface hopping simulation[7] of uracil, using collinear SF-TDDFT at the BH&HLYP/6-31G* level. Three successive snapshots along one trajectory, spanning only 1 fs of simulation time, serve to demonstrate the state assignment problem; excitation energies and $\langle \hat{S}^2 \rangle$ values for these snapshots are given in Table 5.2. Within the time window presented in the table, the S_1 and T_1 states change their order, but this can be difficult to detect in the heavily spin-contaminated

Table 5.2: Excitation energies for three sequential time steps of a surface-hopping simulation of gas-phase uracil performed at the BH&HLYP/6-31G* level.

time/fs	SA-SF-DFT/RPA		Collinear SF-TDDFT			SF-RASCI	
	state	ω/eV	state	ω/eV	$\langle\hat{S}^2\rangle/\hbar^2$	state	ω/eV
26.6	S_1	2.36	S_1	2.05	(1.18)	S_1	2.39
			T_1	2.19	(1.81)		
	S_2	3.82	S_2	3.66	(0.63)	S_2	3.85
27.1			T_1	2.12	(1.52)		
	S_1	2.37	S_1	2.20	(1.51)	S_1	2.44
	S_2	3.83	S_2	3.72	(0.66)	S_2	3.90
27.6			T_1	2.14	(1.91)		
	S_1	2.39	S_1	2.24	(1.15)	S_1	2.47
	S_2	3.82	S_2	3.76	(0.65)	S_2	3.93

SF-TDDFT calculations. The consequence of an incorrect state assignment in an *ab initio* MD simulation (or excited-state geometry optimization, for that matter) might be energy jumps, propagation on the wrong state, and other nonsense ultimately leading to incorrect relaxation times and branching ratios, or even convergence failure. As such, an effective state-tracking algorithm is required whenever SF-TDDFT is used to move about an excited-state potential energy surface.

A straightforward way to do this, which we have sometimes found to be effective, is to monitor the change in the excited-state transition density. Within the Tamm-Dancoff approximation, this quantity is

$$T(\mathbf{r},\mathbf{r}') = \sum_{ai} X_{ai}\,\phi_i(\mathbf{r})\,\phi_a(\mathbf{r}')\ . \tag{5.24}$$

Let us denote the transition density at a subsequent geometry as

$$\widetilde{T}(\mathbf{r},\mathbf{r}') = \sum_{bj} \widetilde{X}_{bj}\, \widetilde{\phi}_j(\mathbf{r})\, \widetilde{\phi}_b(\mathbf{r}') \; . \tag{5.25}$$

We wish to examine the overlap integral

$$\begin{aligned} \int d\mathbf{r}\; d\mathbf{r}'\; T(\mathbf{r},\mathbf{r}')\; \widetilde{T}(\mathbf{r}',\mathbf{r}) &= \sum_{ijab} X_{ai} \widetilde{X}_{bj} \langle \phi_i | \widetilde{\phi}_j \rangle \langle \phi_a | \widetilde{\phi}_b \rangle \\ &= \mathrm{tr}(\mathbf{X}\mathbf{C}^\dagger \mathbf{S} \widetilde{\mathbf{C}} \widetilde{\mathbf{X}}^\dagger \widetilde{\mathbf{C}}^\dagger \mathbf{S}^\dagger \mathbf{C}) \; , \end{aligned} \tag{5.26}$$

where $S_{\mu\nu} = \langle \mu | \widetilde{\nu} \rangle$ is the overlap between the atomic orbitals at the two different geometries. Based on the overlaps between various transition densities, and the assumption that it is possible to assign spin multiplicities to the SF-TDDFT states at the Franck-Condon geometry, one may hope to track those multiplicities as the geometry and excited states evolve in time.

The aforementioned state-tracking procedure was used to assign multiplicities to the SF-TDDFT calculations reported in Table 5.2. Note that if the assignment were based solely on the value of $\langle \hat{S}^2 \rangle$, *e.g.*, with states having $\langle \hat{S}^2 \rangle > 1.5$ assigned as triplets, then at $t = 27.1$ fs we would assign as S_1 the state that is actually labeled as S_2 in Table 5.2. This illustrates the extent to which $\langle \hat{S}^2 \rangle$ completely fails as a reliable quantum number in SF-TDDFT, which in our experience is quite common away from the Franck-Condon region.[49]

On the other hand, the state-tracking procedure suggested in Eq. (5.26) is not guaranteed to work, especially in nonadiabatic MD simulations. Each spin-contaminated state in SF-TDDFT is a mixture of different spin multiplicities, and when the two states with different multiplicities (singlet and triplet in the present example) become nearly degenerate, their wavefunctions usually vary smoothly with respect to nuclear

geometry. This is analogous to an avoided crossing between two strongly coupled states, and state-tracking algorithms can easily fail to identify a change in the ordering of two states with different multiplicities. As such, the most reliable way to solve the state assignment problem is to use spin-adapted methods.

Table 5.2 also lists SA-SF-DFT excitation energies for uracil along with benchmarks computed at the level of spin-flip restricted active space configuration interaction (SF-RASCI).[129] We computed these benchmarks using a large active space [RAS(2,10)-SF] to ensure accuracy, and we find that they agree very well with SA-SF-DFT calculations. This demonstrates that the SA-SF-DFT approach not only cures the state assignment problem, but also improves upon collinear SF-TDDFT energetics. As such, SA-SF-DFT appears to be a promising method for nonadiabatic *ab initio* MD simulations.

Optimization of MECPs

As another example to demonstrate the state assignment problem in SF-TDDFT, we searched for the MECP along the crossing seam between the S_0 and S_1 states of ethylene, using both SF-TDDFT and SA-SF-DFT. The D_{2d} geometry served as the starting point in both calculations, and for SF-TDDFT, we assign the states using $\langle \hat{S}^2 \rangle$ along, with any state having $\langle \hat{S}^2 \rangle < 1.2$ assigned as a singlet. We do not yet have analytic energy gradients for the SA-SF-DFT method, so for this method the gradients are evaluated by finite difference, and we use a penalty-constrained algorithm[63] to locate the MECP. This algorithm does not require derivative couplings. For the SF-TDDFT calculations, both analytic gradients and analytic derivative couplings are

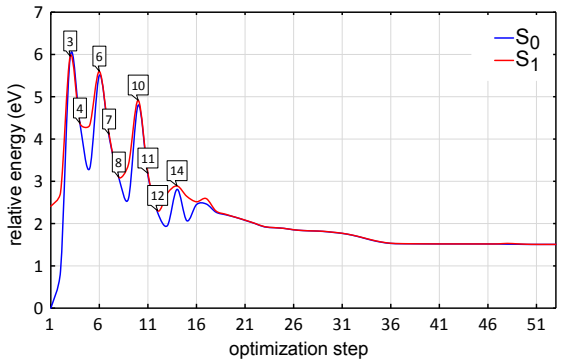

Figure 5.3: Potential energy curves along the S_0/S_1 MECP optimization trajectory of ethylene, calculated using collinear SF-TDDFT (BH&HLYP/6-31G* level). Labels above the curves show at which steps the state assignment problem appears. The zero of energy is the ground state at the D_{2d} geometry.

available,[14] and we can use a MECP optimization algorithm that takes advantage of both.[13]

Figure 5.3 plots the energies of the two states involved in the MECP optimization, at the SF-TDDFT level. Optimization steps at which the state assignment is ambiguous are labeled, and in Table 5.3 we provide the $\langle \hat{S}^2 \rangle$ values of the lowest three states at each optimization step. For the first 14 optimization steps, the S_0 state and the low-lying triplet state are nearly degenerate and strongly coupled with each other, which makes state assignments very difficult. For example, whereas in the second step we can assign state 1 as S_0 and state 3 as S_1 without ambiguity, the use of $\langle \hat{S}^2 \rangle$ in the third step would assign state 1 as S_0 and state 2 as S_1, but by examining the orbitals and CI coefficients we found that state 2 and state 3 are the true S_0 and S_1 states, whereas state 1 is a triplet. As a result of this incorrect state

Table 5.3: Values of $\langle \hat{S}^2 \rangle$ (in units of $\hbar^2$) for the lowest three states of ethylene in the first 19 optimization steps shown in Fig. 5.3.

step	values of $\langle \hat{S}^2 \rangle$		
	state 1	state 2	state 3
1	0.01	2.01	0.06
2	0.02	2.00	0.05
3	1.14	0.90	0.02
4	1.10	0.95	0.02
5	0.07	1.97	0.03
6	0.90	1.18	0.03
7	0.93	1.15	0.05
8	1.00	1.05	0.06
9	0.75	1.30	0.05
10	1.03	1.06	0.04
11	0.93	1.14	0.06
12	0.99	1.06	0.08
13	1.61	0.43	0.09
14	1.20	0.85	0.09
15	0.29	1.76	0.08
16	0.27	1.81	0.05
17	0.12	2.01	0.02
18	2.00	0.10	0.04
19	2.00	0.03	0.10

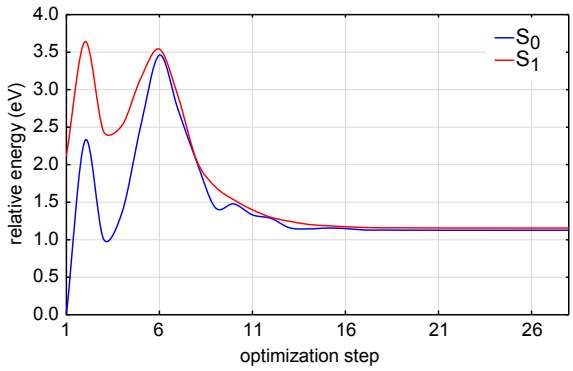

Figure 5.4: Potential energy curves along the S_0/S_1 MECP optimization trajectory of ethylene, calculated using SA-SF-DFT (BH&HLYP/6-31G* level). The zero of energy is the ground state at the D_{2d} geometry.

assignment, the efficiency of MECP optimization is greatly reduced, which can be inferred from the steep peaks in Fig. 5.3 that occur precisely in regions where the state assignment is ambiguous. Since the states are assigned incorrectly, the energy gradients and derivative couplings are calculated for the wrong states, and it takes 18 steps to reach the correct intersection seam.

Although a state-tracking algorithm, such as those discussed above, might improve the performance of SF-TDDFT for MECP optimization, the SA-SF-DFT method is a better solution. Energies along the S_0/S_1 MECP optimization computed using the latter method are plotted in Fig. 5.4. In this case, the energy variations along the optimization pathway are much smaller and the optimization reaches the correct intersection seam within 6 steps, and finally converges to the MECP in fewer steps than the SF-TDDFT calculation, despite the fact that the latter calculation is able to exploit analytic derivative couplings. (MECP optimizations using SF-TDDFT

without analytic derivative couplings require even more steps.[14])

5.4 Summary

We have derived and implemented the spin-adapted counterpart of conventional collinear SF-TDDFT, which we denote as SA-SF-DFT. The underlying SA-SF-CIS method is equivalent to a previous spin-complete implementation of SF-CIS,[3] but is derived here based on an equation-of-motion formulation in a spin-tensor basis. Our derivation results in matrices of similar dimension as those in SF-TDDFT, meaning that the cost of the CI-like part of the SA-SF-CIS calculation is not significantly increased by the extension to spin eigenstates. To this SA-SF-CIS foundation, we then add an *ad hoc* density-functional correction in order to incorporate dynamical correlation, and this constitutes what we call the SA-SF-DFT method. Roughly speaking, SA-SF-DFT is a spin-flip restricted active space CI method with a DFT correction similar in spirit to that used in DFT/MRCI. Unsurprisingly, this dynamical correlation correction can easily exceed 1 eV for excitation energies, and we find that the performance of SA-SF-DFT represents a consistent improvement over collinear SF-TDDFT.

In addition, SA-SF-DFT is a potentially much more attractive approach to excited-state *ab initio* MD simulations, as compared to SF-TDDFT. This is because:

- it is free of spin contamination, and thus not subject to the state-assignment problem that plagues SF-TDDFT;

- it treats ground and excited states on the same footing and thus affords correct topology at conical intersections, including those that involve the ground state; and

- it is just as computationally efficient as SF-TDDFT.

That said, efficient application to *ab initio* MD will require the development an implementation of analytic energy gradients for the SA-SF-DFT method. Relative to the gradients for traditional SF-TDDFT, this is complicated by the additional orbital subspaces that are necessary for the spin-adapted version (as illustrated in Fig. 5.1), and thus by additional orbital response terms that will appear in the derivative of Eq. (5.18). These extra terms should, however, only increase the cost relative to SF-TDDFT by a prefactor that is independent of system size, and thus will should not increase the formal computational scaling with system size relative to TDDFT or SF-TDDFT.

CHAPTER 6

Conclusion

In this work we have demonstrated that SF-TDDFT is an efficient and qualitatively correct first-principle method to study nonadiabatic photodynamics. We formulated the analytic derivative coupling for LR-TDDFT in chapter 2, and further extended it to the spin-flip version in chapter 3. With these couplings, we are able to carry out efficient conical intersection optimizations as well as nonadiabatic AIMD simulations. As an example, we studied the radiationless deactivation of the photo-excited uracil molecule in both gas phase and aqueous solution, where we located the key conical intersections along the relaxation pathways and illuminated the deactivation mechanisms. In order to cure the spin contamination problem in conventional SF-TDDFT, we developed a spin-adapted version of SF-TDDFT based on an tensor equation-of-motion formalism. Our preliminary calculations show that SA-SF-DFT may be a potentially much more attractive approach for excited-state AIMD simulations, as compared to SF-TDDFT. Future studies involve the development of energy gradients and derivative couplings for SA-SF-DFT.

Bibliography

[1] P. M. Hare, C. E. Crespo-Hernández, and B. Kohler, J. Phys. Chem. B **110**, 18641 (2006).

[2] M. Barbatti and H. Lischka, J. Am. Chem. Soc. **130**, 6831 (2008).

[3] J. S. Sears, C. D. Sherrill, and A. I. Krylov, J. Chem. Phys. **118**, 9084 (2003).

[4] M. Barbatti, J. Paier, and H. Lischka, J. Chem. Phys. **121**, 11614 (2004).

[5] C. J. Ballhausen and A. E. Hansen, Annu. Rev. Phys. Chem. **23**, 15 (1972).

[6] J. C. Tully, J. Chem. Phys. **137**, 22A301 (2012).

[7] J. C. Tully, J. Chem. Phys. **93**, 1061 (1990).

[8] D. R. Yarkony, Rev. Mod. Phys. **68**, 985 (1996).

[9] M. E. Casida, Time-dependent density functional response theory for molecules, in *Recent Advances in Density Functional Methods, Part I*, edited by D. P. Chong, volume I of *Recent Advances in Computational Chemistry*, chapter 5, pages 155–192, World Scientific, River Edge, NJ, 1995.

[10] B. G. Levine, C. Ko, J. Quenneville, and T. J. Martínez, Mol. Phys. **104**, 1039 (2006).

[11] Y. Shao, M. Head-Gordon, and A. I. Krylov, J. Chem. Phys. **118**, 4807 (2003).

[12] F. Wang and T. Ziegler, J. Chem. Phys. **121**, 12191:1 (2004).

[13] M. J. Bearpark, M. A. Robb, and H. B. Schlegel, Chem. Phys. Lett. **223**, 269 (1994).

[14] X. Zhang and J. M. Herbert, J. Chem. Phys. **141**, 064104:1 (2014).

[15] B. H. Lengsfield III, P. Saxe, and D. R. Yarkony, J. Chem. Phys. **81**, 4549 (1984).

[16] P. Saxe, B. H. Lengsfield III, and D. R. Yarkony, Chem. Phys. Lett. **113**, 159 (1985).

[17] B. H. Lengsfield III and D. R. Yarkony, J. Chem. Phys. **84**, 348 (1986).

[18] H. Lischka, M. Dallos, P. G. Szalay, D. R. Yarkony, and R. Shepard, J. Chem. Phys. **120**, 7322 (2004).

[19] T. Ichino, J. Gauss, and J. F. Stanton, J. Chem. Phys. **130**, 174105:1 (2009).

[20] A. Tajti and P. G. Szalay, J. Chem. Phys. **131**, 124104:1 (2009).

[21] S. Fatehi, E. Alguire, Y. Shao, and J. E. Subotnik, J. Chem. Phys. **135**, 234105:1 (2011).

[22] F. Furche, J. Chem. Phys. **114**, 5982 (2001).

[23] V. Chernyak and S. Mukamel, J. Chem. Phys. **112**, 3572 (2000).

[24] R. Send and F. Furche, J. Chem. Phys. **132**, 044107:1 (2010).

[25] I. Tavernelli, B. F. E. Curchod, A. Laktionov, and U. Rothlisberger, J. Chem. Phys. **133**, 194104:1 (2010).

[26] Z. Li and W. Liu, J. Chem. Phys. **141**, 014110:1 (2014).

[27] C. Hu, O. Sugino, and K. Watanabe, J. Chem. Phys. **140**, 054106:1 (2014).

[28] Q. Ou, S. Fatehi, E. Alguire, Y. Shao, and J. E. Subotnik, J. Chem. Phys. **141**, 024114:1 (2014).

[29] Q. Ou, E. C. Alguire, and J. E. Subotnik, J. Phys. Chem. B **119**, 7150 (2015), DOI: 0.1021/jp5057682.

[30] J. Olsen and P. Jørgensen, J. Chem. Phys. **82**, 3235 (1985).

[31] E. Gross and W. Kohn, Adv. Quantum Chem. **21**, 255 (1990).

[32] F. Furche and R. Ahlrichs, J. Chem. Phys. **117**, 7433 (2002).

[33] Y. Shao et al., Mol. Phys. **113**, 184 (2015).

[34] E. C. Alguire, Q. Ou, and J. E. Subotnik, J. Phys. Chem. B **119**, 7140 (2015), DOI: 10.1021/jp505767b.

[35] S. Hirata and M. Head-Gordon, Chem. Phys. Lett. **314**, 291 (1999).

[36] H. Werner and P. J. Knowles, J. Chem. Phys. **82**, 5053 (1985).

[37] H. Werner and P. J. Knowles, Chem. Phys. Lett. **115**, 259 (1985).

[38] H.-J. Werner, P. J. Knowles, G. Knizia, F. R. Manby, and M. Schütz, WIREs Comput. Mol. Sci. **2**, 242 (2012).

[39] C. Adamo and V. Barone, J. Chem. Phys. **110**, 6158 (1999).

[40] A. D. Becke, J. Chem. Phys. **98**, 5648 (1993).

[41] C. Lee, W. Yang, and R. G. Parr, Phys. Rev. B **37**, 785 (1988).

[42] E. Tapavicza, G. D. Bellchambers, J. C. Vincent, and F. Furche, Phys. Chem. Chem. Phys. **15**, 18336 (2013).

[43] S. Yang and T. J. Martínez, *Ab initio* multiple spawning: First principles dynamics around conical intersections, in *Conical Intersections: Theory, Computation, and Experiment*, edited by W. Domcke, D. R. Yarkony, and H. Köppel, volume 17 of *Advanced Series in Physical Chemistry*, pages 347–374, World Scientific, 2011.

[44] A. I. Krylov, Chem. Phys. Lett. **338**, 375 (2001).

[45] N. Minezawa and M. S. Gordon, J. Phys. Chem. A **113**, 12749 (2009).

[46] N. Minezawa and M. S. Gordon, J. Phys. Chem. A **115**, 7901 (2011).

[47] N. Minezawa and M. S. Gordon, J. Chem. Phys. **137**, 034116:1 (2012).

[48] Y. Harabuchi, S. Maeda, T. Taketsugu, N. Minezawa, and K. Morokuma, J. Chem. Theory Comput. **9**, 4116 (2013).

[49] X. Zhang and J. M. Herbert, J. Phys. Chem. B **118**, 7806 (2014).

[50] Y. Yamaguchi, Y. Osamura, J. D. Goddard, and H. F. Schaefer III, *A New Dimension to Quantum Chemistry: Analytic Derivative Methods in Ab Initio Molecular Electronic Structure Theory*, Oxford University Press, New York, 1994.

[51] D. Maurice and M. Head-Gordon, Int. J. Quantum Chem. Symp. **29**, 361 (1995).

[52] J. A. Pople, R. Krishnan, H. B. Schegel, and J. S. Binkley, Int. J. Quantum Chem. Symp. **13**, 225 (1979).

[53] J. B. Foresman, M. Head-Gordon, J. A. Pople, and M. J. Frisch, J. Phys. Chem. **96**, 135 (1992).

[54] R. M. Shroll and W. D. Edwards, Int. J. Quantum Chem. **56**, 395 (1995).

[55] J. B. Delos, Rev. Mod. Phys. **53**, 287 (1981).

[56] D. R. Yarkony, J. Chem. Phys. **84**, 3206 (1986).

[57] W. Kutzelnigg, Mol. Phys. **105**, 2627 (2007).

[58] S. Fatehi and J. E. Subotnik, J. Phys. Chem. Lett. **3**, 2039 (2012).

[59] M. Huix-Rotllant et al., Phys. Chem. Chem. Phys. **12**, 12811 (2010).

[60] S. Gozem et al., J. Chem. Theory Comput. **10**, 3074 (2014).

[61] A. D. Becke, Phys. Rev. A **38**, 3098 (1988).

[62] S. Maeda, K. Ohno, and K. Morokuma, J. Chem. Theory Comput. **6**, 1538 (2010).

[63] B. G. Levine, J. D. Coe, and T. J. Martínez, J. Phys. Chem. B **112**, 405 (2008).

[64] D. Casanova and M. Head-Gordon, J. Chem. Phys. **129**, 064104 (2008).

[65] Z. Li, W. Liu, Y. Zhang, and B. Suo, J. Chem. Phys. **134**, 134101:1 (2011).

[66] Y. A. Bernard, Y. Shao, and A. I. Krylov, J. Chem. Phys. **136**, 204103:1 (2012).

[67] C. E. Crespo-Hernández, B. Cohen, P. M. Hare, and B. Kohler, Chem. Rev. **104**, 1977 (2004).

[68] C. T. Middleton et al., Annu. Rev. Phys. Chem. **60**, 217 (2009).

[69] Y. He, C. Wu, and W. Kong, J. Phys. Chem. A **108**, 943 (2004).

[70] H. Kang, K. T. Lee, B. Jung, Y. J. Ko, and S. S. Kim, J. Am. Chem. Soc. **124**, 12958 (2002).

[71] S. Ullrich, T. Schultz, M. Z. Zgierski, and A. Stolow, Phys. Chem. Chem. Phys. **6**, 2796 (2004).

[72] S. Matsika, J. Phys. Chem. A **108**, 7584 (2004).

[73] E. Epifanovsky et al., J. Phys. Chem. A **112**, 9983 (2008).

[74] Y. Mercier, F. Santoro, M. Reguero, and R. Improta, J. Phys. Chem. B **112**, 10769 (2008).

[75] M. Merchán, L. Serrano-Andrés, M. A. Robb, and L. Blancafort, J. Am. Chem. Soc. **127**, 1820 (2005).

[76] H. R. Hudock et al., J. Phys. Chem. A **111**, 8500 (2007).

[77] D. Nachtigallová et al., J. Phys. Chem. A **115**, 5247 (2011).

[78] T. Zelený et al., J. Am. Chem. Soc. **134**, 13662 (2012).

[79] R. Improta, V. Barone, A. Lami, and F. Santoro, J. Phys. Chem. B **113**, 14491 (2009).

[80] W. T. Borden and E. R. Davidson, Acc. Chem. Res. **29**, 67 (1996).

[81] Y. He, C. Wu, and W. Kong, J. Phys. Chem. A **107**, 5145 (2003).

[82] P. M. Hare, C. E. Crespo-Hernández, and B. Kohler, Proc. Natl. Acad. Sci. USA **104**, 435 (2007).

[83] F. Santoro, V. Barone, T. Gustavsson, and R. Improta, J. Am. Chem. Soc. **128**, 16312 (2006).

[84] T. Gustavsson et al., J. Phys. Chem. B **110**, 12843 (2006).

[85] T. Gustavsson et al., J. Am. Chem. Soc. **128**, 607 (2006).

[86] C. Salet, R. Bensasson, and R. S. Becker, Photochem. Photobiol. **30**, 325 (1979).

[87] F. Sicilia, L. Blancafort, M. J. Bearpark, and M. A. Robb, J. Chem. Theory Comput. **4**, 257 (2008).

[88] A. W. Lange and J. M. Herbert, J. Phys. Chem. Lett. **1**, 556 (2010).

[89] A. W. Lange and J. M. Herbert, J. Chem. Phys. **133**, 244111:1 (2010).

[90] B. Peters, A. Heyden, A. T. Bell, and A. Chakraborty, J. Chem. Phys. **120**, 7877 (2004).

[91] A. Behn, P. M. Zimmerman, A. T. Bell, and M. Head-Gordon, J. Chem. Phys. **135**, 224108:1 (2011).

[92] M. A. Rohrdanz, K. M. Martins, and J. M. Herbert, J. Chem. Phys. **130**, 054112:1 (2009).

[93] TURBOMOLE v. 6.3.1, a development of University of Karlsruhe and Forschungszentrum Karlsruhe GmbH, 1989–2007, TURBOMOLE GmbH, since 2007; available from `http://www.turbomole.com`.

[94] R. Taylor and O. Kennard, J. Mol. Struct. **78**, 1 (1982).

[95] T. Fleig, S. Knecht, and C. Hättig, J. Phys. Chem. A **111**, 5482 (2007).

[96] K. A. Kistler and S. Matsika, J. Am. Chem. Soc. **113**, 12396 (2009).

[97] A. DeFusco, J. Ivanic, M. W. Schmidt, and M. S. Gordon, J. Phys. Chem. A **115**, 4574 (2011).

[98] J. M. Olsen, K. Aidas, K. V. Mikkelsen, and J. Kongsted, J. Chem. Theory Comput. **6**, 249 (2009).

[99] M. Etinski and C. M. Marian, Phys. Chem. Chem. Phys. **12**, 4915 (2010).

[100] M. Merchán, R. González-Luque, T. Climent, and L. Serrano-Andrés, J. Phys. Chem. B **110**, 26471 (2006).

[101] Z. Li and W. Liu, J. Chem. Phys. **133**, 064106:1 (2010).

[102] D. J. Rowe and C. Ngo-Trong, Rev. Mod. Phys. **47**, 471 (1975).

[103] F. Wang and T. Ziegler, J. Chem. Phys. **122**, 074109:1 (2005).

[104] K. Yang, R. Peverati, D. G. Truhlar, and R. Valero, J. Chem. Phys. **135**, 044118 (2011).

[105] X. Xu, K. R. Yang, and D. G. Truhlar, J. Chem. Theory Comput. **10**, 2070 (2014).

[106] N. Minezawa, Chem. Phys. Lett. **622**, 115 (2015).

[107] X. Zhang and J. M. Herbert, J. Chem. Phys. **142**, 064109:1 (2015).

[108] X. Xu, S. Gozem, M. Olivucci, and D. G. Truhlar, J. Phys. Chem. Lett. **4**, 253 (2013).

[109] N. Minezawa, J. Chem. Phys. **141**, 164118:1 (2014).

[110] P. Zhou, J. Liu, K. Han, and G. He, J. Comput. Chem. **35**, 109 (2014).

[111] M. Isegawa and K. Morokuma, J. Phys. Chem. A **119**, 4191 (2015).

[112] Y. Harabuchi, K. Keipert, F. Zahariev, T. Taketsugu, and M. S. Gordon, J. Phys. Chem. A **118**, 11987 (2014).

[113] L. Yue, Z. Lan, and Y.-J. Liu, J. Phys. Chem. Lett. **6**, 540 (2014).

[114] O. Vahtras and Z. Rinkevicius, J. Chem. Phys. **126**, 114101:1 (2007).

[115] Z. Li and W. Liu, J. Chem. Phys. **135**, 194106 (2011).

[116] T. Tsuchimochi and T. Van Voorhis, J. Chem. Phys. **142**, 124103:1 (2015).

[117] T. Tsuchimochi, J. Chem. Phys. **143**, 144114:1 (2015).

[118] S. Grimme, Chem. Phys. Lett. **259**, 128 (1996).

[119] S. Grimme and M. Waletzke, J. Chem. Phys. **111**, 5645 (1999).

[120] D. J. Rowe, Rev. Mod. Phys. **40**, 153 (1968).

[121] T. Helgaker, P. Jørgensen, and J. Olsen, *Molecular Electronic-Structure Theory*, Wiley, New York, 2000.

[122] Z. Szekeres, Á. Szabados, M. Kállaya, and P. R. Surján, Phys. Chem. Chem. Phys. **3**, 696 (2001).

[123] $E_{xc}^{\mathrm{BH\&HLYP}} = 0.5E_x^{\mathrm{B88}} + 0.5E_x^{\mathrm{HF}} + E_c^{\mathrm{LYP}}$.

[124] F. Neese, WIREs Comput. Mol. Sci. **2**, 73 (2011).

[125] M. P. Fülscher, L. Serrano-Andrés, and B. O. Roos, J. Am. Chem. Soc. **119**, 6168 (1997).

[126] M. Schreiber, M. R. Silva-Junior, S. P. A. Sauer, and W. Thiel, J. Chem. Phys. **128**, 134110 (2008).

[127] M. Valiev and K. Kowalski, J. Chem. Phys. **125**, 211101 (2006).

[128] M. E. Foster and B. M. Wong, J. Chem. Theory Comput. **8**, 2682 (2012).

[129] D. Casanova and M. Head-Gordon, Phys. Chem. Chem. Phys. **11**, 9779 (2009).

[130] F. Liu et al., Mol. Phys. **108**, 2791 (2010).

APPENDIX A

Supporting information for "Analytic Derivative Couplings of LR-TDDFT: Quadratic Response Theory versus Pseudo-Wavefunction Approach"

A.1 VO and OV blocks of the transition density matrix between TDDFT excited states

In Eq. (2.18), the matrix elements of $\mathbf{R}^{(\alpha\beta)}$ and $\mathbf{S}^{(\alpha\beta)}$ are

$$\begin{aligned} R_{ai}^{(\alpha\beta)} = \hat{\mathcal{P}}(\alpha,\beta) \Bigg[& \sum_{bck} \left(\frac{\partial F_{ab}}{\partial P_{ck}} X_{ck}^{(\alpha)} X_{bi}^{(\beta)} + \frac{\partial F_{ab}}{\partial P_{kc}} Y_{ck}^{(\alpha)} X_{bi}^{(\beta)} \right) \\ & - \sum_{jck} \left(X_{aj}^{(\beta)} \frac{\partial F_{ji}}{\partial P_{ck}} X_{ck}^{(\alpha)} + X_{aj}^{(\beta)} \frac{\partial F_{ji}}{\partial P_{kc}} Y_{ck}^{(\alpha)} \right) \\ & + \frac{1}{2} \sum_{bjb'j'} \frac{\partial^2 F_{ai}}{\partial P_{bj} \partial P_{b'j'}} \left(X_{bj}^{(\alpha)} + Y_{bj}^{(\alpha)} \right) \left(X_{b'j'}^{(\beta)} + Y_{b'j'}^{(\beta)} \right) \Bigg] \end{aligned} \tag{A.1}$$

and

$$\begin{aligned} S_{ai}^{(\alpha\beta)} = \hat{\mathcal{P}}(\alpha,\beta) \Bigg[& - \sum_{jck} \left(\frac{\partial F_{ij}}{\partial P_{ck}} X_{ck}^{(\alpha)} Y_{aj}^{(\beta)} + \frac{\partial F_{ij}}{\partial P_{kc}} Y_{ck}^{(\alpha)} Y_{aj}^{(\beta)} \right) \\ & + \sum_{bck} \left(Y_{bi}^{(\beta)} \frac{\partial F_{ba}}{\partial P_{ck}} X_{ck}^{(\alpha)} + Y_{bi}^{(\beta)} \frac{\partial F_{ba}}{\partial P_{kc}} Y_{ck}^{(\alpha)} \right) \\ & + \frac{1}{2} \sum_{bjb'j'} \frac{\partial^2 F_{ia}}{\partial P_{bj} \partial P_{b'j'}} \left(X_{bj}^{(\alpha)} + Y_{bj}^{(\alpha)} \right) \left(X_{b'j'}^{(\beta)} + Y_{b'j'}^{(\beta)} \right) \Bigg] , \end{aligned} \tag{A.2}$$

where $\mathbf{F}$ is the Fock matrix and $\mathbf{P}$ is the ground state density matrix. Derivatives of $\mathbf{F}$ with respect to $\mathbf{P}$ have matrix elements

$$\begin{aligned}\frac{\partial F_{pq}}{\partial P_{rs}} &= \langle\phi_p\phi_s|\phi_q\phi_r\rangle - C_{\mathrm{HF}}\langle\phi_p\phi_s|\phi_r\phi_q\rangle \\ &\quad + \langle\phi_p\phi_s|f^{\mathrm{xc}}|\phi_q\phi_r\rangle\end{aligned} \tag{A.3}$$

and

$$\begin{aligned}\frac{\partial^2 F_{ai}}{\partial P_{bj}\partial P_{b'j'}} &= \iiint d\mathbf{r}\, d\mathbf{r}'\, d\mathbf{r}''\frac{\delta^3 E_{\mathrm{xc}}[\rho]}{\delta\rho(\mathbf{r})\rho(\mathbf{r}')\rho(\mathbf{r}'')} \\ &\quad \times \phi_a(\mathbf{r})\phi_i(\mathbf{r})\phi_b(\mathbf{r}')\phi_j(\mathbf{r}')\phi_{b'}(\mathbf{r}'')\phi_{j'}(\mathbf{r}'')\ .\end{aligned} \tag{A.4}$$

From Eqs. (2.18), (2.26), (2.27), (A.1) and (A.2), it is straightforward to obtain

$$\begin{aligned}&\frac{\lim\limits_{\omega_\alpha\to-\omega_I}(\omega_\alpha+\omega_I)\lim\limits_{\omega_\beta\to\omega_J}(\omega_\beta-\omega_J)\big|\mathbf{X}^{(\alpha\beta)},\mathbf{Y}^{(\alpha\beta)}\big\rangle}{\langle 0|V^{-\omega_I}|I\rangle\langle J|V^{\omega_J}|0\rangle} \\ &= [\mathbf{\Lambda}-(\omega_J-\omega_I)\mathbf{\Delta}]^{-1}\big|\mathbf{R}^{IJ},\mathbf{S}^{IJ}\big\rangle\ ,\end{aligned} \tag{A.5}$$

where the matrix elements of $\mathbf{R}^{IJ}$ and $\mathbf{S}^{IJ}$ are

$$\begin{aligned}R_{ai}^{IJ} &= \sum_{bck}\Bigg[\frac{\partial F_{ab}}{\partial P_{ck}}\big(Y_{ck}^I X_{bi}^J + X_{ck}^J Y_{bi}^I\big) \\ &\qquad + \frac{\partial F_{ab}}{\partial P_{kc}}\big(X_{ck}^I X_{bi}^J + Y_{ck}^J Y_{bi}^I\big)\Bigg] \\ &\quad - \sum_{jck}\Bigg[\frac{\partial F_{ji}}{\partial P_{ck}}\big(Y_{ck}^I X_{aj}^J + X_{ck}^J Y_{aj}^I\big) \\ &\qquad + \frac{\partial F_{ji}}{\partial P_{kc}}\big(X_{ck}^I X_{aj}^J + Y_{ck}^J Y_{aj}^I\big)\Bigg] \\ &\quad + \sum_{bjb'j'}\frac{\partial^2 F_{ai}}{\partial P_{bj}\partial P_{b'j'}}\big(X_{bj}^I + Y_{bj}^I\big)\big(X_{b'j'}^J + Y_{b'j'}^J\big)\end{aligned} \tag{A.6}$$

and

$$
\begin{aligned}
S_{ai}^{IJ} = & \sum_{bck} \Big[\frac{\partial F_{ba}}{\partial P_{kc}} \big(Y_{ck}^{J} X_{bi}^{I} + X_{ck}^{I} Y_{bi}^{J} \big) \\
& \qquad + \frac{\partial F_{ba}}{\partial P_{ck}} \big(X_{ck}^{J} X_{bi}^{I} + Y_{ck}^{I} Y_{bi}^{J} \big) \Big] \\
& - \sum_{jck} \Big[\frac{\partial F_{ij}}{\partial P_{kc}} \big(Y_{ck}^{J} X_{aj}^{I} + X_{ck}^{I} Y_{aj}^{J} \big) \\
& \qquad + \frac{\partial F_{ij}}{\partial P_{ck}} \big(X_{ck}^{J} X_{aj}^{I} + Y_{ck}^{I} Y_{aj}^{J} \big) \Big] \\
& + \sum_{bjb'j'} \frac{\partial^2 F_{ia}}{\partial P_{bj} \partial P_{b'j'}} \big(X_{bj}^{I} + Y_{bj}^{I} \big) \big(X_{b'j'}^{J} + Y_{b'j'}^{J} \big) \; .
\end{aligned}
\tag{A.7}
$$

By comparing to exact response theory,[30] one discovers that the right side of Eq. (A.5) constitutes the VO and OV blocks of the transition density matrix between two TDDFT excited states $|I\rangle$ and $|J\rangle$. We can define these blocks of the transition density matrix as

$$
|\mathbf{X}_{IJ}, \mathbf{Y}_{IJ}\rangle \equiv -[\mathbf{\Lambda} - (\omega_J - \omega_I)\mathbf{\Delta}]^{-1} |\mathbf{R}^{IJ}, \mathbf{S}^{IJ}\rangle \; . \tag{A.8}
$$

Then $|\mathbf{X}_{IJ}, \mathbf{Y}_{IJ}\rangle$ is the solution of the following linear equations:

$$
\big(\mathbf{\Lambda} - (\omega_J - \omega_I)\mathbf{\Delta}\big) |\mathbf{X}_{IJ}, \mathbf{Y}_{IJ}\rangle = -|\mathbf{R}^{IJ}, \mathbf{S}^{IJ}\rangle \; . \tag{A.9}
$$

A.2 The last term in Eq. (2.28)

We can rewrite the last term in Eq. (2.28) as

$$
\sum_{ai} \big(X_{ai}^{I} \hat{\mathbf{\nabla}}_{\mathbf{R}} X_{ai}^{(\beta)} - Y_{ai}^{I} \hat{\mathbf{\nabla}}_{\mathbf{R}} Y_{ai}^{(\beta)} \big) = \big\langle \mathbf{X}_I, \mathbf{Y}_I \big| \mathbf{\Delta} \big| \hat{\mathbf{\nabla}}_{\mathbf{R}} \mathbf{X}^{(\beta)}, \hat{\mathbf{\nabla}}_{\mathbf{R}} \mathbf{Y}^{(\beta)} \big\rangle \; . \tag{A.10}
$$

Taking the nuclear derivative of Eq. (2.10), we obtain

$$
\begin{aligned}
&(\boldsymbol{\Lambda} - \omega_\beta \boldsymbol{\Delta}) \big| \hat{\boldsymbol{\nabla}}_{\mathbf{R}} \mathbf{X}^{(\beta)}, \hat{\boldsymbol{\nabla}}_{\mathbf{R}} \mathbf{Y}^{(\beta)} \big\rangle \\
&\quad = -\big| \hat{\boldsymbol{\nabla}}_{\mathbf{R}} \mathbf{P}^{(\beta)}, \hat{\boldsymbol{\nabla}}_{\mathbf{R}} \mathbf{Q}^{(\beta)} \big\rangle - (\hat{\boldsymbol{\nabla}}_{\mathbf{R}} \boldsymbol{\Lambda}) \big| \mathbf{X}^{(\beta)}, \mathbf{Y}^{(\beta)} \big\rangle \, .
\end{aligned} \tag{A.11}
$$

Taking the inner product with $\langle \mathbf{X}_I, \mathbf{Y}_I |$ from the left, then we obtain

$$
\begin{aligned}
&\big\langle \mathbf{X}_I, \mathbf{Y}_I \big| (\boldsymbol{\Lambda} - \omega_\beta \boldsymbol{\Delta}) \big| \hat{\boldsymbol{\nabla}}_{\mathbf{R}} \mathbf{X}^{(\beta)}, \hat{\boldsymbol{\nabla}}_{\mathbf{R}} \mathbf{Y}^{(\beta)} \big\rangle \\
&= (\omega_I - \omega_\beta) \big\langle \mathbf{X}_I, \mathbf{Y}_I \big| \boldsymbol{\Delta} \big| \hat{\boldsymbol{\nabla}}_{\mathbf{R}} \mathbf{X}^{(\beta)}, \hat{\boldsymbol{\nabla}}_{\mathbf{R}} \mathbf{Y}^{(\beta)} \big\rangle \\
&= -\big\langle \mathbf{X}_I, \mathbf{Y}_I \big| \hat{\boldsymbol{\nabla}}_{\mathbf{R}} \mathbf{P}^{(\beta)}, \hat{\boldsymbol{\nabla}}_{\mathbf{R}} \mathbf{Q}^{(\beta)} \big\rangle \\
&\quad - \big\langle \mathbf{X}_I, \mathbf{Y}_I \big| (\hat{\boldsymbol{\nabla}}_{\mathbf{R}} \boldsymbol{\Lambda}) \big| \mathbf{X}^{(\beta)}, \mathbf{Y}^{(\beta)} \big\rangle \, .
\end{aligned} \tag{A.12}
$$

From this equation, we know that

$$
\begin{aligned}
&\big\langle \mathbf{X}_I, \mathbf{Y}_I \big| \boldsymbol{\Delta} \big| \hat{\boldsymbol{\nabla}}_{\mathbf{R}} \mathbf{X}^{(\beta)}, \hat{\boldsymbol{\nabla}}_{\mathbf{R}} \mathbf{Y}^{(\beta)} \big\rangle \\
&= (\omega_\beta - \omega_I)^{-1} \Big[\big\langle \mathbf{X}_I, \mathbf{Y}_I \big| \hat{\boldsymbol{\nabla}}_{\mathbf{R}} \mathbf{P}^{(\beta)}, \hat{\boldsymbol{\nabla}}_{\mathbf{R}} \mathbf{Q}^{(\beta)} \big\rangle \\
&\qquad + \big\langle \mathbf{X}_I, \mathbf{Y}_I \big| (\hat{\boldsymbol{\nabla}}_{\mathbf{R}} \boldsymbol{\Lambda}) \big| \mathbf{X}^{(\beta)}, \mathbf{Y}^{(\beta)} \big\rangle \Big] \, .
\end{aligned} \tag{A.13}
$$

After taking the residue of Eq. (A.13), we obtain the final result:

$$
\begin{aligned}
&\sum_{ai} \frac{\lim\limits_{\omega_\beta \to \omega_J} (\omega_\beta - \omega_J) \big(X^I_{ai} \hat{\boldsymbol{\nabla}}_{\mathbf{R}} X^{(\beta)}_{ai} - Y^I_{ai} \hat{\boldsymbol{\nabla}}_{\mathbf{R}} Y^{(\beta)}_{ai} \big)}{\langle J | V^{\omega_J} | 0 \rangle} \\
&= (\omega_J - \omega_I)^{-1} \big\langle \mathbf{X}_I, \mathbf{Y}_I \big| (\hat{\boldsymbol{\nabla}}_{\mathbf{R}} \boldsymbol{\Lambda}) \big| \mathbf{X}_J, \mathbf{Y}_J \big\rangle \, .
\end{aligned} \tag{A.14}
$$

APPENDIX B

Supporting information for "Analytic Derivative Couplings of SF-TDDFT"

B.1 Derivation of h_x^{IJ} for SF-CIS

Following the formalism of the CIS analytic energy gradient,[53,54] the nonadiabatic coupling vector h_x^{IJ} in Eq. (3.28) can be expressed as

$$\begin{aligned} h_x^{IJ} &= \sum_{ijab} t_{ai}^I A_{ai,bj}^{[x]} t_{bj}^J \\ &= \sum_{ijab} t_{ai}^I \left(F_{ab}^{[x]} \delta_{ij} - F_{ij}^{[x]} \delta_{ab} + \langle aj||ib\rangle^{[x]} \right) t_{bj}^J \ , \end{aligned} \tag{B.1}$$

where F_{ij} and F_{ab} are Fock matrix elements. Hereafter, we will use matrix notation for simplicity.[130] Matrix elements of the Fock operator are

$$F_{\mu\nu} = \langle \mu | \hat{f} | \nu \rangle \tag{B.2}$$

and its one-electron part is

$$H_{\mu\nu} = \langle \mu | \hat{h} | \nu \rangle \ , \tag{B.3}$$

whereas two-electron integrals are denoted

$$\Pi_{\mu\nu,\lambda\sigma} = \langle \mu\lambda || \nu\sigma \rangle \ . \tag{B.4}$$

The overlap matrix is

$$S_{\mu\nu} = \langle \mu | \nu \rangle \tag{B.5}$$

and

$$P_{\mu\nu} = \sum_{k}^{\text{occ}} C_{\mu k} C_{\nu k} \tag{B.6}$$

is the one-electron density matrix. The difference density matrix for the excited state is

$$\begin{aligned} \mathbf{P}^{\Delta} = {} & \tfrac{1}{2}\mathbf{C}_{\text{v}}\big(\mathbf{t}^{I}\mathbf{t}^{J\dagger} + \mathbf{t}^{J}\mathbf{t}^{I\dagger}\big)\mathbf{C}_{\text{v}}^{\dagger} \\ & - \tfrac{1}{2}\mathbf{C}_{\text{o}}\big(\mathbf{t}^{I\dagger}\mathbf{t}^{J} + \mathbf{t}^{J\dagger}\mathbf{t}^{I}\big)\mathbf{C}_{\text{o}}^{\dagger} \, , \end{aligned} \tag{B.7}$$

where $\mathbf{C}_{\text{o}}$ and $\mathbf{C}_{\text{v}}$ are rectangular matrices containing the occupied and virtual MO coefficients, respectively.

Next, define

$$\mathbf{R}^{I} = \mathbf{C}_{\text{v}}\mathbf{t}^{I}\mathbf{C}_{\text{o}}^{\dagger} \tag{B.8}$$

for state I, with a similar quantity $\mathbf{R}^{J}$ for state J, and

$$\mathbf{P}^{z} = \mathbf{C}_{\text{v}}\mathbf{Z}\mathbf{C}_{\text{o}}^{\dagger} + \mathbf{C}_{\text{o}}\mathbf{Z}^{\dagger}\mathbf{C}_{\text{v}}^{\dagger} \, . \tag{B.9}$$

The quantity $\mathbf{Z}$ in Eq. (B.9) represents the solution to the well-known coupled-perturbed equations,[52] which are

$$\begin{aligned} & \mathbf{C}_{\text{v}}^{\dagger}\mathbf{F}\mathbf{C}_{\text{v}}\mathbf{Z} - \mathbf{Z}\mathbf{C}_{\text{o}}^{\dagger}\mathbf{F}\mathbf{C}_{\text{o}} + \mathbf{C}_{\text{v}}(\boldsymbol{\Pi}\cdot\mathbf{P}^{z})\mathbf{C}_{\text{o}} \\ & = -\mathbf{C}_{\text{v}}^{\dagger}(\boldsymbol{\Pi}\cdot\mathbf{P}^{\Delta})\mathbf{C}_{\text{o}} \\ & \quad - \tfrac{1}{2}\mathbf{C}_{\text{v}}^{\dagger}(\boldsymbol{\Pi}'\cdot\mathbf{R}^{I\dagger})\mathbf{C}_{\text{v}}\mathbf{t}^{J} - \tfrac{1}{2}\mathbf{C}_{\text{v}}^{\dagger}(\boldsymbol{\Pi}'\cdot\mathbf{R}^{J\dagger})\mathbf{C}_{\text{v}}\mathbf{t}^{I} \\ & \quad + \tfrac{1}{2}\mathbf{t}^{J}\mathbf{C}_{\text{o}}^{\dagger}(\boldsymbol{\Pi}'\cdot\mathbf{R}^{I\dagger})\mathbf{C}_{\text{o}} + \tfrac{1}{2}\mathbf{t}^{I}\mathbf{C}_{\text{o}}^{\dagger}(\boldsymbol{\Pi}'\cdot\mathbf{R}^{J\dagger})\mathbf{C}_{\text{o}} \, . \end{aligned} \tag{B.10}$$

(The prime in $\mathbf{\Pi}'$ indicates that the Coulomb contribution to the electron repulsion integrals vanishes in SF-CIS, due to $\alpha \rightarrow \beta$ excitation.)

Equation (B.10) contains transition amplitudes for both electronic states, but for $I = J$ it is equivalent to the usual coupled-perturbed equations that must be solved to obtain the relaxed density $\mathbf{P}^{\Delta} + \mathbf{P}^{z}$ and therefore the excited-state CIS analytic gradient.[53,130] Evaluation of the difference gradient $\mathbf{g}^{IJ}$ already requires solution of Eq. (B.10) for both states (*i.e.*, for two different vectors $\mathbf{Z}$), and evaluation of $\mathbf{h}^{IJ}$ requires solution of this equation for a third $\mathbf{Z}$-vector with $I \neq J$ in Eq. (B.10). However, all three $\mathbf{Z}$-vectors can be obtained simultaneously in the same set of Davidson iterations, and in our experience this typically requires only one or two iterations beyond what is required for a CIS gradient evaluation. Relative to the cost of a CIS (or TDDFT) gradient evaluation, the additional cost for derivative couplings is extremely low.

Finally, Eq. (B.1) can be rewritten as

$$h_x^{IJ} = \mathbf{P}' \cdot \mathbf{H}^{[x]} + \mathbf{\Gamma}_1 \cdot \mathbf{\Pi}^{[x]} + \mathbf{\Gamma}_2 \cdot \mathbf{\Pi}'^{[x]} + \mathbf{W}' \cdot \mathbf{S}^{[x]} \tag{B.11}$$

where

$$\mathbf{P}' = \mathbf{P}^{\Delta} + \mathbf{P}^{z} \tag{B.12}$$

$$\mathbf{\Gamma}_1 = \mathbf{P}' \otimes \mathbf{P} \tag{B.13}$$

$$\mathbf{\Gamma}_2 = \mathbf{R}^{I\dagger} \otimes \mathbf{R}^{J} \tag{B.14}$$

$$\mathbf{W}' = -\tfrac{1}{2}\mathbf{\Lambda}'\mathbf{C}\mathbf{C}^{\dagger} - \tfrac{1}{2}\mathbf{C}\mathbf{C}^{\dagger}\mathbf{\Lambda}'^{\dagger} \tag{B.15}$$

$$\begin{aligned}\mathbf{\Lambda}' = {} & \mathbf{P}'\mathbf{F} + \mathbf{P}(\mathbf{\Pi} \cdot \mathbf{P}') \\ & + \tfrac{1}{2}\mathbf{R}^{I}(\mathbf{\Pi}' \cdot \mathbf{R}^{J\dagger}) + \tfrac{1}{2}\mathbf{R}^{J}(\mathbf{\Pi}' \cdot \mathbf{R}^{I\dagger}) \\ & + \tfrac{1}{2}\mathbf{R}^{I\dagger}(\mathbf{\Pi}' \cdot \mathbf{R}^{J}) + \tfrac{1}{2}\mathbf{R}^{J\dagger}(\mathbf{\Pi}' \cdot \mathbf{R}^{I}) \; .\end{aligned} \tag{B.16}$$

B.2 Derivation of h_x^{IJ} for collinear SF-TDDFT

In Ref. 28, the quantity h_x^{IJ} was derived for spin-conserving TDDFT within the TDA, based on an *ad hoc* extension of the CIS formalism. The collinear SF-TDDFT counterpart of this quantity is even simpler because $\langle aj|\hat{\xi}_{\rm xc}|ib\rangle$ vanishes in Eq. (3.29). Thus, h_x^{IJ} for SF-TDDFT is very similar to that in SF-CIS, except that $\mathbf{\Pi}$ is now defined according to

$$\Pi_{\mu\nu,\lambda\sigma} = \langle\mu\lambda|\nu\sigma\rangle - C_{\rm HF}\langle\mu\lambda|\sigma\nu\rangle \; , \tag{B.17}$$

and in addition there are some additional terms arising from the orbital response of the exchange-correlation part of the Kohn-Sham Fock matrix, $\mathbf{F}_{\rm xc}$.

The coupled perturbed equations now read

$$\begin{aligned}
&\mathbf{C}_{\mathrm{v}}^{\dagger}\mathbf{F}\mathbf{C}_{\mathrm{v}}\mathbf{Z} - \mathbf{Z}\mathbf{C}_{\mathrm{o}}^{\dagger}\mathbf{F}\mathbf{C}_{\mathrm{o}} + \mathbf{C}_{\mathrm{v}}(\boldsymbol{\Pi}\cdot\mathbf{P}^{\mathrm{z}} + \boldsymbol{\Omega}\cdot\mathbf{P}^{\mathrm{z}})\mathbf{C}_{\mathrm{o}} \\
&= -\mathbf{C}_{\mathrm{v}}^{\dagger}(\boldsymbol{\Pi}\cdot\mathbf{P}^{\Delta} + \boldsymbol{\Omega}\cdot\mathbf{P}^{\Delta})\mathbf{C}_{\mathrm{o}} \\
&\quad - \tfrac{1}{2}\mathbf{C}_{\mathrm{v}}^{\dagger}(\boldsymbol{\Pi}'\cdot\mathbf{R}^{I\dagger})\mathbf{C}_{\mathrm{v}}\mathbf{t}^{J} - \tfrac{1}{2}\mathbf{C}_{\mathrm{v}}^{\dagger}(\boldsymbol{\Pi}'\cdot\mathbf{R}^{J\dagger})\mathbf{C}_{\mathrm{v}}\mathbf{t}^{I} \\
&\quad + \tfrac{1}{2}\mathbf{t}^{J}\mathbf{C}_{\mathrm{o}}^{\dagger}(\boldsymbol{\Pi}'\cdot\mathbf{R}^{I\dagger})\mathbf{C}_{\mathrm{o}} + \tfrac{1}{2}\mathbf{t}^{I}\mathbf{C}_{\mathrm{o}}^{\dagger}(\boldsymbol{\Pi}'\cdot\mathbf{R}^{J\dagger})\mathbf{C}_{\mathrm{o}}
\end{aligned} \tag{B.18}$$

where

$$\Omega_{\mu\nu,\lambda\sigma} = \frac{\partial F_{\mathrm{xc},\mu\nu}}{\partial P_{\lambda\sigma}} \, . \tag{B.19}$$

The final expression for h_x^{IJ} in collinear SF-TDDFT is

$$h_x^{IJ} = \mathbf{P}'\cdot\mathbf{H}^{[x]} + \boldsymbol{\Gamma}_1\cdot\boldsymbol{\Pi}^{[x]} + \boldsymbol{\Gamma}_2\cdot\boldsymbol{\Pi}'^{[x]} + \mathbf{W}'\cdot\mathbf{S}^{[x]} + \mathbf{P}'\cdot\mathbf{F}_{\mathrm{xc}}^{[x]} \, , \tag{B.20}$$

where

$$\mathbf{W}' = -\tfrac{1}{2}\boldsymbol{\Lambda}'\mathbf{C}\mathbf{C}^{\dagger} - \tfrac{1}{2}\mathbf{C}\mathbf{C}^{\dagger}\boldsymbol{\Lambda}'^{\dagger} \tag{B.21}$$

and

$$\begin{aligned}
\boldsymbol{\Lambda}' &= \mathbf{P}'\mathbf{F} + \mathbf{P}(\boldsymbol{\Pi}\cdot\mathbf{P}' + \boldsymbol{\Omega}\cdot\mathbf{P}') \\
&\quad + \tfrac{1}{2}\mathbf{R}^{I}(\boldsymbol{\Pi}'\cdot\mathbf{R}^{J\dagger}) + \tfrac{1}{2}\mathbf{R}^{J}(\boldsymbol{\Pi}'\cdot\mathbf{R}^{I\dagger}) \\
&\quad + \tfrac{1}{2}\mathbf{R}^{I\dagger}(\boldsymbol{\Pi}'\cdot\mathbf{R}^{J}) + \tfrac{1}{2}\mathbf{R}^{J\dagger}(\boldsymbol{\Pi}'\cdot\mathbf{R}^{I}) \, .
\end{aligned} \tag{B.22}$$

Other matrices have the same definitions as those in SF-CIS, except for $\mathbf{F}_{\mathrm{xc}}^{[x]}$, which is defined as

$$\begin{aligned}
F_{\mathrm{xc},\mu\nu}^{[x]} &= \int^{[x]} \frac{\partial f_{\mathrm{xc}}}{\partial\rho}\frac{\partial\rho}{\partial P_{\mu\nu}}d\mathbf{r} + \int \frac{\partial f_{\mathrm{xc}}}{\partial\rho}\left(\frac{\partial\rho}{\partial P_{\mu\nu}}\right)^{[x]} d\mathbf{r} \\
&\quad + \int \frac{\partial^2 f_{\mathrm{xc}}}{\partial\rho\partial\rho'}\frac{\partial\rho}{\partial P_{\mu\nu}}\rho'^{[\overline{x}]}d\mathbf{r} \, .
\end{aligned} \tag{B.23}$$

Note that within this particular SF-TDDFT formalism, third functional derivatives of f_{xc} are not required in order to compute derivative couplings.

B.3 Comparison with Finite-Difference Derivative Couplings

Here, we compare our analytic derivative couplings with finite-difference results to validate the formalism. The finite difference formula for derivative coupling to the first order is

$$\left\langle \Psi_I \middle| \Psi_J^{[x]} \right\rangle = \frac{\langle \Psi_I | \Psi_J(x+\delta x) \rangle - \langle \Psi_I | \Psi_J(x-\delta x) \rangle}{2\delta x} \tag{B.24}$$

Our test system is H_2 with a bond length of $R = 1.1$Å. The cc-pVTZ basis set was used for all calculations, and CL-SF-TDDFT calculations use the BH&HLYP functional (50% Hartree-Fock exchange plus 50% Becke exchange[61] with Lee-Yang-Parr correlation[41]). We denote the latter method as SF-BH&HLYP.

The vertical excitation energies of the lowest six singlet states are shown in Table B.1. The S_4 state has HOMO $\rightarrow$ LUMO double excitation character, so it is missing in the restricted CIS (RCIS) calculation. Derivative couplings between the states S_1 and S_3 are listed in Table B.2.

From Table B.2, we can see that the finite difference results agree well with the analytic results for all of the three methods, which confirms the validity of our formalism as shown in Eq. (13). In addition, the derivative couplings calculated by Eq. (13) and Eq. (22) re exactly the same as the ones calculated using the formalism introduced in Ref. 21 for spin-conserved CIS, which comes as no surprise since the two formalisms are intrinsically equivalent for spin-conserved CIS.

Table B.1: Vertical excitation energies (in eV) for the lowest singlet states of H_2 using RCIS, SF-CIS, and SF-BH&HLYP in the cc-pVTZ basis set.

State	RCIS	SF-CIS	SF-BH&HLYP
S_1	10.6756	11.4664	9.7089
S_2	16.3160	14.8178	13.8764
S_3	20.7863	19.2544	18.4337
$S_4(\sigma^0\sigma^{*2})$		19.3603	17.7473
S_5	23.1458	21.1063	20.3281
S_6	23.1458	21.1063	20.3281

Table B.2: $\left\langle \Psi_1 \middle| \Psi_3^{[x]} \right\rangle$ derivative couplings (in a_0^{-1}) calculated by RCIS, SF-CIS and SF-BH&HLYP. The H_2 molecule is aligned to the z-axis and the derivative couplings vanish in the x and y directions.

	RCIS			SFCIS			SF-BH&HLYP		
Atom	Analytic	FD	ETF	Analytic	FD	ETF	Analytic	FD	ETF
H	−0.088057	−0.088057	−0.003857	−0.104717	−0.104718	−0.078036	−0.092725	−0.092725	−0.053895
H	0.088057	0.088057	0.003857	0.104717	0.104718	0.078036	0.092725	0.092725	0.053895

APPENDIX C

Supporting information for "Excited-State Deactivation Pathways in Uracil versus Hydrated Uracil"

C.1 Cartesian Coordinates of Critical structures

Table C.1: Cartesian coordinates of S_0-*min* of gas phase uracil

N	-0.778028	-0.148621	0.129781
N	0.622033	1.665951	-0.083327
C	-0.675020	1.202913	-0.083920
C	1.707862	0.859092	0.110932
C	1.581752	-0.459935	0.317470
C	0.255764	-1.062285	0.336501
O	0.012482	-2.229698	0.509763
O	-1.623675	1.926862	-0.258321
H	-1.711500	-0.519662	0.132806
H	0.723676	2.649633	-0.237770
H	2.662127	1.353679	0.086557
H	2.430646	-1.097078	0.469877

Table C.2: Cartesian coordinates of $S_{n\pi^*}$-min of gas phase uracil

N	-1.219504	-0.501062	0.011869
N	0.173607	1.322847	-0.205708
C	-1.102600	0.865406	-0.204267
C	1.312707	0.517496	-0.007876
C	1.153748	-0.821958	0.200934
C	-0.117471	-1.316286	0.206920
O	-0.493954	-2.634516	0.401334
O	-2.080102	1.556438	-0.373452
H	-2.152422	-0.864130	0.010264
H	0.265407	2.306317	-0.358007
H	2.259383	1.018800	-0.033768
H	1.998152	-1.466823	0.355037

Table C.3: Cartesian coordinates of *ci*-0π of gas phase uracil

N	-0.663423	-0.206624	-0.093886
N	0.718001	1.662145	0.265992
C	-0.590246	1.118033	0.254113
C	1.718696	0.879108	-0.178899
C	1.665583	-0.482150	0.264295
C	0.389710	-1.156228	-0.003881
O	0.124395	-2.325474	-0.013794
O	-1.541808	1.824395	0.442620
H	-1.595816	-0.578340	-0.144376
H	0.723978	2.666342	0.182039
H	2.423647	1.301089	-0.881149
H	1.835402	-0.561446	1.337276

Table C.4: Cartesian coordinates of *ci*-$n\pi$ of gas phase uracil

N	-0.757076	-0.078203	0.456403
N	0.674380	1.605618	-0.235641
C	-0.643880	1.144721	-0.148590
C	1.695657	0.954559	0.360117
C	1.567003	-0.518242	0.306608
C	0.296868	-1.028723	0.399242
O	-0.052432	-2.232827	0.351122
O	-1.566603	1.820020	-0.529023
H	-1.687989	-0.454052	0.474317
H	0.749434	2.559250	-0.552504
H	2.575959	1.499951	0.639885
H	2.356798	-1.131222	-0.091585

Table C.5: Cartesian coordinates of *ci*-$n\pi$-p of gas phase uracil

N	-0.001513	0.002892	0.000003
N	2.388296	-0.003709	-0.000001
C	1.196901	0.767216	0.000000
C	2.587089	-1.301969	0.000003
C	1.307594	-2.116947	-0.000001
C	0.080197	-1.464003	-0.000005
O	-0.959221	-2.053545	0.000002
O	1.355855	1.972779	0.000001
H	-0.892400	0.459804	-0.000001
H	3.231428	0.534090	0.000000
H	3.560114	-1.750986	-0.000001
H	1.318358	-3.190377	0.000001

Table C.6: Cartesian coordinates of S_0-*min* of (uracil)$(H_2O)_4$

C	-1.965155	-1.654351	0.153097
N	-2.024816	-0.306923	-0.024301
C	-0.911647	0.454364	-0.183918
N	0.272533	-0.233329	-0.157802
C	0.419869	-1.593177	0.030398
C	-0.812208	-2.326459	0.188154
O	-0.960195	1.666486	-0.339978
O	1.539666	-2.094649	0.052241
H	-0.774984	-3.388778	0.331557
O	-4.673001	0.741489	0.003406
O	4.020599	-0.912400	0.298770
O	2.764685	1.338557	-0.559457
O	1.154548	3.359239	0.608977
H	-2.926952	0.164729	-0.032031
H	1.113877	0.318931	-0.310756
H	-2.918822	-2.138541	0.266048
H	-4.888644	1.340633	0.718151
H	-4.974464	1.173866	-0.795641
H	0.363158	2.892524	0.320690
H	1.870944	2.788063	0.313643
H	3.370236	0.645128	-0.245132
H	3.026366	1.546633	-1.455733
H	3.180707	-1.397840	0.273455
H	4.359709	-0.992257	1.189042

Table C.7: Cartesian coordinates of $S_{n\pi^*}$-*min* of (uracil)$(H_2O)_4$

C	-1.983303	-1.757352	0.168810
N	-2.017339	-0.352672	0.017502
C	-0.943690	0.394980	-0.271847
N	0.256350	-0.276860	-0.361059
C	0.314457	-1.646990	-0.180221
C	-0.796739	-2.412757	0.031236
O	-0.991565	1.617303	-0.419628
O	1.601914	-2.116916	-0.509139
H	-0.732300	-3.482678	0.106425
O	-4.707885	0.763292	0.122188
O	4.159626	-0.897277	0.581390
O	2.800116	1.206098	-0.573536
O	1.133967	3.282153	0.427745
H	-2.911852	0.120429	0.025883
H	1.109379	0.263940	-0.468267
H	-2.911381	-2.216543	0.448844
H	-4.907492	1.387824	0.819099
H	-5.071022	1.143922	-0.677065
H	0.345645	2.797233	0.154932
H	1.855730	2.693654	0.186195
H	3.407525	0.574270	-0.157841
H	3.133778	1.369517	-1.455128
H	3.474850	-1.559786	0.471339
H	4.381238	-0.894782	1.512138

Table C.8: Cartesian coordinates of *ci*-0π of (uracil)$(H_2O)_4$

C	-1.933538	-1.611650	0.551930
N	-2.087411	-0.392464	-0.015264
C	-0.930448	0.352742	-0.222334
N	0.265660	-0.267662	0.047198
C	0.446216	-1.658476	0.093650
C	-0.828129	-2.364791	0.034438
O	-1.001365	1.524115	-0.544329
O	1.567537	-2.122661	0.041349
H	-0.979304	-2.649143	-1.006710
O	-4.636959	0.880979	0.166739
O	4.073834	-0.919378	0.391007
O	2.755077	1.324120	-0.414810
O	1.019098	3.426868	0.315586
H	-2.946732	0.151391	0.081143
H	1.094293	0.307502	-0.086845
H	-2.569591	-1.871135	1.384568
H	-4.864960	1.543881	0.818348
H	-5.036034	1.172509	-0.653005
H	0.265626	2.907104	0.023087
H	1.765588	2.831025	0.191618
H	3.358110	0.641171	-0.074707
H	2.958760	1.418920	-1.344852
H	3.254282	-1.430150	0.334350
H	4.425782	-1.061630	1.268542

Table C.9: Cartesian coordinates of *ci*-$n\pi$ of (uracil)$(H_2O)_4$

C	-1.960413	-1.575559	0.534946
N	-2.047167	-0.294577	0.083488
C	-0.946449	0.485781	-0.169121
N	0.257991	-0.134891	-0.094100
C	0.368568	-1.542043	-0.105439
C	-0.732637	-2.280977	0.210036
O	-1.062255	1.684808	-0.398950
O	1.510487	-1.996052	-0.491496
H	-0.715417	-3.350406	0.108490
O	-4.671573	0.844109	0.034411
O	4.015888	-0.977887	0.388605
O	2.792316	1.296351	-0.534394
O	1.123366	3.361789	0.554498
H	-2.944415	0.193208	0.092248
H	1.075285	0.407532	-0.351193
H	-2.790765	-1.986367	1.074348
H	-5.001468	1.434390	0.711595
H	-4.990010	1.195924	-0.796848
H	0.322802	2.909247	0.271786
H	1.830892	2.759015	0.304296
H	3.377331	0.603911	-0.185804
H	3.106589	1.505981	-1.413069
H	3.214157	-1.504151	0.289242
H	4.289926	-1.071174	1.300151

Table C.10: Cartesian coordinates of *ci*-$n\pi$-p of (uracil)$(H_2O)_4$

C	-2.107234	-1.573483	0.150471
N	-2.006473	-0.256821	-0.031414
C	-0.869413	0.505671	-0.192016
N	0.321430	-0.270155	-0.148901
C	0.338820	-1.721038	0.044945
C	-0.847932	-2.351763	0.190408
O	-0.876295	1.726643	-0.355542
O	1.502830	-2.234742	0.054254
H	-0.791305	-3.414103	0.330094
O	-4.684494	0.737784	-0.025043
O	4.031428	-0.904305	0.298390
O	2.760351	1.335163	-0.560372
O	1.152696	3.359136	0.608341
H	-2.910704	0.193420	-0.045515
H	1.176378	0.269570	-0.265148
H	-3.058755	-2.055756	0.263955
H	-4.890642	1.342404	0.717358
H	-4.976146	1.177163	-0.797159
H	0.362171	2.886950	0.320178
H	1.870396	2.789316	0.314437
H	3.371973	0.649260	-0.245552
H	3.025100	1.546324	-1.455185
H	3.212761	-1.405654	0.282747
H	4.361846	-0.990886	1.191385

APPENDIX D

Supporting information for "Spin-flip, Tensor Equation-of-Motion Configuration Interaction with a Density-Functional Correction"

D.1 Matrix elements in Eq. (5.12)

In this appendix, we briefly summarize the matrix elements of $\mathbf{M}$ in Eq. (5.12), which are derived from Eq. (5.5) with the spin-tensor basis shown in Eq. (5.18). More details can be found in Ref. 101.

The matrix $\mathbf{M}$ is the sum of three matrices,

$$\mathbf{M} = \mathbf{M}^{(0)} - \mathbf{M}^{(1)} + \mathbf{M}^{(2)}, \tag{D.1}$$

where

$$\mathbf{M}^{(0)} = \tfrac{1}{3}(\mathbf{M}_+ + \mathbf{M}_0 + \mathbf{M}_-) \tag{D.2}$$

$$\mathbf{M}^{(1)} = \left(\frac{S_0+1}{2S_0}\right)(\mathbf{M}_+ - \mathbf{M}_-) \tag{D.3}$$

$$\mathbf{M}^{(2)} = \left[\frac{(S_0+1)(2S_0+3)}{6S_0(2S_0-1)}\right](\mathbf{M}_+ - 2\mathbf{M}_0 + \mathbf{M}_-)\,. \tag{D.4}$$

The matrix elements of $\mathbf{M}_+$, $\mathbf{M}_0$, and $\mathbf{M}_-$ are grouped into different blocks. Recall that the blocks associated with de-excitation vanish, which makes the size of $\mathbf{M}$

about half the size of the orbital rotation Hessian in the conventional time-dependent Hartree-Fock method. Since $\mathbf{M}$ is not Hermitian, we need to calculate a few more matrix elements as compared to the approach used in Ref. 101. The results are summarized in Tables D.1 and D.2. In those tables, $\mathbf{F}$ is the Fock matrix, and $\mathbf{K}$ is the coupling matrix defined as

$$K_{pq,rs}^{\sigma\tau,\sigma'\tau'} = \langle p_\sigma s_{\tau'} || q_\tau r_{\sigma'} \rangle \ , \tag{D.5}$$

where σ, τ, σ', and τ' denote α or β spins. Finally, $\mathbf{K}^t$ is defined as

$$\mathbf{K}^t = \frac{1}{2}(\mathbf{K}^{\alpha\alpha,\alpha\alpha} + \mathbf{K}^{\beta\beta,\beta\beta} - \mathbf{K}^{\alpha\alpha,\beta\beta} - \mathbf{K}^{\beta\beta,\alpha\alpha}) \ . \tag{D.6}$$

Table D.1: Matrix elements of $\mathbf{M}_+$, $\mathbf{M}_0$, and $\mathbf{M}_-$ not including OO excitations.

Block	Matrix element
CV-CV	$[M_+]_{ai,bj} = \delta_{ij}F^{\alpha}_{ab} - \delta_{ab}F^{\beta}_{ij} + K^{\alpha\beta,\alpha\beta}_{ai,bj}$
	$[M_0]_{ai,bj} = \delta_{ij}(F^{\alpha}_{ab} + F^{\beta}_{ab})/2 - \delta_{ab}(F^{\alpha}_{ij} + F^{\beta}_{ij})/2 + K^{t}_{ai,bj}$
	$[M_-]_{ai,bj} = \delta_{ij}F^{\beta}_{ab} - \delta_{ab}F^{\alpha}_{ij} + K^{\beta\alpha,\beta\alpha}_{ai,bj}$
CV-CO	$[M_+]_{ai,vj} = \delta_{ij}F^{\alpha}_{av}$
	$[M_0]_{ai,vj} = (\delta_{ij}F^{\alpha}_{av} + \delta_{ij}F^{\beta}_{av} - K^{\alpha\alpha,\beta\beta}_{ai,vj} + K^{\beta\beta,\beta\beta}_{ai,vj})/2$
	$[M_-]_{ai,vj} = \delta_{ij}F^{\beta}_{av} + K^{\beta\alpha,\beta\alpha}_{ai,vj}$
CO-CV	$[M_+]_{ui,bj} = 0$
	$[M_0]_{ui,bj} = (\delta_{ij}F^{\beta}_{bu} - K^{\beta\beta,\alpha\alpha}_{ui,bj} + K^{\beta\beta,\beta\beta}_{ui,bj})/2$
	$[M_-]_{ui,bj} = \delta_{ij}F^{\beta}_{bu} + K^{\beta\alpha,\beta\alpha}_{ui,bj}$
CV-OV	$[M_+]_{ai,bv} = -\delta_{ab}F^{\beta}_{iv}$
	$[M_0]_{ai,bv} = (-\delta_{ab}F^{\alpha}_{iv} - \delta_{ab}F^{\beta}_{iv} + K^{\alpha\alpha,\alpha\alpha}_{ai,bv} - K^{\beta\beta,\alpha\alpha}_{ai,bv})/2$
	$[M_-]_{ai,bv} = -\delta_{ab}F^{\alpha}_{iv} + K^{\beta\alpha,\beta\alpha}_{ai,bv}$
OV-CV	$[M_+]_{au,bj} = 0$
	$[M_0]_{au,bj} = (-\delta_{ab}F^{\alpha}_{ju} + K^{\alpha\alpha,\alpha\alpha}_{au,bj} - K^{\alpha\alpha,\beta\beta}_{au,bj})/2$
	$[M_-]_{au,bj} = -\delta_{ab}F^{\alpha}_{ju} + K^{\beta\alpha,\beta\alpha}_{au,bj}$
CO-CO	$[M_+]_{ui,vj} = 0$
	$[M_0]_{ui,vj} = (\delta_{ij}F^{\beta}_{uv} - \delta_{uv}F^{\beta}_{ij} + K^{\beta\beta,\beta\beta}_{ui,vj})/2$
	$[M_-]_{ui,vj} = \delta_{ij}F^{\beta}_{uv} - \delta_{uv}F^{\alpha}_{ij} + K^{\beta\alpha,\beta\alpha}_{ui,vj}$
CO-OV	$[M_+]_{ui,bv} = 0$
	$[M_0]_{ui,bv} = -K^{\beta\beta,\alpha\alpha}_{ui,bv}/2$
	$[M_-]_{ui,bv} = K^{\beta\alpha,\beta\alpha}_{ui,bv}$
OV-CO	$[M_+]_{au,vj} = 0$
	$[M_0]_{au,vj} = -K^{\alpha\alpha,\beta\beta}_{au,vj}/2$
	$[M_-]_{au,vj} = K^{\beta\alpha,\beta\alpha}_{au,vj}$
OV-OV	$[M_+]_{au,bv} = 0$
	$[M_0]_{au,bv} = (\delta_{uv}F^{\alpha}_{ab} - \delta_{ab}F^{\alpha}_{uv} + K^{\alpha\alpha,\alpha\alpha}_{au,bv})/2$
	$[M_-]_{au,bv} = \delta_{uv}F^{\beta}_{ab} - \delta_{ab}F^{\alpha}_{uv} + K^{\beta\alpha,\beta\alpha}_{au,bv}$

Table D.2: Matrix elements of $\mathbf{M}_+$, $\mathbf{M}_0$, and $\mathbf{M}_-$ including OO excitations.

Block	Matrix element
CV-OO	$[M_+]_{ai,vw} = -K^{\alpha\beta,\alpha\beta}_{ai,vw}$
	$[M_0]_{ai,vw} = 0$
	$[M_-]_{ai,vw} = K^{\beta\alpha,\beta\alpha}_{ai,vw}$
OO-CV	$[M_+]_{tu,bj} = 0$
	$[M_0]_{tu,bj} = \delta_{tu}(F^{\alpha}_{bj} - F^{\beta}_{bj})/2$
	$[M_-]_{tu,bj} = K^{\beta\alpha,\beta\alpha}_{tu,bj}$
CO-OO	$[M_+]_{ui,vw} = 0$
	$[M_0]_{ui,vw} = -\delta_{uv}F^{\beta}_{iw}/2$
	$[M_-]_{ui,vw} = -\delta_{uv}F^{\alpha}_{iw} + K^{\beta\alpha,\beta\alpha}_{ui,vw}$
OO-CO	$[M_+]_{tu,vj} = 0$
	$[M_0]_{tu,vj} = -\delta_{tu}F^{\beta}_{jv}/2$
	$[M_-]_{tu,vj} = -\delta_{tv}F^{\alpha}_{ju} + K^{\beta\alpha,\beta\alpha}_{tu,vj}$
OV-OO	$[M_+]_{au,vw} = 0$
	$[M_0]_{au,vw} = \delta_{uw}F^{\alpha}_{av}/2$
	$[M_-]_{au,vw} = \delta_{uw}F^{\beta}_{av} + K^{\beta\alpha,\beta\alpha}_{au,vw}$
OO-OV	$[M_+]_{tu,bv} = 0$
	$[M_0]_{tu,bv} = \delta_{ut}F^{\alpha}_{bv}/2$
	$[M_-]_{tu,bv} = \delta_{uv}F^{\beta}_{bt} + K^{\beta\alpha,\beta\alpha}_{tu,bv}$
OO-OO	$[M_+]_{tu,vw} = 0$
	$[M_0]_{tu,vw} = 0$
	$[M_-]_{tu,vw} = \delta_{uw}F^{\beta}_{tv} - \delta_{tv}F^{\alpha}_{uw} + K^{\beta\alpha,\beta\alpha}_{tu,vw}$